Volume 1, Issue 1 2010

Radio Physics and Radio Astronomy

LEONID M. LYTVYNENKO
EDITOR-IN-CHIEF

begell house, inc.
publishers

Radio Physics and Radio Astronomy (ISSN: 2152-274X) is published four times a year and owned by Begell House, Inc., 50 Cross Highway, Redding, Connecticut 06896, Phone: 203-938-1300. Institutional subscription rate for 2010 is $681.00. Add $10.00 per issue for foreign airmail shipping and handling fees to all orders outside the United States and Canada. All subscriptions are payable in advance. Subscriptions are entered on an annual basis, i.e., January to December. Orders should be mailed to Begell House, Inc., 50 Cross Highway, Redding, Connecticut 06896. Payments should be made by dollar checks drawn on a U.S. bank.

Printed March 22, 2010

RADIO PHYSICS
AND
RADIO ASTRONOMY

ADDRESS: IRA NASU, 4, Chervonopraporna st.,
Kharkov, 61002, Ukraine
Phone: 380 (57) 700-3092
Fax: 380 (57) 706-1415
E-mail: journal@ri.kharkov.ua

AIMS and SCOPE

Radio Physics and Radio Astronomy was founded February 2, 1995 by the National Academy of Sciences of Ukraine (NASU), Institute of Radio Astronomy of NASU, and the Ukrainian Committee URSI

The journal *"Radio Physics and Radio Astronomy"* publishes articles on investigations in present-day radio physics and electronic engineering (*electromagnetic wave generation, electromagnetic wave propagation in natural and artificial media, radio-frequency antennas and receivers, signal processing, achievements of microwave technologies*), radio astronomy (*radio telescopes and radio-astronomy observation equipment; technique, results and analysis of radio-astronomy research efforts within the whole frequency range*), and astrophysics.

Radio Physics and Radio Astronomy

Volume 1, No. 1 **2010**

Content

Radio Physics and Radio Astronomy, 1(1), 3–9 (2010)

DISPERSION ANALYSIS OF INTERPLANETARY SCINTILLATIONS AT DECAMETER WAVELENGTHS: FIRST RESULTS

I. S. Falkovich[1], A. A. Konovalenko[1], N. N. Kalinichenko[1], M. R. Olyak[1], A. A. Gridin[1], N. N. Bubnov[1], A. I. Brazhenko[2], A. Lecacheux[3], & H. O. Rucker[4]

[1]*Institute of Radio Astronomy, National Academy of Sciences of Ukraine, 4, Chervonopraporna St., Kharkiv 61002, Ukraine*

[2]*Poltava Gravimetric Observatory, Subbotin Institute of Geophysics National Academy of Sciences of Ukraine, 27/29 Myasoedov St., Poltava 36029, Ukraine*

[3]*Ovservatoire Paris-Meudon, Paris, CNRS UMR 8644, France*

[4]*Institut für Weltraumforschung der Österreichischen Akademie der Wissenschaften, 6, Schmiedlstrasse, Graz, 8042, Austria*

*Address all correspondence to I. S. Falcovich E-mail:falk@ira.kharkov.ua

The potential of the dispersion analysis technique is discussed in application to interplanetary scintillations observed from two sites (UTR-2 and URAN-2 radio telescopes). By combining analyses of the frequency dependences shown by velocities of cross-spectral harmonics of the scintillations and of their power spectra, it proves possible to recover the basic parameters of the interplanetary plasma along the line of sight. In the framework of a layered model of the medium, layer thicknesses, densities and velocities can be estimated, as well as the power index of the spatial spectrum and inner scale of the turbulence.

KEY WORDS: *decameter wavelengths, radio telescope, scintillations, dispersion analysis, heliosphere*

1. INTRODUCTION

Studying the solar wind is among the principal tasks of the low frequency radio astronomy and Project LOFAR in particular [1]. Observations of scintillations of cosmic radio sources suggest a powerful tool for investigating the interplanetary medium [2]. The observations held in the meter band and at shorter wavelengths have provided many new data on the structure and dynamics of the interplanetary plasma in the inner heliosphere [3-5]. Decameter wavelength experiments were not as intense, while it is just the HF band which permits studying the outer heliosphere at great separations from the Sun [6, 7]. The outer heliosphere used to

ISSN 2152-274X

be investigated from space vehicles, however recently there have been only few long range space missions.

The difficulties encountered by decameter wave observers arise from the high level of electromagnetic interference, mainly from broadcasting radios, and ionospheric distortions of the received radio signal. The effect of these negative influences can be greatly reduced through the use of advanced broad-band radio receivers and digital spectrum analyzers (DSP). Recording the signal in a broad band (over 14 MHz) should allow suppressing the interference in the course of signal processing and separate the interplanetary scintillations from the ionospherically induced. Tell-tales of separation of the two kinds of scintillations are their different spectrum widths and different correlation lengths in the frequency domain [8]. The effective value of the frequency band used for the data processing shall be greater than 10 MHz, which enables a high sensitivity of the measurements and allows increasing the number of observable radio sources with different heliocentric coordinates.

Application of the scintillation technique first was based on the analysis of power spectra of the sources as observed with one radio telescope. Certain model representations of the medium structure allowed estimating parameters of both the "slow" and the "fast" solar wind. Further progress in the field was associated with the use of dispersion and tomographic analysis techniques, i.e. methods involving simultaneous observations at spatially separated sites. The tomographic analysis permits a fairly full reconstruction of the shape and dynamics of transient formations, before all of CMEs – coronal mass ejections [9]. The technique is least dependent on the model adopted for the medium, however it requires considerable numbers of the sounding radio sources. The latter requirement is hard to meet at decameter wavelengths because of the high level of the galactic background in the band, limiting the sensitivity of observations, and hence the number of accessible radio sources.

We will discuss below the potential of dispersion analysis [10] for decameter-wavelength interplanetary scintillations observed simultaneously from two sites. A combined analysis of their dispersive phase velocity and power spectra permits an improved determination of basic parameters of the interplanetary plasma along the line of sight. Making use of a layered medium model, one may be able to evaluate layer thicknesses and mass densities, as well as the drift velocity, power index of the spatial spectrum and inner scale of the turbulence.

2. SPECIAL FEATURES OF DISPERSION ANALYSIS AT DECAMETER WAVELENGTHS

Interplanetary scintillations are observable at decameter wavelengths for elongations greater than 80°, thus offering an opportunity to study the solar wind of the outer heliosphere at great separations from the Sun. In case the wind involves more than one plasma flow with different parameters, an analysis of power spectra alone of the scintillations may not always allow a correct choice of the the line of sight model of the medium. The model may be improved through application of the dispersion analysis of the phase velocity associated with the scintillations. The technique is based on studying the frequency dependence of velocities of cross-spectrum harmonics of the scintillations as recorded by two spaced antennas.

Let the "scintillation function" $\Delta I_{1,2}(t)$ be expanded in a Fourier integral,

$$\Delta I_{1,2}(t) = \int P_{1,2}(\Omega)\exp(-i\Omega t)\mathrm{d}\Omega,$$

$$P_{1,2}(\Omega) = \frac{1}{2\pi}\int \Delta I_{1,2}(t)\exp(i\Omega t)\mathrm{d}t =$$

$$= \left|P_{1,2}(\Omega)\right|\exp\left[i\varphi_{1,2}(\Omega)\right],$$

where $\Omega = 2\pi f$.

The cross-correlation function of the scintillations, $B(r,\tau)$, is

$$B(r,\tau) = \left\langle \Delta I_1(0,t)\Delta I_2(r,t+\tau)\right\rangle = \int W(\Omega)\exp(-i\omega\tau)\mathrm{d}\Omega,$$

while its cross-spectrum

$$W(\Omega) = \left|P_1(\Omega)\right|\left|P_2(\Omega)\right|\exp\left[i\left(\varphi_1(\Omega)-\varphi_2(\Omega)\right)\right]. \qquad (1)$$

It can be shown [10] that the velocity $V(\Omega)$ of cross-spectrum harmonics (Eq. (1)) may be expressed as

$$V(\Omega) = \frac{\Omega r}{\Delta\varphi(\Omega)}, \qquad (2)$$

where $\Delta\varphi(\Omega) = \varphi_1(\Omega) - \varphi_2(\Omega)$, and r is the separation between the two receive antennas (baseline length

of the interferometer). It follows from this equation that for obtaining the dispersion law $V(\Omega)$, knowledge of the frequency dependence of the phase shift between the observation sites would be necessary,

$$\Delta\varphi(\Omega) = \tan^{-1}\frac{\mathrm{Im}W(\Omega)}{\mathrm{Re}W(\Omega)}. \quad (3)$$

At the frequencies corresponding to the decameter waveband, the wave scattering plasma volume is rather extended (along the line of sight), with the denser part of it lying close to the observer. For this reason the most suitable mathematics is the Feynman trajectory integration technique which was used in paper [11] to derive the cross-spectrum of scintillations, *viz.*

$$W(r,f) \approx \pi^2 \frac{L\omega_p^4}{c^2\omega^2}\int_0^1 \frac{\mathrm{d}\zeta}{\zeta^{1/2}}\int_A^\infty \kappa_\perp \mathrm{d}\kappa_\perp \left[1-\cos\left(\kappa_\perp^2 L\zeta/k\right)\right]\times$$

$$\times\frac{\Phi_N(\kappa_\perp,0)}{\left[\kappa_\perp^2 V_\perp^2(\zeta)-4\pi^2 f^2\right]^{1/2}}\exp\left[-\frac{1}{2}\left(\kappa_\perp L\zeta\theta\right)^2 + i\frac{2\pi fr}{V_\perp(\zeta)}\right]. \quad (4)$$

Here $f=\frac{\Omega}{2\pi}$; $\kappa_\perp=\{\kappa_x,\kappa_y\}$ is the 2-D wave vector; $\zeta=(1-z/L)$; $V_\perp(\zeta)=\frac{V\sin\varepsilon}{R/R_0}$, with $R=\left[R_0^2+L^2\zeta^2-2R_0L\zeta\cos\varepsilon\right]^{1/2}$, $R_0=1$ a.u.; ε is the elongation; L the plasma layer thickness; θ the angular size of the source; ω_p the plasma frequency, and $A=2\pi f/V_\perp(\zeta)$. The spatial spectrum $\Phi_N(\kappa_\perp,0)$ of electron density irregularities has been assumed to follow the power law

$$\Phi_N(\kappa_\perp,0)\propto\sigma_N^2(\zeta)\exp(-\kappa_\perp^2 l_0^2)L_0^{3-n}\kappa_\perp^{-n},$$

where $\sigma_N^2(\zeta)$ is the dispersion of relative fluctuations in the electron density along the ray; l_0 and L_0 the inner and outer turbulence scales, respectively, and n the power-law index of the electron inhomogeneity spectrum.

At higher frequencies and/or small elongations the scattering volume can be regarded as a thin layer. Shown in Fig. 1 is the dispersion law calculated after Eqs. (2) to (4) for a 0.75 m wavelength and a spherically symmetric solar wind with a speed of 450 km/s. The source elongation was 20° and the angular size 0.1″. As can be seen from the Figure, the frequency dependence $V=V(f)$ is only slightly pronounced, owing to the small thickness of the interplanetary plasma layer to effectively scatter the radio frequency signal. Another reason is that the model adopted for the solar wind was a single velocity one.

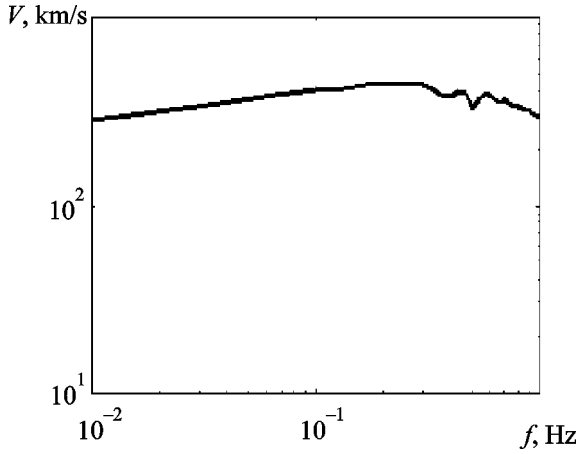

FIG. 1: The frequency dependence of the phase velocity of scintillations at the wavelength of 0.75 m (the elongation is $\varepsilon=20°$ and the source size $\theta=0.1''$)

At decameter wavelengths and elongations greater than 80° the effective thickness of the layer contributing to scintillations may be as high as 9 a.u. The slope of the dispersion dependence $V(f)$ is determined by the scatter of velocities, parameters of the turbulence and different widths of the solar wind flows. Fig. 2 presents dispersion dependences $V=V(f)$ calculated within the above described wind model for observation wavelengths of 3, 6 and 12 m (curves 1, 2 and 3, respectively), appropriate elongations (45°, 60°, and 90°), and source sizes of 0.2″, 0.5″, and 1.5″. The slope and span of the dispersion curves can be seen to increase as the wavelength moves toward decameter values. The reasons are the increased thickness of the scintillation contributing plasma layer and the variation of the wind speed projection $V_\perp(\zeta)$ along the line of sight. The higher the slope of the dispersion curve, the better is the accuracy of medium parameter recovery through matching the measured and the theoretical $V=V(f)$ dependences.

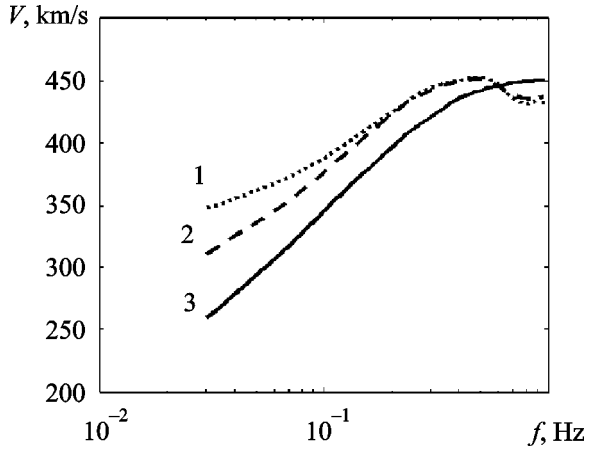

FIG. 2: Dispersion dependences shown by scintillations for a variety of elongations and wavelengths: curve 1 is for $\varepsilon = 45°$, $\lambda = 3$ m, and $\theta = 0.2''$; curve 2 for $\varepsilon = 60°$, $\lambda = 6$ m, and $\theta = 0.5''$; curve 3 for $\varepsilon = 90°$, $\lambda = 12$ m and $\theta = 1.5''$

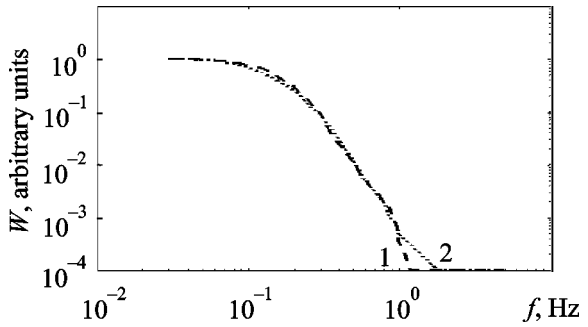

FIG. 3: Power spectra of scintillations computed for a spherically symmetric model of the solar wind (curve 1, with $\varepsilon = 90°$ and $V = 500$ km/s) and a dual-flow model (curve 2, velocities $V_1 = 350$ km/s and $V_2 = 500$ km/s)

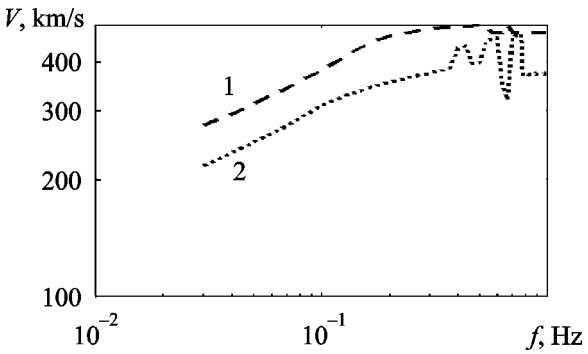

FIG. 4: Dispersion dependences of the phase velocity of scintillations computed for a spherically symmetric model of the solar wind (curve 1) and a dual-flow model (curve 2). Parameters of the medium have been the same as in Fig. 3.

The model of the solar wind may be essentially improved as a result of joint analysis of the scintillation spectrum and the dispersion dependence. Figs. 3 and 4 show these functions as calculated for a 12 m wavelength and a baseline of 153 km in length. Curves 1 correspond to a spherically symmetric solar wind, while curves 2 to a dual-flow model with different wind velocities within the flows. As can be seen, the two scintillation spectra are nearly coincident, whereas the dispersion curves show a marked difference.

The examples given provide evidence that the dispersion analysis technique may allow determining parameters of the medium in solar wind flows characterized by different velocities in the outer heliosphere.

3. OBSERVATIONS WITH THE URAN-2 INTERFEROMETER

The URAN-2 interferometer of the National Academy of Sciences of Ukraine (baseline length 153 km) involves array antennas of the radio telescopes UTR-2 (near Hrakovo township in the Kharkiv Region) and URAN-2 proper (village of Stepanivka in the Poltava Region), both operating in the frequency range 9 to 32 MHz [12, 13]. The effective collecting areas are 150,000 m^2 and 28,000 m^2, respectively, with beam widths 0.5° and 3.5° at 25 MHz. The signal detectors used for the observations were a triple-channel, broadband radiometer at the UTR-2 observatory (total band of analysis equal to 3 MHz [8]) and a 16-channel super-broad band correlation radiometer at the URAN-2 (total band width of 12 MHz, [14]). In spite of the smaller effective area of the URAN-2 array, the fluctuation sensitivity of the two radio telescopes proved commensurable, owing to the greater band width of the radiometer

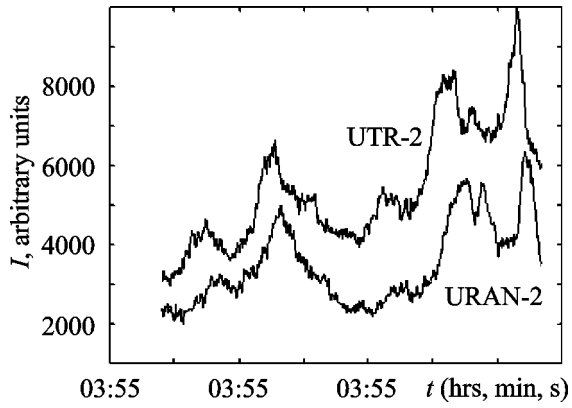

FIG. 5: An example of synchronized records of interplanetary scintillations

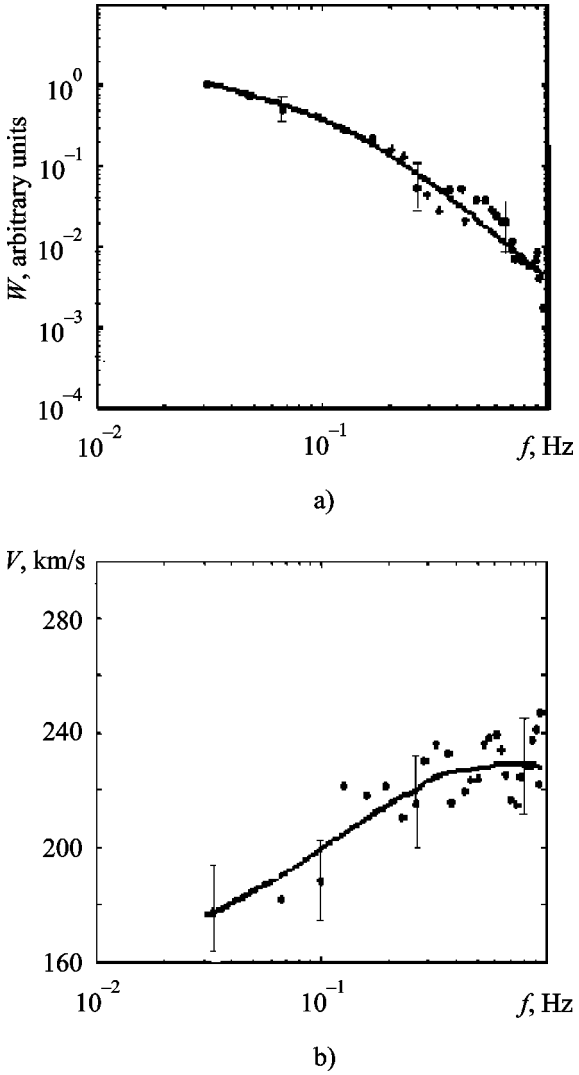

Fig. 6. Scintillation spectra (a) and dispersion dependences (b) for the radio source 3C144, as obtained in October, 2006 (the dots represent measured data, while the solid curves are computed results). The recovered solar wind parameters are $n = 3.0$ and $V = 230$ km/s (the model of a spherically symmetric wind)

at the site. Fig. 5 presents a sample of synchronized records of interplanetary scintillations from the source 3C196 (flux density about 300 f.u.). The time constant of recording was 0.1 sec.

Figs. 6 and 7 are examples of recovered solar wind parameters along the line of sight, relating to two days in the October of 2006. In the first case the source observed was 3C144 lying within the ecliptic plane. Ten days later it was the 3C196 whose heliospheric latitude is about 30°. In example one the structure of the medium along the line of sight (i.e. within the ecliptic plane) can be well represented by a spherically symmetric model of a slow solar wind. In the case of the "high latitude" source we have used a three-layer model involving high speed wind flows. This is in agreement with generally accepted concepts of velocity distributions in the solar equatorial region and at higher heliolatitudes, characteristic of the minimum activity periods [8]. Fig. 8 is a schematic of the solar wind structure along the line of sight toward 3C196.

CONCLUSIONS

As has been shown, application of the dispersion analysis technique permits recovering parameters of both fast and slow solar wind flows from the data of scintillation observations at decameter wavelengths. The theoretical estimates and the measurements performed demonstrate applicability of the method to two- and three-component velocity models of the line-of-sight outer heliosphere. The UTR-2 radio telescope of Ukraine currently remains an instrument with the largest effective collecting area (150,000 m^2), enabling one to consistently observe about a dozen of scintillating sources overnight. Unfortunately, it does not provide for a spatial resolution which would be sufficiently high for mapping. Implementation of the Giant,

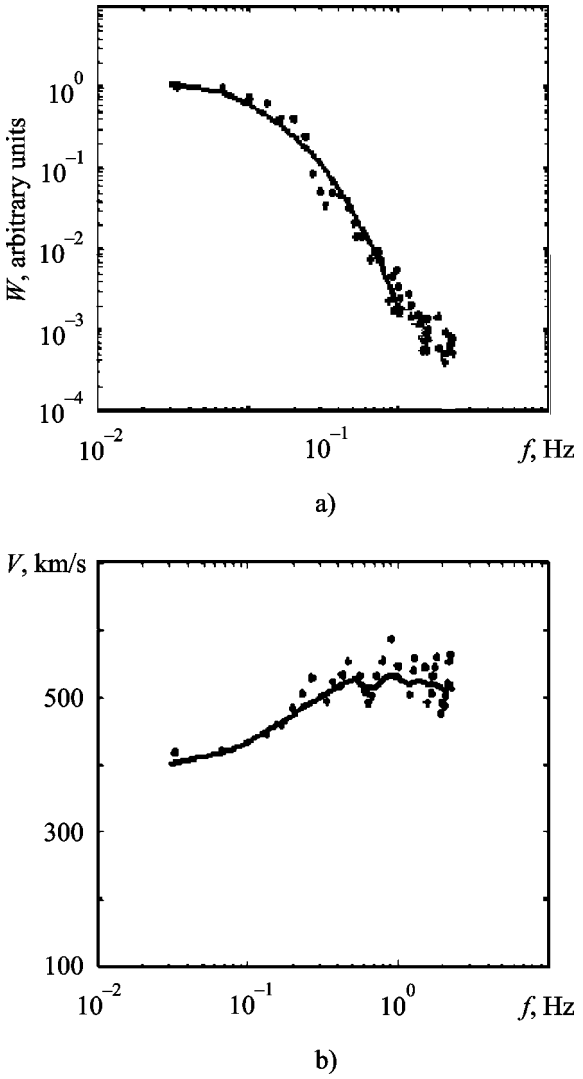

FIG. 7: Scintillation spectra (a) and dispersion dependences (b) for the radio source 3C196, as obtained in October, 2006 (the dots represent measured data, while the solid curves are computed results). The recovered solar wind parameters are: $n_1 = 3.8$; $V_1 = 550$ km/s; $l_0 = 300$ km, and $L_0 = 1$ a.u. (wind flow 1); $n_2 = 3.7$; $V_2 = 730$ km/s; $l_0 = 100$ km, and $L_0 = 2$ a.u. (wind flow 2), and $n_3 = 3.9$ and $V_3 = 500$ km/s (wind flow three)

New Generation Low Frequency Radio Telescope (effective area 1 M m^2), which Project is being pursued at the Institute of Radio Astronomy, National Academy of Sciences of Ukraine [15], should enable increasing the number of observable sources at least by one order of magnitude and greatly improving the resolution of maps of the outer heliosphere.

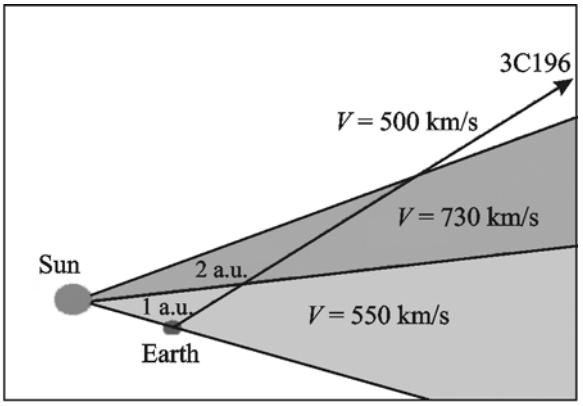

FIG. 8: The solar wind structure along the line of sight toward 3C196

ACKNOWLEDGMENTS

The work was done with a partial financial support from the Fundamental Research Program of the National Academy of Sciences of Ukraine ("Development of theories, methods and information technologies for integrated studies of solar – terrestrial ties as a basis for Space Weather forecasting"), and the INTAS Grant No 03-5727.

REFERENCES

1. Butcher, H. R., LOFAR: "First of a new generation of radio telescopes", *Proc. SPIE*, 5489:537-544, 2004.
2. Vitkevich, V. V. and Vlasov, V. I., Parameters of interplanetary electron density irregularities according to observational data of 1967-1969, *Astronomicheskii Zhurnal (Sov. Astron)*, 49(issue 3):595-606, 1972 (in Russian).
3. Vlasov, V. I., Interplanetary shock waves according to radio scintillation observations, *Geomagnetism i Aeronomia*, 21(5):927-929, 1981 (in Russian).
4. Vlasov, V. I., Shishov, V. I., and Shishova, T. D., Parameter variations of interplanetary scintillations and disturbance types in the interplanetary medium, *Geomagnetism i Aeronomia*, 23(6):888-893, 1983 (in Russian).
5. Blums, D. F. and Lotova, N. A., Analyzing frequency spectra of scintillations with account of velocity distributions in

the solar wind, *Geomagnetism i Aeronomia*, 21(2):209-213, 1981 (in Russian).

6. Bovkoon, V. P. and Zhouck, I. N., Interplanetary scintillations of decameter wave cosmic sources owing to interplanetary and ionospheric plasma irregularities, *Kosmicheskaia Nauka i Tekhnika*, (issue 7):80-91, 1992 (in Russian).
7. Falkovich, I. S., Konovalenko, A. A., Kalinichenko N. N., Olyak, M. R., Gridin, A. A., Bubnov, I. N., Lecacheux, A., Rucker, H. O., "Variation of parameters of solar wind stream structure outside 1 a.u. in 2003 and 2004," *Radiofizika i Radioastronomia*, 11(1):31-41,2006 (in Russian).
8. Falkovich, I. S., Kalinichenko, N. N., Gridin, A. A., and Bubnov, I. N., Feasibility of broad band observations of interplanetary scintillations at decameter wavelengths, *Radiofizika i Radioastronomia*, 9(2):121-129, 2004 (in Russian).
9. Jackson, B. V. and Hick, P. L., Heliospheric tomography using interplanetary scintillation observations 1. Combined Nagoya and Cambridge data, *J. Geophys. Res.*, 103(A6):12,049-12,067, 1998.
10. Lotova, N. A. and Chashey, I. V., Velocity distributions in the interplanetary medium as recovered from scintillation observations, *Geomagnetism i Aeronomia*, 18(5):809-817, 1978 (in Russian).
11. Olyak, M. R., Applying the dispersion analysis technique to solar wind investigations, *Radiofizika i Radioastronomia*, 10(4):385-391, 2005 (in Russian).
12. Braude, S. J. , Megn, A. V., and Sodin, L. G. The decameter-band radio telescope UTR-2. In: Pistolkors, A. A., editor. Antennas, issue 26. Moscow: Svyaz; 1978. p. 3-15 (in Russian).
13. Megn, A. V., Sharykin, N. K., Zakharenko, V. V., Bulatsen, V. G., Brazhenko, A. I., Vaschishin, R. V., Decameter wavelength radio telescope URAN-2, *Radiofizika i Radioastronomia*, 8(4):345-356, 2003 (in Russian).
14. Falkovich, I. S., Gridin, A. A., Kalinichenko, N. N., and Bubnov, I. N., A 16-channel correlation type radiometer for interplanetary scintillation observations, *Radiofizika i Radioastronomia*, 10(4):392-397, 2005 (in Russian).
15. Konovalenko, A. A., Falkovich, I. S., Kalinichenko, N. N., Gridin, A. A., Bubnov, I. N., Lecacheux, A., Rosolen, C., & Rucker, H. O.,Thirty-element active antenna array as a prototype of a huge low-frequency radio telescope, *Experimental Astronomy*, 16(3):149-164, 2003.

Radio Physics and Radio Astronomy, 1(1), 11–18 (2010)

PROPERTIES OF FAST DRIFTING TYPE III BURSTS AT DECAMETER WAVELENGTHS

V. N. Melnik[1], A. A. Konovalenko[1], H .O. Rucker[2], B. P. Rutkevych[1], E. P. Abranin[1], V. V. Dorovsky[1], A. I. Brazhenko[3], A. Lecacheux[4], & A. A. Stanislavsky[1]

[1]*Institute of Radio Astronomy, National Academy of Sciences of Ukraine, 4, Chervonopraporna St., Kharkiv 61002*

[2]*Institut für Weltraumforschung der Österreichischen Akademie der Wissenschaften, 6, Schmiedlstrasse, Graz, 8042, Austria*

[3] *Poltava Gravimetric Observatory, Subbotin Institute of Geophysics, National Academy of Sciences of Ukraine, 27/29 Myasoedov St., Poltava 36029, Ukraine*

[4]*Ovservatoire Paris-Meudon, Paris, CNRS UMR 8644, France*

*Address all correspondence to B. P. Rutkevich E-mail:bprutkevich@mail.ru

First results are reported concerning fast drifting type III-like radio bursts observed at 10 to 30 MHz. More than 1000 cases have been analyzed of the bursts recorded in 2002 to 2004. The frequency drift rates shown by the "fast" variety were several times higher than those of "standard" decameter wavelength type III bursts, while durations were mostly 1 to 2 s. The "fast" bursts were observable, for the most part, on those days when the active region stayed close to the central solar meridian. The explanation suggested for the high rate of the frequency drift of decameter wavelength type III-like bursts takes into account both the group velocity of electromagnetic waves and the speed of radiating electrons.

KEY WORDS: *burst, decameter wavelengths, frequency drift, polarization, polarimeter, spectrometer*

1. INTRODUCTION

Fast drifting type III bursts were first detected in 1959 by Young *et al*. [1] who observed the emissions at 500 to 950 MHz. They reported frequency drift rates greater than 2000 MHz/s, occasionally even tending to infinity. Along with negative drift rates (from higher to lower frequencies), bursts with a positive drift through the frequency domain were also observed. Characteristic durations of the bursts were 0.2 to 0.3 s and radiation flux densities $5 \cdot 10^4$ Jy to 10^8 Jy (1 Jy, or 1 f.u. $= 10^{-26}$ W/m$^2 \cdot$Hz). The writers also noted [1] that "faster" bursts were characterized by shorter durations.

Kundu *et al*. [2] established that fast drifting type III-like bursts normally occupy the range of 400 to 800 MHz, while being occasionally observed in a wider range, from 200 MHz up to 950 MHz. According to papers [1, 2], the bursts of this variety are often encountered as groups of 3 to 10 events. Some of them may change the sense of the drift rate after drifting initially from the lower to higher frequencies.

Elgaroy [3] has given a detailed analysis to 402 fast drifting type III bursts which he observed at 310

ISSN 2152-274X

to 340 MHz. Of the total number of 402 bursts, 50 % and 17 % were characterized, respectively, by negative and positive drift rates in the frequency domain. The remaining 33 % of the bursts showed "infinite" (i.e. greater than 500 MHz/s) rates of the frequency drift. The mean value of duration of the fast drifting type III bursts happened to be 0.26 s, or one fourth of the duration of "standard" type III bursts observable at these frequencies (i.e. 1.1 s). Elgaroy also noted that fast type III-like bursts occurred in groups and estimated the average separation between the bursts as 1.1 s. He studied the dependences of the burst duration and drift rate of the fast bursts upon the position on the solar disk of their associated active region. As it occurred, the duration increases as the active region moves away from the central meridian. At the same time, the number of bursts with an "infinite" positive drift rate in frequency decreases. These findings have led Elgaroy to the conclusion that an essential factor to influence the formation of fast type III radio bursts is the impact of propagational effects of the radiation traveling through the solar corona.

Gopal Rao [4] studied the polarization of type III bursts of various durations at somewhat lower frequencies. He found out that the bursts of the shortest duration (1 or 2 s) were characterized by a high degree of polarization (up to 70 %). While drift rates were not determined in paper [4], Zaitsev and Levin [5] classified the bursts reported there as type III events, judging by their short duration.

In 1984 Zaitsev and Levin [5] made an attempt of detecting fast type III bursts at decameter wavelengths (frequencies of 16 and 25 MHz) when analyzing the storm event of 6-7 June, 1977. They concluded that the durations and drift rates of such bursts (if they existed at all) should not be very different from the figures typical of standard type III bursts.

As for possible interpretations of the high drift rates of type III-like bursts, they are, in fact, just two. One of the models [1, 3] is based on the theory of common type III bursts and ascribes the high rate of drift of the "fast" bursts to structural irregularities in the lower corona, possessing large gradients of mass density. The appearance of bursts with a positive drift owes to the sunward motion of electron beams "responsible" for the bursts. Ledenev [6] suggested recently that a positive drift in frequency could be explained by reduced group delays of the signal when the source of radiation moves toward lower plasma densities. Also, he noted that the group delay of signals arriving from different levels in the corona can be correctly estimated only through account of the fairly high speeds of the electrons responsible for type III bursts.

Zaitsev and Levin [5] suggested a different model where all type III bursts (both fast drifting and standard) are associated with the same electron beam, however one characterized by a spectrum of electron velocities. The standard bursts are generated by the bulk of the beam electrons, while the fast bursts get excited by the fastest particles from the leading edge of the beam. The fast electrons move at roughly twice the speed of the bulk of particles, hence it can be expected that the drift rates characteristic of the fast and standard bursts would be also different by a factor about two. The writers [5] associated the effect of fast drifting type III bursts with excitation of cyclotron waves. Whereas excitation rates of such waves are dictated by the magnetic field strength, favorable conditions for the generation of fast type III bursts shall be expected (after Zaitsev and Levin) in the lower corona. In other words, this variety of bursts should be preferably observable at higher frequencies, which assertion was fully confirmed by the observational results of the time.

This paper presents results of first observations of the fast drifting type III bursts at decameter wavelength (i.e. frequencies of 10 to 30 MHz). They demonstrate characteristics similar to the properties of higher frequency type III bursts. We have also noted that the appearance frequency of such bursts is strongly dependent on the location of the active region on the solar disk. In our opinion, this speaks in favor of the decisive role played in the formation of such bursts by propagation effects. Finally, the paper suggests a possible explanation to the phenomenon of fast drifting type III bursts, based on the account of speeds of the radiation sources and group velocities of the waves they emit, as these contribute jointly to drift rate values of the bursts.

2. OBSERVATIONS

The fast type III bursts that are discussed in the paper were observed with the UTR-2 radio telescope in 2002–2004. The observations were performed with three sectors of the array antenna (total area of 30,000 m^2), which

produced a 1°×13° reception pattern of the telescope. In 2002 the signals were recorded with a digital spectral polarimeter (DSP) [7] which provided for a high resolution, both in the frequency and time domain (12 KHz and 20 to 100 ms, respectively), within the 18 to 30 MHz band. Besides, the observations of 2002 to 2004 were done with a 60-channel spectrometer providing nearly a 10 ms time domain resolution and a 300 KHz frequency resolution through the frequency band of 10 to 30 MHz.

The drift rates of standard type III bursts observed at decameter wavelengths (frequencies 10 to 30 MHz) normally are 2 to 4 MHz/s, with 4 to 10 s burst durations [8,9]. Yet during type III storms the present authors were sometimes able to record "faster" bursts whose drift rates were greatly in excess of these values. The burst durations often were shorter than for standard type III bursts. The present paper is dedicated to the said fast-drifting bursts of type III (or, according to the nomenclature accepted in the English-language literature, type III-like bursts [3]). They will be analyzed, based on the selection of 1100 plus bursts recorded during five storms of 2002 to 2004 (see the Table). The total observation time was 120 hr. All the fast drifting type III bursts were characterized by a negative frequency drift (an example is given in Fig. 1, a). Unlike the "standard" type III bursts (whose time "profile" is characterized by rapid growth and a relatively slow decay), all the fast bursts demonstrated a practically symmetric profile (see Fig. 1, b)

At decameter wavelengths we were able to also observe fast drifting type III bursts characterized by a fine structure in the frequency domain (see Fig. 2, a). They will be named fast type IIIb-like bursts, since their frequency structure is similar to such of (standard) type IIIb bursts. Higher frequency observations of such bursts (i.e. at meter or decimeter wavelengths) have not been reported until now.

When performing statistical analysis, we referred to some events as type III-like fast bursts if they showed frequency drift rates higher than 4 MHz/s and were recordable nearly through the observational range. It could be said for virtually all the fast-drifting bursts observed that their drift rates remained constant along the *t-f* trace. The highest drift rate recorded to date belongs to the burst event observed 18 August, 2002 (see Fig. 2, b). The value was close to 40 MHz/s. "Infinite" drift rates (i.e. greater than 100 MHz/s) were not reported, nor were bursts with a reverse sense of the drift through a frequency band comparable with the total range of observation (10 to 30 MHz). Meanwhile, in a few cases bursts with a positive drift sense (from lower to higher frequencies) were recorded within the range of 4 to 5 MHz. These were not regarded as fast type III-like bursts. Drift rate histograms are very much alike for the bursts of all burst storms (a histogram for

TABLE: The appearance frequencies of fast-drifting type III-like bursts as observed during five burst storms of 2002 to 2004. The bold-face entries refer to the dates when the active region crossed the central meridian on the solar disk

Year	Date, month	Number of bursts per minute	Duration of observations, hr/min	Number of bursts
2002	13.07	0.02	5 hr 36 min	7
	14.07	0.03	4 hr 57 min	8
	15.07	0.04	4 hr 48 min	10
	16.07	**0.06**	**3 hr 47 min**	**13**
	17.07	0.00	3 hr 40 min	1
2002	26.07	0.07	5 hr 28 min	24
	27.07	0.09	6 hr 17 min	33
	28.07	**0.46**	**6 hr 14 min**	**171**
	29.07	0.02	5 hr 37 min	6
	30.07	0.06	2 hr 52 min	10
2002	16.08	0.04	7 hr 00 min	16
	17.08	**0.12**	**3 hr 26 min**	**24**
	18.08	0.06	7 hr 30 min	28
	19.08	**0.08**	**1 hr 18 min**	**6**
2003	01.07	0.00	7 hr 30 min	2
	03.07	0.09	2 hr 56 min	16
	04.07	**0.40**	**6 hr 20 min**	**153**
	05.07	0.28	4 hr 39 min	77
	06.07	0.03	6 hr 31 min	11
2004	17.06	0.07	5 hr 04 min	20
	18.06	0.20	6 hr 05 min	71
	19.06	**0.45**	**5 hr 44 min**	**156**
	20.06	0.33	6 hr 03 min	121
	21.06	**0.40**	**5 hr 20 min**	**131**
	22.06	0.19	5 hr 32 min	62

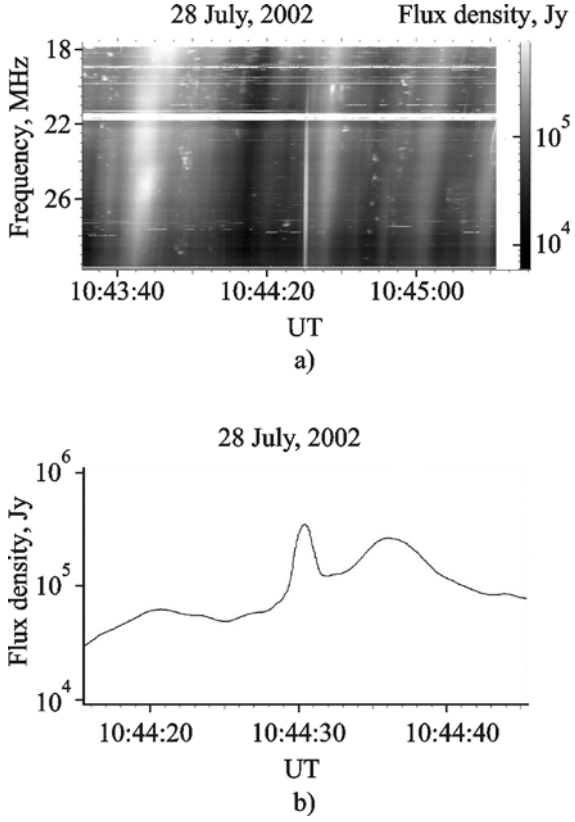

FIG. 1: (a) A fast-drifting type III-like burst (at 10:44:30 UT) observed against the background of standard type III events; and (b) the temporal "profile" of that burst

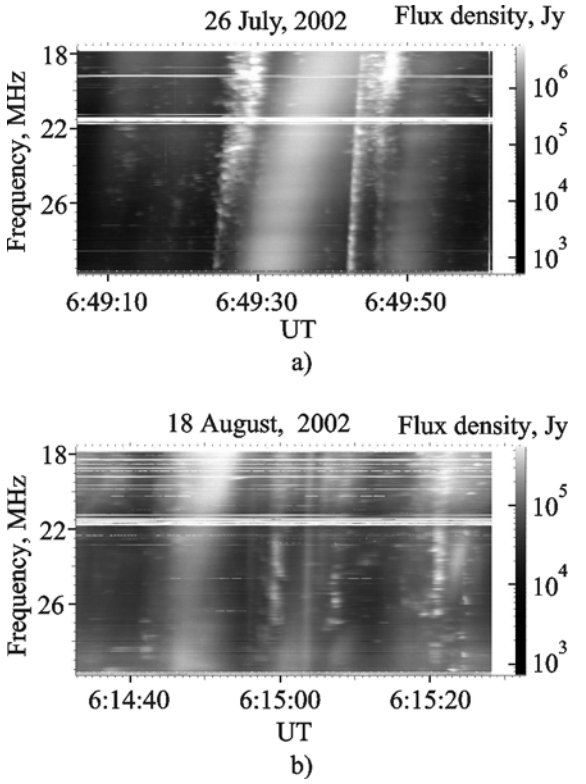

FIG. 2: (a) A fast-drifting type IIIb-like burst (at 06:49:42 UT) observed against the background of "standard" type III and type IIIb events; and (b) a type III-like burst (at 06:15:04 UT) with the highest drift rate observed (40 MHz/s)

the storm of 26 to 30 July, 2002 is shown in Fig. 3, a). As can be seen from the histograms, drift rates of the fast bursts can be as high as 20 MHz/s, which is 5 to 10 times greater than the rates typical of "standard" type III events.

It follows from Fig. 3, b that the major part of the fast drifting bursts observed in the series were of durations between 1 and 2 seconds, or 4 to 5 times shorter than the standard type III bursts at decameter wavelengths. A similar value for the duration ratio of higher frequency type III and fast type III bursts was noted earlier in paper [3]. As for the flux densities of the bursts under study, they are generally lower than the values reported for high frequency analogs (see Fig. 3, c). Also, it will be noted that flux density distributions are rather different for different burst storms, unlike the drift rate or duration distributions. To our belief, this might be related to the size of the active solar regions associated with the decameter wavelength emissions. Whereas the drift rate and duration of the bursts appear to be determined by parameters of the corona which are not as strongly influenced by the active regions, since the generation areas are greatly separated from the photosphere.

We have analyzed the appearance frequency of type III-like bursts in dependence on the location of the relevant active area on the solar disk. The observations belonged to various time intervals, therefore a unified parameter for the analysis was the appearance frequency of fast drifting bursts on a given day. This was defined as a ratio of the number of fast bursts recorded to the total observational time for the day.

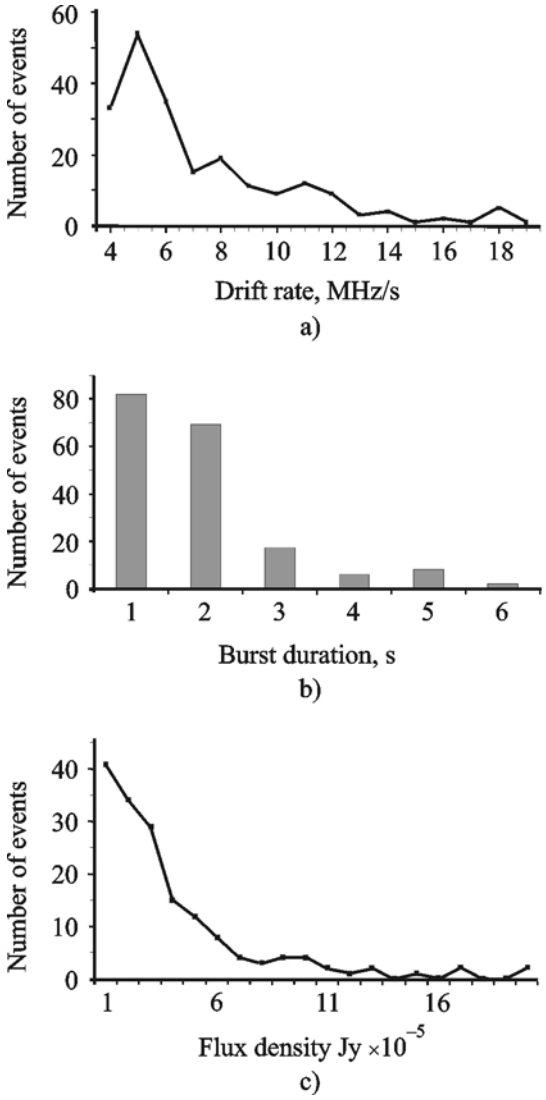

FIG. 3: Drift rate (a), duration (b) and flux density (c) histograms of the fast-drifting type III-like bursts belonging to the storm of 26-30 July

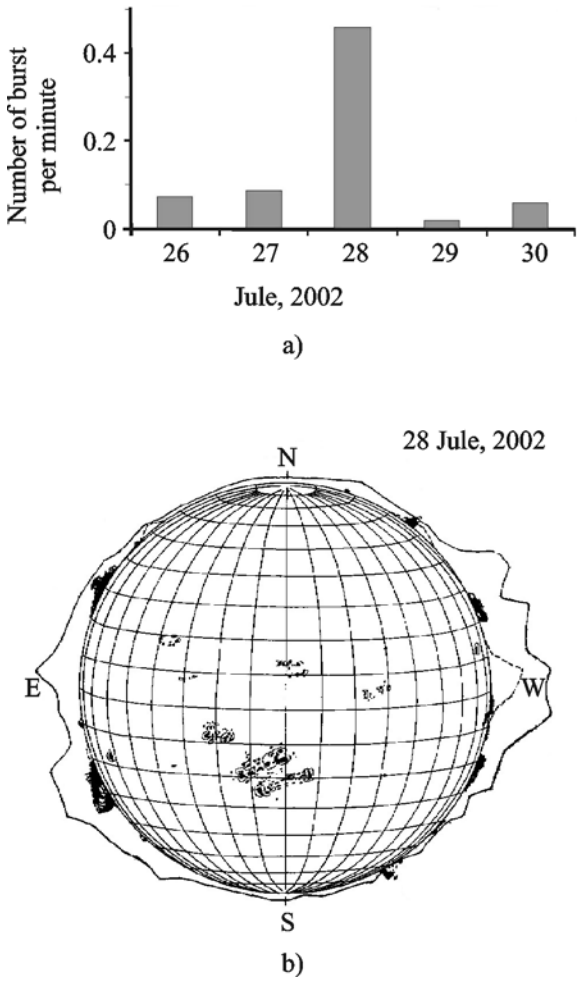

FIG. 4: (a) Appearance frequencies of fast type III-like bursts for various days of the storm of 26-30 July, 2002, and (b): position of the active region on the solar disk on 28 July, 2002

As it occurred, the fraction of fast type III-like bursts observed over the storm duration showed a marked correlation with the position of the active region on the solar disk. In the case of the July, 2002 storm (26 to 30 July), the appearance frequency reached its maximum on July 28, when the active region stayed close to the central meridian (see Fig. 4). The appearance frequency of bursts on that day was almost ten times higher than on adjacent dates. The situation was similar with other burst storms (e.g., 13 to 17 July, 2002 and 1 to 3 July, 2003) when just one active region was close to the central meridian. In the case of two active regions following one another (like, for example, during the storms of 16-19 August, 2002 or 17-22 June, 2004) the distribution function of the burst appearance frequency showed two maxima corresponding to their dates of crossing the central meridian (see the Table). This property of fast type III-like bursts is similar to the behavior demonstrated by the high frequency type III bursts described in paper [3], however it is better pronounced at decameter wavelengths. Thus, our obser-

vational data seem to confirm the relation noted in [3] between burst characteristics and propagation effects of the radio emissions in the solar corona. In our view, the propagation effects just might be responsible for the appearance of fast drifting type III bursts. Proceeding from the dependence of their appearance frequency on the date of observation (Fig. 4, a) one can obtain an "upper estimate" for the width of the bursts' radiation pattern, namely about 10 degrees. Our attempts of revealing smallest-scale temporal structures (shorter than of day's duration, on the date of maximum appearance frequency of the fast-drifting bursts) have not been successful.

3. DISCUSSION

Prior to our observations, it was generally accepted that fast type III-like bursts were a phenomenon characteristic mainly of frequencies above 200 MHz. The many records obtained at decameter wavelengths suggest a somewhat new look at the events and the underlying physics. As a matter of fact, most of the models suggested earlier for interpreting high frequency type III bursts of the fast variety face difficulties when applied to lower frequency events. In the case of a model which ascribes the bursts to high gradients of density in the corona [1, 3] the existence of suitable coronal inhomogeneities seems doubtful. Indeed, formations with a mass density tens of times lower than in the ambient coronal plasma can hardly be expected at altitudes comparable to one solar radius. The required size of such areas should also be comparable to the solar radius, since the bursts under discussion demonstrate a stable high drift rate over the range from 30 to about 10 MHz. Moreover, fast drifting type III-like bursts are observed simultaneously with standard type III events (see Figs. 1 and 2), which latter are generated by electrons moving through the middle corona. Finally, the essential regularity which we have established, namely that the burst appearance frequency is dependent upon position on the solar disk, can in no way support any model hinging on the assumption of deep inhomogeneities in the corona.

As can be seen in Fig. 3, a, the histogram of frequency drift rates of fast bursts decreases monotonically in the range of 6 to 10 MHz/s where the Zaitsev–Levin model [5] predicts an enhanced number of fast drifting bursts. Besides, it follows from our observations that the drift rate of fast type III-like bursts may exceed the standard rates typical of ordinary type III events by a greater factor than 10. Substituting these figures into the model [5] one would estimate the velocity of the electron beam generating the type III radio bursts as a value exceeding the speed of light. Indeed, the common equation for the frequency drift rate, $\mathrm{d}f/\mathrm{d}t$, is

$$\frac{\mathrm{d}f}{\mathrm{d}t} \approx \frac{\mathrm{d}f}{\mathrm{d}n}\frac{\mathrm{d}n}{\mathrm{d}r}v_s, \qquad (1)$$

where v_s is the velocity of the burst generating electrons; n the number density of the plasma at the generation point of the electromagnetic wave; $\mathrm{d}f/\mathrm{d}n = f_{pe}/2n -$ if the emission occurs at the fundamental harmonic, hence at the plasma frequency, $f = f_{pe}$, ($f_{pe} = \sqrt{4\pi e^2 n/m}$, and e and m are, respectively, the electron charge and mass). In the case of standard type III bursts a 2 to 4 MHz/s drift rate corresponds, according to Eq. (1), to an electron beam velocity $\approx 0.3c$, where c is the speed of light. Accordingly, the electron velocity corresponding to drift rates of 20 to 30 MHz/s should be much higher than the speed of light. For all the reasons listed in this Section we are in need of looking for new hypotheses to explain the phenomenon of fast type III-like bursts.

The derivation procedure of Eq. (1) suggests that the motion velocity of the radiating source is lower than the velocity of the electromagnetic wave emitted. This is true far away from the point of beam injection, however may not be so near that point. Now we intend deriving an equation for the drift rate of a burst with account of the group velocity v_{gr} of the electromagnetic waves emitted, as well as of the velocity v_s of the radiating source moving at angle α relative the Sun – Earth line (see Fig. 5). The difference of times for frequencies f_1 and f_2 to arrive to the observer is

$$\Delta t = t_2 - t_1 = \frac{r_{12}}{v_s} + \int_{R_1}^{R_2}\frac{\mathrm{d}r}{v_{gr}} \approx \frac{r_{12}}{v_s v_{gr}}(v_{gr} - v_s\cos\alpha), \qquad (2)$$

where r_{12} is the separation between generation levels for the two frequencies; R_1 and R_2 are the distances from the generation points to the observer, and t_1 and

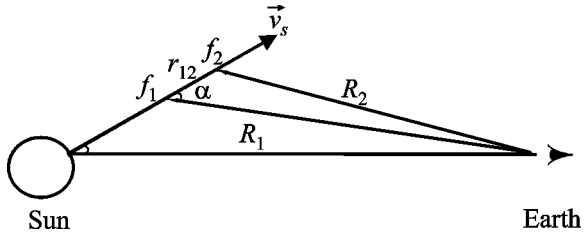

FIG. 5: The theoretical model: Schematic of motion of the electron beam

t_2 the moments of arrival of the two waves. (When deriving Eq. (2), it has been taken into account that $r_{12} \ll R_1, R_2$.) If the frequencies f_1 and f_2 are close enough, the drift rate can be written as

$$\frac{\mathrm{d}f}{\mathrm{d}t} \approx \frac{f_2 - f_1}{t_2 - t_1} \approx \frac{\mathrm{d}f}{\mathrm{d}n}\frac{\mathrm{d}n}{\mathrm{d}r}\frac{v_s v_{gr}}{v_{gr} - v_s \cos\alpha}. \qquad (3)$$

As can be seen, the drift rate can assume high values and even change its sign, provided that the group velocity is close to the speed of the electrons. Hence, there is no need in assuming a sunward direction of the source motion to explain positive values of the drift rate (it should be noted that Ledenev [6] arrived to the same conclusion). Evidently, the effect is particularly bright with small values of the angle α, i.e. when the beam electrons move practically toward the observer. For the fast drifting bursts to appear at greater values of α, ever higher electron speeds are required. With $v_{gr} \approx c$ and $v_s \ll c$ Eq. (3) goes over to Eq. (1). Eq. (3) has been derived on the assumption that the emitted wave is characterized by strictly fixed magnitudes of the frequency and wavenumber, and the radiating source is a point-size object. In actual fact, the waves generated by the electron beam occupy a frequency band of certain width, and the radiating area is rather large in size (the effective cross section for the decameter waveband is comparable with the solar disk). A consistent account of these features would be possible only if the problem were analyzed numerically, which is beyond the scope of this paper. Here we intended just to call one's attention to the feasibility of interpreting fast type III-like bursts without assumptions on large scale coronal inhomogeneities with high gradients of mass density.

4. CONCLUSIONS

The fast type III-like bursts that we have observed at frequencies of 10 to 30 MHz are characterized by frequency drift rates as high as 40 MHz/s. This is greater than the drift rate of "standard" type III bursts by more than a factor of 10. The durations of the fast type III-like bursts are, for the most part, 1 or 2 seconds, which is 4 to 5 times shorter than the duration of ordinary bursts. This feature was also noted by Elgaroy [3] with respect to higher frequency (meter- and decimeter-wavelength) fast drifting type III bursts. The fast decameter wavelength bursts are not as intense as the ordinary type III bursts. Analysis of the appearance frequency of fast type III-like bursts in dependence on the location of active areas on the solar disk has revealed that the greater number of such bursts are observed on the dates when an active area crosses the central solar meridian. A similar regularity, while somewhat less pronounced, was reported in paper [3] with regard to high frequency type III-like bursts. In our view, this property can be exclusively associated with wave propagation effects on the way to the observer. When estimating the drift rate of a burst, it is important to make account not of the group velocity alone of the electromagnetic wave radiated (like it is commonly done) but of the velocity of the generating electrons as well. If these values happen to be roughly equal in magnitude, the drift rate may increase in the positive direction or change sign. Thus, there is no need any more to assume a sunward-directed motion of the source for interpreting positive values of the drift rate.

ACKNOWLEDGMENTS

The work was supported by the INTAS Project 03-5727 and partly by the Program of Collaboration between the Austrian Academy of Sciences and the National Academy of Sciences of Ukraine.

REFERENCES

1. Young, C. W., Spencer, C. L., Moreton, G. E., and Roberts, J. A., A preliminary study of the dynamic spectra of solar radio burst in the frequency range 500–900 Mc/s, *Astrophys. J.*, 133:243-254, 1961.
2. Kundu, M. R., Roberts, J. A., Spencer, C. L., and Kuiper, J. W., A comparison of the dynamic spectra of solar radio bursts in the decimeter- and meter- wavelength ranges, *Astrophys. J.*, 133:255-259, 1961.
3. Elgaroy, O., Type III-like Solar Radio Bursts, *Astron. Astrophys.*, 82:308-313, 1980.
4. Gopal Rao, U. V., The polarization structure of type III solar radio bursts, *Aust. J. Phys*., 18:283-286, 1965.
5. Zaitsev, V. V. and Levin, B. N., A possible generation mechanism of type III-like solar radio bursts, *Astron. Astrophys*., 134:268-272, 1984.
6. Ledenev, V. G., On the group delay and the sign of frequency drift of solar type III radio bursts, *Solar Phys.,* 197:387-397, 2000.
7. Kleewein, P., Rosolen, C., and Lecacheux, A., New Digital Spectrometers for Ground Based Decameter Radio Astronomy. In: Rucker, H. O., Bauer, S. J., and Lecacheux, A., editors. Planetary Radio Emission IV. Vienna: Austrian Academy of Sciences Press, 1997, p. 349-358.
8. Abranin, E. P., Bazelian, L. L., Rapoport, V. O., and Tsybko, Y. G., Variations of type III burst parameters during a decametric solar storm, *Solar Phys*, 66:333-346, 1980.
9. Abranin, E. P., Bazelian, L. L., and Tsybko, Y. G., The stability of decametric type III burst parameters over the 11-year solar activity cycle. The frequency drift rate of radio bursts, *Astron. Zh*., 67:141-150, 1990 (in Russian).

Radio Physics and Radio Astronomy, 1(1), 19–26 (2009)

THE MECHANISM OF COMPONENT FORMATION OUT OF THE MAIN PULSE OF A RADIO PULSAR. I. THE PRECURSOR

S. A. Petrova

Institute of Radio Astronomy, National Academy of Sciences of Ukraine, 4, Chervonopraporna St., Kharkiv 61002, Ukraine

*Address all correspondence to S. A. Petrova E-mail:petrova@ri.kharkov.ua

Induced scattering of radio emission off the ultrarelativistic particles in a superstrong magnetic field is considered. The problem of radio beam scattering into the background radiation is solved. In the magnetosphere of a pulsar, this process can be efficient, and the scattered radiation concentrates close to the external magnetic field direction. Because of rotational aberration, the scattered component precedes the main pulse in the pulse profile and can be identified with the precursor component of a pulsar. In the framework of our model, the observed polarization, spectral and fluctuation properties of the precursor emission as well as its connection to the main pulse are explained.

KEY WORDS: *pulsar, pulse, polarization, radio emission, magnetosphere, scattering, intensity transfer, numerical estimate*

1. INTRODUCTION

The radio profiles of some pulsars contain a precursor being a peculiar component preceding the main pulse by ten-twenty degrees [1-4]. The main distinctive feature of precursors is almost complete linear polarization of their radiation (as a rule, the main pulse is markedly depolarized because of simultaneous presence of the two orthogonally polarized modes of emission). The spectra of the precursor and the main pulse differ as well [3-5]. However the individual pulse observations strongly testify to the physical connection between the two components. The observational manifestations of this connection are very diversiform. In the pulsar B1822-09, the precursor is present only in strong pulses [3, 6, 7]. In the pulsar J1326-6700, on the contrary, the precursor is visible only in the cases when the main pulse intensity is below the detection level [8]. In the Vela pulsar, the stronger the precursor, the larger is its separation from the main pulse [4].

The unusual polarization, spectral and fluctuation properties of a precursor call for theoretical explanation, however the nature of this component has not been discussed in the available literature. Recently, the geometrical model of the profile of the pulsar B1822-09 has been suggested [9] which implies that the emission of the precursor and the main pulse is generated at different altitudes in the pulsar magnetosphere. The precursor location in the pulse profile can really be explained by the component formation in the outer magnetosphere, at the altitudes much higher than the emission altitude of the main pulse. However, with the assumption of an independent generation of the two components, it is difficult to interpret the observed correlation of their intensities.

In this paper, the physical mechanism of the precursor formation is suggested, which allows to explain the

ISSN 2152-274X

peculiarities of this component and also its connection to the main pulse. The precursor is considered as a consequence of the induced scattering of the main pulse emission off the particles of the electron-positron plasma in the magnetosphere of a pulsar. Below, the induced scattering of the directed emission of a pulsar into the background in the approximation of a superstrong magnetic field is investigated in detail and solved. It is shown that at pulsar conditions this process can be so efficient that the scattered component may become comparable with the main pulse.

2. PROBLEM STATEMENT

The pulsar magnetosphere is filled with an ultrarelativistic electron-positron plasma which streams along the open magnetic field lines and leaves the magnetosphere as the pulsar wind. The pulsar radio emission originates deep in the tube of the open magnetic lines and, consequently, on its way in the magnetosphere it propagates through the plasma flow. As the brightness temperatures of the pulsar radio emission are extremely high, $T_B = 10^{25} \div 10^{30}$ one can expect the induced scattering of the emission off the pulsar plasma particles being significant.

The external magnetic field may affect the scattering process, changing the scattering cross-section and the recoil. The general form of the scattering cross-section in the magnetic field is found in [10, 11]. In [11], the magnetic field influence is shown to become strong if the electron gyrofrequency exceeds the frequency of the incident radiation in the rest frame of the scattering particles, $\omega_G \equiv eB/mc \gg \omega' \equiv \omega\gamma(1-\beta\cos\theta)$ (where β is the particle velocity in units of the speed of light, $\gamma \equiv \left(1-\beta^2\right)^{-1/2}$ is the Lorentz-factor, θ is the angle between the wavevector of the radiation and the particle velocity). Deep in the magnetosphere, e.g. close to the radio emission region, this condition is well satisfied, and the induced scattering should be treated in the approximation of a strong magnetic field [12]. As the magnetic field strength of a pulsar decreases with distance from the neutron star, $B \propto r^{-3}$, in the outer magnetosphere the radio waves pass through the cyclotron resonance, $\omega' = \omega_G$. The induced scattering in the pulsar wind occurs in the non-magnetic regime [13]. Note that in the resonance region itself the radio waves suffer resonance absorption rather than scattering [12, 14-17].

The induced scattering in the superstrong magnetic field is fist considered in [13], where it is shown to be efficient in the pulsar magnetosphere. Later on this process was involved into the explanation of a number of peculiarities of the observed radio emission of pulsars [18-20]. As is known, the rate of induced scattering depends on the number of photons in the final state and also on the recoil determined by the difference in orientations of the incident and scattered photons. Therefore, the problem of induced scattering in the pulsar magnetospheres can be formulated in different ways, depending on the final state of the scattered radiation considered.

As the pulsar radio emission is concentrated into a narrow beam, in case of the induced scattering inside the beam the recoil is small, whereas the photon occupation numbers in the final state are large. This process can lead to a substantial redistribution of radiation inside the beam and accounts for the observed microstructure of the radio pulses [19]. The scattering of the beam photons over a larger angle may be much more efficient. It will be noted that in the rest frame of the scattering particles the photon frequency is almost unchanged in scattering. Therefore, in the laboratory frame, the photon frequencies and orientations in the initial and final states are related as $\omega_1\gamma(1-\beta\cos\theta_1) = \omega_2\gamma(1-\beta\cos\theta_2)$. The induced scattering between the photon states with substantially different frequencies and orientations may lead to the efficient energy transfer from the low to the high frequency and, because of the decreasing spectrum of the pulsar, cause giant pulses of radio emission [20].

The induced scattering of the beam photons in the direction toward maximum scattering probability is also of interest. This process requires the presence of the background radiation out of the beam. Such radiation may arise, e.g. as a result of the spontaneous scattering of the beam photons. Although the intensity of the background radiation is very small, it can stimulate sufficiently strong induced scattering. Then the beam photons are scattered predominantly in a certain direction, and the intensity in this state may become comparable with the initial intensity of the beam. On a qualitative level, the induced scattering of the directed radio emission of pulsars into the background one was first considered in [18]. The estimates carried out have shown that this process may markedly affect the observed radio emission, especially at low frequencies and account for the low-frequency turnovers in pulsar spectra. The problem of induced scattering of the directed radio emission of a pulsar into the background is treated analytically, the growth rate and orientation of the

scattered component examined, and the scattered component identified with the precursor.

3. INTENSITY TRANSFER IN SCATTERING

The kinetic equation describing the induced scattering of radiation off the particles of the electron-positron plasma in a superstrong magnetic field has the form [13, 18]

$$\frac{\partial n(\vec{k})}{\partial r} = \frac{\hbar r_e^2 n_e n(\vec{k})}{mc} \int \frac{\sin^2\theta \sin^2\theta_1}{\gamma^6 \eta^3 \eta_1^3 \beta^2} \times$$

$$\times \left\{ \frac{(\eta_1 - \eta)^2}{\eta_1^2 \gamma^3} \frac{\partial k_1^2 n_1(\vec{k}_1)}{\partial k_1} + \frac{6k\eta^2 (\eta_1 - \eta) n_1(\vec{k}_1)}{\gamma \eta_1^2} \times \right.$$

$$\left. \times \left[1 - \frac{\eta + \eta_1}{2\gamma^2 \eta \eta_1} \right] \right\} \mathrm{d}\Omega_1, \qquad (1)$$

where $n(\vec{k})$ and $n_1(\vec{k}_1)$ are the photon occupation numbers in the initial and final states with the total number of the photons participating in scattering in the elementary spatial volume being $N \equiv \int n(\vec{k}) \mathrm{d}^3\vec{k} / (2\pi)^3 = \int n_1(\vec{k}_1) \mathrm{d}^3\vec{k}_1 / (2\pi)^3$; the photon trajectory is assumed to be a straight-line and is described by the coordinate r, r_e is the classical electron radius, n_e is the number density of the scattering particles, θ and θ_1 are the inclinations of the initial and final wavevectors to the magnetic field, $\eta \equiv 1 - \beta\cos\theta$ and $\eta_1 \equiv 1 - \beta\cos\theta_1$, $\mathrm{d}\Omega_1$ is the elementary solid angle in the space of the final photon states. In equation (1), the wavevector coordinates before and after scattering are related by the equation

$$k\eta = k_1\eta_1, \qquad (2)$$

which implies the equality of the photon frequencies in the rest frame of the scattering particles. In the problem of scattering in the pulsar magnetosphere the incident radiation is the transverse electromagnetic waves polarized either in the plane of the wavevector and the ambient magnetic field (the ordinary polarization) or perpendicularly to this plane (the extraordinary polarization). It will be noted that in the kinetic equation (1) the occupation numbers n and n_1 refer to the states with the ordinary polarization. In the approximation of a superstrong magnetic field, the scattering involving the photons of the extraordinary polarization is negligible, since the perturbed motion of a particle (in the incident wave field) across the external magnetic field is suppressed.

The pulsar radio emission is characterized by a strong forward directivity: in each point of the pulsar emission cone it is concentrated into a narrow beam of the opening angle $\leq 1/\gamma$, whereas the width of the emission cone itself is typically much larger. Far from the emission region the waves propagate quasitransversely with respect to the ambient magnetic field ($1/\gamma \ll \theta_b \ll 1$, where θ_b is the wavevector inclination to the magnetic field). Therefore one can neglect the beam width, and in each point of the scattering region the incident radiation can be represented by a single wavevector $\vec{k}_b = (k_b, \theta_b, \varphi_b)$. In case of an effective induced scattering, the orientations of the scattered photons $(\theta_{bg}, \varphi_{bg})$ are chiefly close to the direction $\left(\theta_{bg}^{\max}, \varphi_{bg}^{\max}\right)$, which corresponds to the maximum scattering probability at a fixed $\vec{k}_b$. Note that in the approximation of a superstrong magnetic field the induced scattering process is characterized by the azimuthal symmetry.

To find the value of $\theta_{bg}^{\max}$ let us turn to the investigation of the kinetic equation (1). At first, let us consider the evolution of the occupation numbers of the beam, so that $n(\vec{k})$ refers to the beam photons, whereas $n_1(\vec{k}_1)$ to the background photons. Given that $1/\gamma \ll \theta_1 < \theta$ the second term in the curly brackets is $\theta_1^2\gamma^2$ times greater than the first one and scales $\propto \theta_1^{-4}$. Therefore one can expect that the whole integrand peaks at $\theta_{bg}^{\max} \approx 1/\gamma$. Let us analyze more in detail the variation of the occupation numbers at $\theta_{bg} < 1/\gamma$ numerically. Fig. 1 shows the rate of change of the background (Fig. 1, a) and the beam (Fig. 1, b) versus θ_{bg}. Each plot shows both terms in the integrand of the kinetic equation and their sum. The beam is assumed to propagate in a given direction θ_b and have the power-law spectrum, $n(k_b) \propto k_b^{-\mu}$, where μ is the spectral index, while the background radiation has the uniform angular distribution and the same spectrum. To obtain the kinetic equation describing the change of the background occupation numbers in Eq. (1) it is taken that $n(\vec{k})$ corresponds to the background photons, whereas $n_1(\vec{k}_1)$ to the beam photons.

The growth rate of the background occupation numbers $\partial n_{bg} / \partial r$ is maximal at $\theta_{bg} = \theta_{bg}^{\max} \approx 4/\gamma$, with the width of the maximum being $\approx 1/\gamma$ and the second term of the kinetic equation making the dominant contribution (see Fig. 1, a). In our treatment $1/\gamma$ is a small

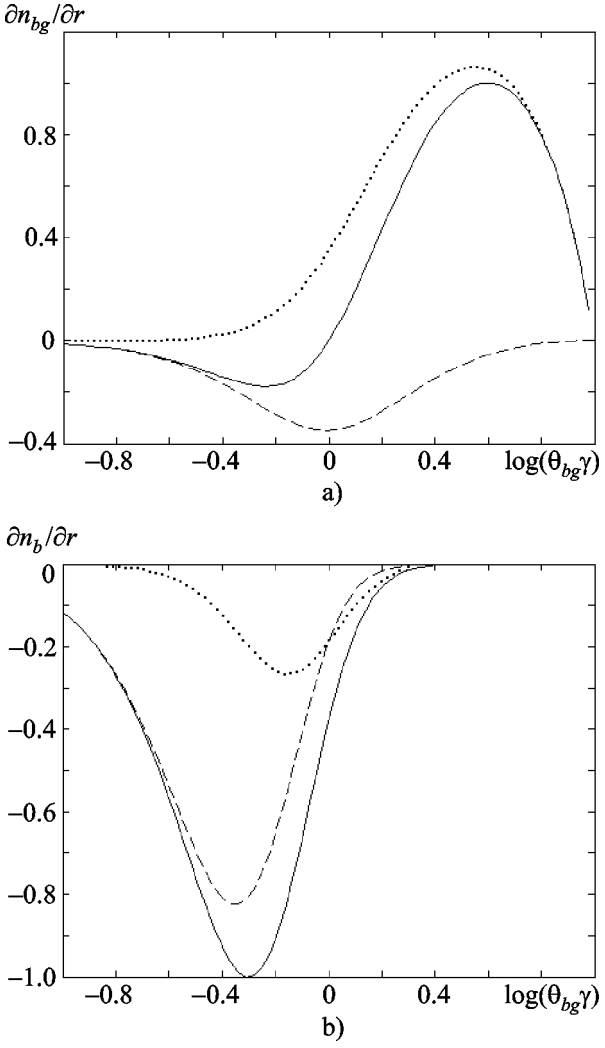

FIG. 1: The rate of change of the photon occupation numbers of the background (a) and the beam (b) versus orientation of the background photons; $\theta_b = 0.1$, $\mu = 5$, $\gamma = 100$. The first terms of the kinetic equations are shown by dashed lines, the second ones by dotted lines and their sum by solid lines. In each plot, the curves are normalized to the maximum modulo of the ordinate of the corresponding total curve

parameter, thus one can neglect the width of the maximum and take that $\theta_{bg} \approx 1/\gamma$. In the kinetic equation for the beam photons, the integrand peaks at somewhat less values of θ_{bg} (see Fig. 1, b). However the rate of change of the beam occupation numbers $\partial n_b/\partial r$ is in fact determined not only by the scattering probability but also by the background occupation numbers, thus the beam photons are most efficiently scattered in the direction $\theta_{bg}^{\max}$ where the background occupation numbers can grow significantly. As can be seen from Fig. 1, b, at $\theta_{bg} = \theta_{bg}^{\max}$ the second term under the integral in the kinetic equation is also larger than the first one. Therefore, the first terms of the both kinetic equations can be neglected.

Thus, let us consider the induced scattering between the two photon states with $\theta \gg 1/\gamma$, $\theta_1 = \theta_{bg}^{\max} \approx 1/\gamma$ and the frequencies related, in accordance with Eq. (2), by $\omega_1 = \omega\eta/\eta_1 \approx \omega\theta^2\gamma^2 \gg \omega$. It will be noted that the pulsar emission cone is much wider than the direction diagram in each point, so that the transverse size of the scattering region is much larger than the cross-section of the photon beam. Then, although in the problem considered the latter is negligible, the transverse size of the scattering region is still large enough not to impose substantial restrictions on the evolution of the photon occupation numbers. It is convenient to introduce the intensities $i_{\nu_a} = \hbar\omega^3 n(\vec{k})/2\pi^2c^2$ and $i_{\nu_b} = \hbar\omega_1^3 n(\vec{k}_1)/2\pi^2c^2$, where $\nu_a = \omega/2\pi$, $\nu_b = \omega_1/2\pi$ and the angular distributions are described by the δ-functions. Performing integration over the solid angle, let us proceed to the spectral intensities $I_{\nu_{a,b}} \equiv \int i_{\nu_{a,b}} \mathrm{d}\Omega_{a,b}$. Intensity variation of the beam and the background in the course of induced scattering is approximately described by the following set of equations (see also [20]):

$$\frac{\mathrm{d}I_{\nu_a}}{\mathrm{d}r} = -aI_{\nu_a}I_{\nu_b}, \qquad \frac{\mathrm{d}I_{\nu_b}}{\mathrm{d}r} = aI_{\nu_a}I_{\nu_b}, \tag{3}$$

where

$$a \approx \frac{24n_e r_e^2}{m\nu_a^2\gamma^5\theta^4}. \tag{4}$$

Taking notice that $I_{\nu_a} + I_{\nu_b} \equiv I = \mathrm{const}$, from Eq. (3) we obtain the following equation for the function $u \equiv I_{\nu_a}/I_{\nu_b}$:

$$\frac{\mathrm{d}u}{\mathrm{d}r} = -Iau,$$

thus

$$u = u^{(0)} \exp(-Iar)$$

and the set of equations (3) is solved as

$$I_{\nu_a} = \frac{I\left[I^{(0)}_{\nu_a} \big/ I^{(0)}_{\nu_b}\right]\exp(-Iar)}{1+\left[I^{(0)}_{\nu_a} \big/ I^{(0)}_{\nu_b}\right]\exp(-Iar)}\,,$$

$$I_{\nu_b} = \frac{I}{1+\left[I^{(0)}_{\nu_a} \big/ I^{(0)}_{\nu_b}\right]\exp(-Iar)}\,, \qquad (5)$$

where $I^{(0)}_{\nu_a}$ and $I^{(0)}_{\nu_b}$ are the initial intensities of the beam and the background, respectively. Thus, in the approximation considered the total intensity of the two beams remains constant. For the exact solution this relation is violated, since the total number of the photons participating in scattering is conserved, while the energy of emission is partially transferred to the scattering particles. Our result means that the intensity redistribution between the beams holds much more rapidly than the variation of the total intensity I, and hereafter we are interested only in this process. As can be seen from Eqs. (3) and (5), the photon frequency increases, $\nu_b \gg \nu_a$, and they are directed almost along the external magnetic field and the velocity of the scattering particles, $\theta_1 \approx 1/\gamma$. This differs substantially from the case of induced scattering in the absence of magnetic field, in which case the kinetic equation contains only the term analogous to the first term in equation (1), the photons are scattered mainly in the direction antiparallel to the particle velocity and their frequencies are decreasing monotonically.

As can be seen from Eq. (5), the efficiency of induced scattering is characterized by the quantity $\Gamma \equiv Iar$, whereas the extent of intensity transfer from the beam to the background by the quantity $\xi \equiv \left[I^{(0)}_{\nu_b} \big/ I^{(0)}_{\nu_a}\right]\exp(\Gamma)$. At $\xi \ll 1$ the intensities of the beam and the background are $I_{\nu_a} \approx I^{(0)}_{\nu_a}$ and $I_{\nu_b} \approx I^{(0)}_{\nu_b}\exp(\Gamma)$, respectively. At $\xi \approx 1$ the quantity I_{ν_b} becomes comparable with $I^{(0)}_{\nu_a}$ and its growth reaches the stage of saturation. At $\xi \gg 1$ the intensities take the form $I_{\nu_b} \approx I^{(0)}_{\nu_a}$ and $I_{\nu_a} \approx I^{(0)}_{\nu_a}/\xi$. Since the background intensity is very low initially, $\log I^{(0)}_{\nu_b} \big/ I^{(0)}_{\nu_a} \approx -10$, to provide $\xi \approx 1$ it is necessary that $\Gamma = n \times 10$, where n is the quantity of order unity. In this case a substantial part of the beam intensity is transferred to the background.

4. NUMERICAL ESTIMATE OF THE SCATTERING EFFICIENCY

Let us estimate the efficiency of induced scattering in a pulsar magnetosphere. Since $I = I^{(0)}_{\nu_a} + I^{(0)}_{\nu_b} \approx I^{(0)}_{\nu_a}$, then $\Gamma \approx I^{(0)}_{\nu_a} ar$, where a is given by equation (4). The radio emission spectrum of a pulsar typically has a power-law form,

$$I^{(0)}_{\nu_a} = I_{\nu_0}\left(\frac{\nu}{\nu_0}\right)^{-\alpha}. \qquad (6)$$

Here α is the spectral index and the spectral intensity at frequencies $\nu_0 \approx 100$ MHz is related to the pulsar radio luminosity L as

$$I_{\nu_0} = \frac{L}{\nu_0 S}, \qquad (7)$$

where $S = \pi r^2 w^2/4$ is the sectional area of the pulsar emission cone at the distance r from the neutron star and w is the pulsar beam width in the angular measure. It is convenient to normalize the scattering particles number density to the Goldreich–Julian number density:

$$n_e = \frac{\kappa B}{Pce}, \qquad (8)$$

where κ is the multiplicity factor of the plasma and P is the pulsar period. The pulsar magnetic field is assumed to have a dipole structure, hence $n_e \propto B \propto r^{-3}$. Using equations (6)-(8), one can estimate the scattering efficiency:

$$\Gamma = 10P^{-1}L_{28}B_{*_{12}}\kappa_2\gamma_2^{-1}\nu_8^{-2-\alpha}\hat{w}^{-2}(\theta_{-1}\gamma_2 r_8)^{-4}, \qquad (9)$$

where B_* is the magnetic field strength at the neutron star surface, the stellar radius is taken to be 10^6 cm and all the quantities entering Eq. (9) are normalized to their characteristic values: $L_{28} = L/10^{28}$ erg·s^{-1}, $B_{*_{12}} = B_*/10^{12}$ G, $\kappa_2 = \kappa/10^2$, $\gamma_2 = \gamma/10^2$, $\nu_8 = \nu_a/10^8$ Hz, $\hat{w} = w/0.4$, $\theta_{-1} = \theta/0.1$, and $r_8 = r/10^8$ cm. One can see that the scattering efficiency may run up to a few tens, thus the intensity transfer from the beam to the background can indeed be efficient.

5. ORIENTATION OF THE SCATTERED COMPONENT

To determine the location of the scattered component on the radio pulse profile let us first determine the site of the scattering region in the pulsar magnetosphere. According to Eq. (9), the explicit dependence of the scattering efficiency on altitude above the neutron star is sufficiently strong, $\Gamma \propto r^{-4}$. However the implicit dependence on r appears still stronger. Since $\theta \propto r$ (see below), then $\nu_a = \nu_b/\theta^2\gamma^2 \propto r^{-2}$. Indeed, the background emission of a given frequency ν_b is fed by the emission of different frequencies ν_a which satisfy the condition $\nu_b = \nu_a\theta^2(r^2)\gamma^2$ at different altitudes. The larger the altitude, the lower is the frequency ν_a, the larger the intensity of the incident radiation (see equation (6)) and the stronger the scattering. Taking into account these considerations, we have $\Gamma \propto r^{2\alpha-4}$. For the pulsars with precursors $\alpha > 2$, thus the scattering efficiency increases with distance from the neutron star. Note also that the original spectra of radio pulsars may be steeper than those observed, since the induced scattering is stronger at low frequencies (see equation (9)) and, consequently, may lead to flattening the observed spectrum.

Thus, the induced scattering is most efficient near the upper boundary of the scattering region, at distances of order of the cyclotron resonance radius r_c. This quantity is determined from the condition $2\pi\nu_a\gamma\theta^2/2 = \omega_G$ and equals

$$\frac{r_c}{r_L} = 0.4B_{*_{12}}^{1/5}(\gamma_2\nu_8)^{-1/5}P^{-3/5}, \qquad (10)$$

where $r_L \equiv c/\Omega$ is the light cylinder radius, Ω is the angular velocity of the neutron star rotation, and it is taken that $\theta = r/2r_L$ (see below). As can be seen from estimate (10), the region of cyclotron resonance typically lies in the outer magnetosphere of a pulsar, at distances of order of the light cylinder radius.

Now let us turn to analyzing the location of the scattered component on the pulse profile. Since the scattering region lies well above the radio emission one, the observed geometry of the rays is mainly determined by the effect of magnetosphere rotation. For the sake of simplicity we dwell on the case when the pulsar magnetic axis is perpendicular to its rotation axis. Let a ray directed approximately along the magnetic axis be emitted at the start time at point O (see Fig. 2). For the time $t = r/c$ the ray comes to the point of scattering S, whereas the magnetic axis turns by the angle $\Omega r/c = r/r_L$. The polar angle of the ray with respect to the instantaneous orientation of the magnetic axis is $\chi = r/r_L$, and under the assumption of the dipolar structure of the magnetic field the angle between the unit vector of the magnetic field strength $\vec{b}$ and the magnetic axis equals $3\chi/2$. In the corotating frame of the neutron star the wavevector of the scattered radiation is almost co-directed with $\vec{b}$, while in the observer's frame it is shifted by the angle r/r_L in the direction of rotation due to rotational aberration.

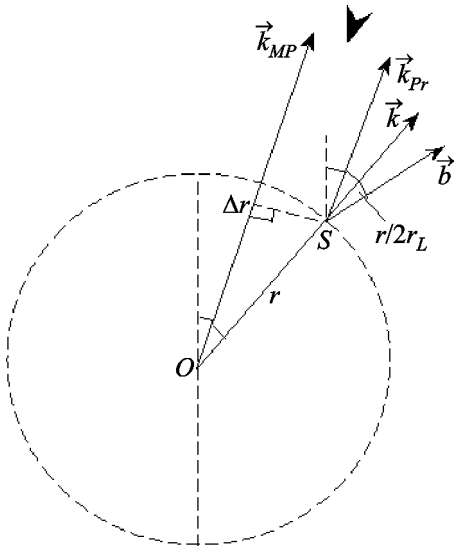

FIG. 2: Scattering geometry in the magnetosphere of a pulsar; $\vec{k}_{MP}$ and $\vec{k}_{Pr}$ are the wavevectors of the main pulse and precursor emission, respectively

In total, the difference of longitudes of the main pulse and the scattered component equals

$$\lambda_{MP} - \lambda_{Pr} = \frac{r}{2r_L}. \quad (11)$$

Note that the magnetosphere rotation leads to deformation of the dipolar magnetic field, however the change of orientation of a field line in a fixed point of the field line tube is the effect of the second order in r/r_L and in our consideration it can be neglected. Furthermore, as can be seen from Fig. 2, the precursor emission passes a somewhat larger distance to the observer than the main pulse emission, $\Delta r = r\left[1-\cos\left(r/2r_L\right)\right]$, however this effect changes the difference of longitudes by the quantity $\propto \left(r/r_L\right)^3 \ll r/r_L$ and is also neglected here.

According to Eq. (11), the distance from the precursor to the main pulse on the pulse profile is proportional to the scattering region altitude. The maximum difference of the component longitudes, $\Delta\lambda \approx 30°$, is reached at $r \approx r_L$.

6. DISCUSSION OF THE RESULTS

In our treatment, it is shown that in the pulsar magnetosphere the induced scattering of radio emission into the background in the approximation of a superstrong magnetic field can be efficient. Then a substantial part of the radio beam energy can be transferred to the scattered component. The wavevectors of the scattered radiation are directed approximately along the external magnetic field, and, as a result of rotational aberration in the scattering region, the scattered component appears on the pulsar profile somewhat earlier than the main pulse. It is of interest to compare the physical properties of the scattered radiation with the observed features of the precursors.

In the approximation of a superstrong magnetic field, only the photons of the ordinary polarization are involved in scattering. Correspondingly, the scattered component should be characterized by a high degree of linear polarization. This is indeed a distinctive feature of the precursor emission. Since the position angle of linear polarization is determined by the magnetic field orientation in the region of radio emission formation and the main pulse and the precursor originate at different altitudes in the magnetosphere, the values of the position angle in these components may differ markedly. Such a difference is observed, e.g. in the pulsar B1822-09 [3]. Moreover, if the main pulse is dominated by the emission of the extraordinary polarization, then the position angle of the precursor should show an extra shift by $90°$, as is really the case in the Vela pulsar [4].

The precursors are known to be met in the pulsars with relatively strong magnetic fields at the neutron star surface (see, e.g. [3]). As can be seen from equation (9), the efficiency of induced scattering is proportional to B_*, thus a marked growth of the scattered component can indeed be expected in pulsars with strong magnetic field. Furthermore, our estimate of Γ shows that the precursor presence should be characteristic of the short-period pulsars with high enough radio luminosities.

The efficiency of induced scattering, which determines the scattered component growth, may strongly vary from pulse to pulse because of fluctuations of both the intensity of incident radiation and the parameters of the scattering particles. If the main pulse emission is dominated by the waves of the ordinary polarization and the scattering is very strong ($\xi \gg 1$), this emission may be almost completely transferred to the scattered component. Probably, this is the case in the pulsar J1326-6700, when occasionally the main pulse intensity drops below the detection level and a strong precursor arises on the profile [8]. In the pulsar B1822-09, on the contrary, the precursor is visible only in strong pulses [3, 6, 7]. In case of moderately strong scattering, $\xi \approx 1$, the intensity of the scattered component grows exponentially, $I_{\nu_b} \approx I^{(0)}_{\nu_b} \exp\left(I^{(0)}_{\nu_a} ar\right)$, whereas the beam intensity is almost unaltered, $I_{\nu_a} \approx I^{(0)}_{\nu_a}$, so that with the fluctuations of $I^{(0)}_{\nu_a}$ the intensities I_{ν_b} and I_{ν_a} are correlated. In the individual pulses of the Vela pulsar, stronger precursors exhibit larger separations from the main pulse [4]. Larger separations between the components imply larger altitudes of the scattering region, $\Delta\lambda \propto r$. In this case, the beam angle of incidence is also larger, $\theta_b \propto r$, and at a fixed frequency the precursor is formed due to scattering of the lower-frequency radiation, $\nu_a = \nu_b / \theta^2(r)\gamma^2$, which is much more intensive.

As estimate (9) can show, the efficiency of induced scattering strongly increases with the frequency decrease, so that the precursor spectrum should be steeper than that of the main pulse. The precursor of the Crab pulsar really has a very steep spectrum, $\alpha \geq 5$ [3]. The flat spec-

trum of the pulsar B1822-09 [3] can be explained by scattering the main pulse emission beyond the low-frequency turnover, which starts at frequencies ≈ 100 MHz, whereas in the Crab pulsar the power-law segment of the spectrum extends down to the frequencies ≈ 10 MHz.

7. CONCLUSIONS

The induced scattering of radio emission off the particles of the ultrarelativistic electron-positron plasma in the approximation of a superstrong magnetic field is considered. Scattering a narrow beam into the background in the open field line tube of a pulsar is considered. The scattered radiation is found to be concentrated in the direction close to the velocity vector of the scattering particles, its frequency being well above that of the incident radiation, $\nu_b \approx \nu_a \theta^2 \gamma^2 \gg \nu_a$. In scattering, the intensity of the scattered component may grow substantially, the total intensity of the beam and the background being approximately conserved. In the limiting case of extremely strong scattering $I_{\nu_b}(\nu_b) \approx I^{(0)}_{\nu_a}(\nu_a)$ and, on condition of the decreasing spectrum of the pulsar radio emission, $I^{(0)}_{\nu_a}(\nu) \propto \nu^{-\alpha}$, the intensity of the scattered component, $I_{\nu_b}(\nu_b)$, may exceed the beam initial intensity at the same frequency, $I^{(0)}_{\nu_a}(\nu_b)$.

The region of an efficient induced scattering at a superstrong magnetic field lies in the outer magnetosphere of a pulsar, at distances comparable with the cyclotron resonance radius. As a result of rotational aberration, the scattered component precedes the main pulse by $10 \div 20°$ in pulse longitude and can be identified with the pulsar precursor. The suggested mechanism of the precursor formation based on the induced scattering of the main pulse emission explains the physical connection of the two components as well as a number of the observed features of the precursor emission, in particular, high linear polarization of this component.

REFERENCES

1. Campbell, D. B., Heiles, C., Rankin, J. M., Pulsar NP 0532: Average polarization and daily variability at 430 MHz, *Nature*, 225:527-528, 1970.
2. McCulloch, P. M., Hamilton, P. A., Ables, J. G., Komesaroff, M. M., PSR 1055-52-A pulsar resembling the Crab Nebula pulsar, *Mon. Notic. Roy. Astron. Soc.*, 175: 71P-75P, 1976.
3. Fowler, L. A., Wright, G. A. E., Morris, D., Unusual properties of the pulsar PSR 1822-09, *Astron. and Astrophys.*, 93:54-61, 1981.
4. Krishnamohan, S., Downs, G. S., Intensity dependence of the pulse profile and polarization of the VELA pulsar, *Astrophys. J.*, 265:372-388, 1983.
5. Manchester, R. N., Observations of the Crab pulsar at 410 and 1664 MHz, *Astrophys. J.*, 163:L61-L63, 1971.
6. Fowler, L. A., Wright, G. A. E., Pulse-interpulse interaction in pulsar PSR 1822-09, *Astron. and Astrophys.*, 109(2):279-281, 1982.
7. Gil, J. A., Jessner, A., Kijak, J., Kramer, M., Malofeev, V., Malov, I., Seiradakis, J. H., Sieber, W., Wielebinski, R., Multifrequency study of PSR 1822-09, *Astron. and Astrophys.*, 282(1):45-53, 1994.
8. Wang, N., Manchester, R. N., Johnston, S., Pulsar nulling and mode changing, *Mon. Notic. Roy. Astron. Soc.*, 377(3):1383-1392, 2007.
9. Dyks, J., Zhang, B., Gil, J., Reversals of radio emission direction in PSR B1822-09, *Astrophys. J.*, 626(1):L45-L47, 2005.
10. Gurevich, L. E. and Pavlov, S. T., Electromagnetic wave scattering off free electrons in a strong magnetic field, *Zhurnal Tekhnicheskoi Fiziki*, 30(1):41-43, 1960 (in Russian).
11. Canuto, V., Lodenquai, J., Ruderman, M., Thomson scattering in a strong magnetic field, *Phys. Rev. D.*, 3:2303-2308, 1971.
12. Blandford, R. D., Scharlemann, E. T., On the scattering and absorption of electromagnetic radiation within pulsar magnetospheres, *Mon. Notic. Roy. Astron. Soc.*, 174:59-85, 1976.
13. Wilson, D. B., Rees, M. J., Induced Compton scattering in pulsar winds, *Mon. Notic. Roy. Astron. Soc.*, 185:297-304, 1978.
14. Lyubarskii, Yu. E., Petrova, S. A., Synchrotron absorption in pulsar magnetospheres, *Astron. and Astrophys.*, 337:433-440, 1998.
15. Luo, Q., Melrose, D. B., Cyclotron absorption of radio emission within pulsar magnetospheres, *Mon. Notic. Roy. Astron. Soc.*, 325(1):185-196, 2001.
16. Petrova, S. A., The effect of synchrotron absorption on the observed radio luminosities of pulsars, *Mon. Notic. Roy. Astron. Soc.*, 336(3):774-784, 2002.
17. Fussell, D., Luo, Q., Melrose, D. B., Cyclotron absorption in rotating pulsar magnetospheres, *Mon. Notic. Roy. Astron. Soc.*, 343(4):1248-1256, 2003.
18. Lyubarskii, Yu. E., Petrova, S. A., Stimulated scattering of radio emission in pulsar magnetospheres, *Astron. Letters*, 22(3):399-408, 1996.
19. Petrova, S. A., Toward explanation of microstructure in pulsar radio emission, *Astron. and Astrophys.*, 417:L29-L32, 2004.
20. Petrova, S. A., On the origin of giant pulses in radio pulsars, *Astron. and Astrophys.*, 424:227-236, 2004.

Radio Physics and Radio Astronomy, 1(1), 27–35 (2010)

THE MECHANISM OF COMPONENT FORMATION OUT OF THE MAIN PULSE OF A RADIO PULSAR. II. THE INTERPULSE

S. A. Petrova

Institute of Radio Astronomy, National Academy of Sciences of Ukraine, 4, Chervonopraporna St., Kharkiv 61002, Ukraine

*Address all correspondence to S. A. Petrova E-mail:petrova@ri.kharkov.ua

The theory of induced scattering off the ultrarelativistic particles in a moderately strong magnetic field is developed. The kinetic equations obtained are applied to the problem of induced scattering of pulsar radiation out of the narrow beam. It is shown that the scattered radiation concentrates predominantly in the direction antiparallel to the velocity of the scattering particles. Based on this process, we first suggest a physical mechanism of the interpulse component of a pulsar. Our model explains the observed spectral and polarization peculiarities of the interpulse emission as well as its connection to the main pulse.

KEY WORDS: *pulsar, pulse, fluctuation, intensity magnetosphere, kinetic equations, induced scattering*

1. INTRODUCTION

Some pulsars have an interpulse, or a component located approximately half way between the main pulses. This component is met in the short-period pulsars, with periods ≤ 0.6 s [1], and it is especially abundant in the millisecond pulsars: among the known pulsars, the interpulses are present in 2 % of the normal pulsars and in 40 % of the millisecond ones [2]. In many cases, the interpulse intensity is only a few per cent of that of the main pulse. The spectral and polarization properties of the interpulse emission are also distinct. As a rule, the interpulse spectrum is steeper than that of the main pulse, so that the interpulse component is most pronounced at low frequencies [3-5]. The interpule emission is characterized by a high degree of linear polarization, with the position angle being almost unaltered across the component [6].

The interpulse intensity can be modulated at different timescales. Similarly to the main pulses, the interpulses may exhibit a number of fluctuation phenomena, such as the microstructure [7, 8], the subpulse modulation [9], the pulse-to-pulse intensity fluctuations [10], the emission mode switching [11-13] and giant pulses [14-17]. Recently it has been discovered that the subpulse modulation in the interpulse of the pulsar B1702-19 is characterized by the same quasi-periodicity as does the modulation in the trailing part of the main pulse, the variations of the modulation in the two components being identical [9]. This clearly testifies to the physical connection between the main pulse and the interpulse.

In the literature, several geometrical models of the interpulse formation are considered. It is usually taken that the interpulses come from the pulsars, in which the magnetic axis is almost perpendicular to the rotation axis, so that the observer catches the emission from the both magnetic poles of the neutron star [18]. However, in this two-pole model it is difficult to explain the connection of the component emission. It was also suggested to identify the main pulse and the interpulse

ISSN 2152-274X

with a pair of widely spaced conal components [1]. In this case, the unusually wide emission cone can be attributed either to the location of the radio emission region at high altitudes in the magnetosphere or to the small inclination of the magnetic axis to the pulsar rotation axis. In these single-pole models, however, a substantial distinction of the component intensities remains unclear. This difficulty was partially overcome in another version of the single-pole model [19], where the pulsar radio beam was assumed to present two co-axial hollow cones, the outer and inner ones, with the axes along the magnetic axis, the latter being almost aligned with the pulsar rotation axis. Then the main pulse and interpulse were identified with the outer and inner conal components. This model explains the geometry of the pulsar B0826-34 rather well, however, it does not bear generality.

Recently, the bi-directional model was proposed [20] in order to explain the profile of the pulsar B1822-09. The main pulse and interpulse are suggested to originate above one pole, but at different altitudes, with the interpulse emission being directed backward, to the neutron star, whereas the main pulse emission forward, as usual. For the two components to be visible to the observer, the pulsar magnetic axis should be almost perpendicular to the rotation axis. The mechanism of the emission directed to the neutron star was not discussed. Furthermore, the assumpiton of independent generation of the main pulse and interpulse in widely separated regions contradicts the observed anticorrelation of the component intensities [11-13].

In this paper, the physical mechanism of the interpulse formation is first suggested. In contrast to the preceding geometrical models, it explains the spectral and polarization peculiarities of the interpulse emission and also its connection to the main pulse emission. In [21], we have considered the formation of another component outside of the main pulse of a pulsar – the precursor – based on the induced scattering of ther main pulse emission into the background. It was shown that in the approximation of a superstrong magnetic field the scattered component is almost aligned with the field and because of rotational aberration in the scattering region appears on the pulse profile ahead of the main pulse. Here, we extend the theory of magnetic induced scattering to the case of a moderately strong magnetic field and, making use of the kinetic equations obtained, solve the problem of the induced scattering out of a narrow beam. It is shown that in the case considered the main pulse emission is mainly scattered backward – in the direction antiparallel to the velocity of the scattering particles – and forms the component separated from the main pulse approximately twice as nearer as the pulsar period.

2. PROBLEM STATEMENT

The pulsar magnetosphere is filled with the ultrarelativistic electron-positron plasma, which streams along the open magnetic field lines. As the radio emission is generated deep in the open field line tube, it should propagate through the plasma flow. The brightness temperatures of the pulsar radio emission are very high, so that the induced scattering off the plasma particles may be efficient.

The external magnetic field affects the scattering process given that the frequency of radiation in the rest frame of the scattering particles is much lower than the electron gyrofrequency, $\omega' \equiv \omega\gamma(1-\beta\cos\theta) \ll \omega_G \equiv eB/(mc)$ (here ω' and ω are the frequencies of the incident radiation in the particle rest frame and the laboratory frame, respectively, β is the particle velocity in units of the speed of light, $\gamma \equiv \left(1-\beta^2\right)^{-1/2}$ is their Lorentz-factor, θ is the angle between the wavevector of the incident radiation and the magnetic field, B is the magnetic field strength). The region of cyclotron resonance of radio frequencies, $\omega' = \omega_G$, usually lies in the outer magnetosphere of a pulsar, at distances of order of the light cylinder radius, and at lower altitudes in the open field line tube the magnetic field influence on scattering is significant.

In the literature, two regimes of the spontaneous magnetic scattering are considered: the longitudinal and transverse ones [22, 23]. The longitudinal scattering occurs in a superstrong magnetic field, in which case the velocity of the perturbed motion of the particle in the field of the incident wave is aligned with the field line of the external field. The transverse scattering regime corresponds to moderately strong magnetic fields, when the perturbed motion of the particle is a drift in the crossed fields – in the electric field of the incident wave and in the external magnetic field. If the incident emission is inclined at an angle $1/\gamma \ll \theta < 1$ to the magnetic field, the longitudinal scattering holds

on condition that $\omega'/\omega_G \ll 1/(\theta\gamma)$, and the transverse one on condition that $1/(\theta\gamma) \ll \omega'/\omega_G \ll 1$ [23].

As a rule, at the conditions of the pulsar magnetosphere both regimes of the magnetic scattering are realized. The induced scattering in the longitudinal regime is considered in [21, 22, 24-26], and it is shown that this process may have a number of important observational consequences. The transverse induced scattering is discussed qualitatively in [22]. In our paper, the kinetic equation describing the transverse induced scattering is derived and the problem of the induced scattering out of a narrow beam is solved.

3. BASIC FORMALISM

Let the emission in the form of transverse electromagnetic waves falls on the system of relativistic particles. The induced scattering will be treated in the laboratory frame. In a general form, the kinetic equation for the induced scattering off the hot electrons in the magnetic field is obtained in [22]. Following this work, we shall repeat the derivation of the kinetic equation in order to correct the error made by the authors. The evolution of the occupation numbers in the course of induced scattering in the magnetic field can be written in the form

$$\frac{\mathrm{d}n(\vec{k})}{\mathrm{dt}}\frac{\mathrm{d}^3\vec{k}}{(2\pi)^3} = \int\left[f(p+\Delta p)-f(p)\right]\frac{\mathrm{d}P}{\mathrm{d}t}n_1(\vec{k}_1)\mathrm{d}p, \quad (1)$$

where $n(\vec{k})$ and $n_1(\vec{k}_1)$ are the photon occupation numbers in the initial and final states, $\int n(\vec{k})\,\mathrm{d}^3\vec{k}/(2\pi)^3 = \int n_1(\vec{k}_1)\,\mathrm{d}^3\vec{k}_1/(2\pi)^3 \equiv N$ is the total number of the photons involved in scattering, $f(p)$ is the distribution function of the scattering particles in momenta, $\int f(p)\mathrm{d}p \equiv n_e$ is the number density of the scattering particles, Δp is the momentum increment in the elementary scattering act, $\mathrm{d}P/\mathrm{d}t$ is the probability of emitting a scattered photon by an electron in the unit time. Here it is taken into account that in a strong magnetic field the transverse component of the momentum is almost immediately lost because of synchrotron re-emission, so that the particles perform one-dimensional motion along the field line. Note that in equation (21) from [22], which is analogous to our equation (1), the distribution function in Lorentz-factors, $N(\gamma)$ stands instead of $f(p)$, which is incorrect. Indeed, since $p \equiv \beta\gamma mc$, then $N(\gamma) = f(p)\,\mathrm{d}p/\mathrm{d}\gamma = mcf(p)/\beta$, where β is also an implicit function of p, i.e. $\beta(p+\Delta p) \neq \beta(p)$.

In the scattering process, the longitudinal component of the momentum is conserved:

$$\Delta p = \hbar k\cos\theta - \hbar k_1\cos\theta_1. \quad (2)$$

The probability of emitting the scattered photon is

$$\frac{\mathrm{d}P}{\mathrm{d}t} = n(\vec{k})c^4\eta\frac{\mathrm{d}\sigma}{\mathrm{d}\Omega_1}\frac{\mathrm{d}^3\vec{k}}{(2\pi)^3}\frac{\mathrm{d}^3\vec{k}_1}{\omega_1^2}\delta\left(\omega_1 - \frac{\eta}{\eta_1}\omega\right), \quad (3)$$

where $\eta \equiv 1-\beta\cos\theta$, $\eta_1 \equiv 1-\beta\cos\theta_1$, $\mathrm{d}\sigma/\mathrm{d}\Omega_1$ is the differential cross-section of scattering, $\mathrm{d}\Omega_1$ is the elementary solid angle in the space of the wavevectors of the scattered photons and the argument of the δ-function means equality of the frequencies of the initial and final states in the rest frame of the scattering particles, $\omega\gamma\eta = \omega_1\gamma\eta_1$.

In the kinetic equation (1), $\mathrm{d}/\mathrm{d}t \equiv \partial/\partial t + c\,\partial/\partial r$, where r is the coordinate along the photon trajectory. We assume the straight-line photon propagation and consider the stationary case, omitting the explicit temporal dependence of the quantities. Taking into account that $f(p+\Delta p) - f(p) \approx \Delta p\,\partial f/\partial p$, and integrating equation (1) by parts, we obtain

$$c\frac{\partial n}{\partial r}\frac{\mathrm{d}^3\vec{k}}{(2\pi)^3} = -\int\frac{\partial}{\partial p}\left(\Delta p n_1\frac{\mathrm{d}P}{\mathrm{d}t}\right)f\mathrm{d}p. \quad (4)$$

Changing to the distribution function in Lorentz-factors, substituting equations (2) and (3) into (4) and integrating over k_1 with the help of δ-function, we find finally:

$$\frac{\partial n}{\partial r} = \int\mathrm{d}\gamma F(\gamma)\frac{\beta\hbar\omega}{mc^2}\int(\cos\theta_1 - \cos\theta)\frac{\partial}{\partial\gamma}\left(nn_1\frac{\mathrm{d}\sigma}{\mathrm{d}\Omega_1}\right)\mathrm{d}\Omega_1. \quad (5)$$

Here $F(\gamma)$ is chosen to obey the normalization $\int F(\gamma)\,\mathrm{d}\gamma = n_e$.

The kinetic equation (5) describes the photon transfer in the course of induced scattering in a strong magnetic field. As applied to pulsars, the scattering far from the emission region is considered, in which case the characteristic plasma frequency is already much lower than the emission frequency, $\omega \gg \omega_p\sqrt{\gamma} \equiv \sqrt{4\pi n_e e^2\gamma/m}$. Then the collective effects can be neglected and the incident radiation appears to be the transverse electromagnetic waves, whose electric vector either lies in the same plane as the wavevector and the external magnetic field (the ordinary, or A-polarization) or is perpendicular to this plane (the extraordinary, or B-polarization).

In the rest frame of the scattering particles, the scattering cross-section in the magnetic field has the form [27]

$$\frac{d\sigma^{AA}}{d\Omega_1'} = r_e^2 \sin^2\theta'\sin^2\theta_1' + \frac{r_e^2\cos^2\theta'\cos^2\theta_1'}{\left(1-\omega_G^2/\omega'^2\right)^2}\times$$

$$\times\left(\cos^2\Delta\phi' + \frac{\omega_G^2}{\omega'^2}\sin^2\Delta\phi'\right)+$$

$$+2\frac{r_e^2}{1-\omega_G^2/\omega'^2}\sin\theta'\sin\theta_1'\cos\theta'\cos\theta_1'\cos\Delta\phi',$$

$$\frac{d\sigma^{AB}}{d\Omega_1'} = \frac{r_e^2\cos^2\theta'}{\left(1-\omega_G^2/\omega'^2\right)^2}\left(\sin^2\Delta\phi' + \frac{\omega_G^2}{\omega'^2}\cos^2\Delta\phi'\right),$$

$$\frac{d\sigma^{BA}}{d\Omega_1'} = \frac{r_e^2\cos^2\theta_1'}{\left(1-\omega_G^2/\omega'^2\right)^2}\left(\sin^2\Delta\phi' + \frac{\omega_G^2}{\omega'^2}\cos^2\Delta\phi'\right), \qquad (6)$$

$$\frac{d\sigma^{BB}}{d\Omega_1'} = \frac{r_e^2}{\left(1-\omega_G^2/\omega'^2\right)^2}\left(\cos^2\Delta\phi' + \frac{\omega_G^2}{\omega'^2}\sin^2\Delta\phi'\right).$$

Here the superscripts of σ denote the polarization type of the emission in the initial and final states, primes mark the quantities in the particle rest frame, r_e is the classical electron radius, (θ',ϕ') and (θ_1',ϕ_1') are the spherical coordinates of the wavevectors $\vec{k}'$ and $\vec{k}_1'$ in the system with the polar axis along the external magnetic field, $\omega' = \omega_1'$ and $\Delta\phi' \equiv \phi' - \phi_1'$. In the superstrong magnetic field, at $\omega_G \to \infty$, only one of the cross-sections (6) does not vanish:

$$\frac{d\sigma^{AA}}{d\Omega_1'} = r_e^2\sin^2\theta'\sin^2\theta',$$

which describes scattering in the longitudinal regime. Below we consider the induced scattering in somewhat weaker magnetic fields for the frequencies much lower than the resonance one, $\omega' \ll \omega_G$.

4. KINETIC EQUATIONS FAR OFF THE RESONANCE

Far off the resonance, one can develop the cross-sections (6) into a series in ω'^2/ω_G^2 and examine the induced scattering in a moderately strong magnetic field. Retaining the terms $\propto \omega'^4/\omega_G^4$, we obtain the following expressions for the cross-sections:

$$\frac{d\sigma^{AA}}{d\Omega_1'} \approx r_e^2\sin^2\theta'\sin^2\theta_1' + r_e^2\frac{\omega'^2}{\omega_G^2}\cos^2\theta'\cos^2\theta_1'\times$$

$$\times\left[\sin^2\Delta\phi' + \frac{\omega'^2}{\omega_G^2}\left(1+\sin^2\Delta\phi'\right)\right]-$$

$$-r_e^2\frac{\omega'^2}{2\omega_G^2}\left(1+\frac{\omega'^2}{\omega_G^2}\right)\sin 2\theta'\sin 2\theta_1'\cos\Delta\phi',$$

$$\frac{d\sigma^{AB}}{d\Omega_1'} \approx r_e^2\frac{\omega'^2}{\omega_G^2}\cos^2\theta'\left[\cos^2\Delta\phi' + \frac{\omega'^2}{\omega_G^2}\left(1+\cos^2\Delta\phi'\right)\right], \qquad (7)$$

$$\frac{d\sigma^{BA}}{d\Omega_1'} \approx r_e^2\frac{\omega'^2}{\omega_G^2}\cos^2\theta_1'\left[\cos^2\Delta\phi' + \frac{\omega'^2}{\omega_G^2}\left(1+\cos^2\Delta\phi'\right)\right],$$

$$\frac{d\sigma^{BB}}{d\Omega_1'} \approx r_e^2\frac{\omega'^2}{\omega_G^2}\left[\sin^2\Delta\phi' + \frac{\omega'^2}{\omega_G^2}\left(1+\sin^2\Delta\phi'\right)\right].$$

By making use of the relativistic transformations

$$\omega' = \omega\gamma\eta, \qquad \Delta\phi' = \Delta\phi, \qquad d\Omega_1' = \frac{d\Omega_1}{\gamma^2\eta_1^2},$$

$$\cos\theta' = \frac{\cos\theta - \beta}{1 - \beta\cos\theta} = \frac{1 - \eta\gamma^2}{\beta\gamma^2\eta}, \qquad \sin\theta' = \frac{\sin\theta}{\gamma\eta},$$

the cross-sections (7) can be expressed via the quantities of the laboratory frame, substituted in (5) and differentiated with respect to γ. Using the transformation $d\sigma/d\Omega_1 = \left(d\sigma/d\Omega_1'\right)/\gamma^2\eta_1^2$, one can see that the cross-section expansion terms $\propto \omega'^2/\omega_G^2$ make the contribution $\propto \omega^2\eta^2/\left(\omega_G^2\eta_1^4\right)$ in $d\sigma/d\Omega_1$, which does not depend on γ explicitly, whereas the implicit dependence via $\eta(\beta)$ and $\eta_1(\beta)$ is very weak: $d\beta/d\gamma = 1/(\beta\gamma^3) \ll 1/\gamma$. The next terms of the cross-section expansion, $\propto \omega'^4/\omega_G^4 \ll \omega'^2/\omega_G^2$, introduce the explicit dependence on γ into $d\sigma/d\Omega_1$, $\propto \omega^4\eta^4\gamma^2/\left(\omega_G^4\eta_1^6\right)$, and their derivatives with respect to γ may be significant. Thus, the derivatives of the second and the first terms of the cross-section expansions in the kinetic equation (5) differ by the factor $\gamma^2\omega'^2/\omega_G^2$ (without taking account of the geometrical factors). This quantity may be both less and greater than unity, therefore in general it is necessary to retain both expansion terms in the cross-sections. Note that the third expansion term, $\propto \omega'^6/\omega_G^6$, (as well as all the next following ones) shows the explicit dependence on γ; its contribution to the kinetic equation differs from that of the second term by the factor $\omega'^2/\omega_G^2 \ll 1$ and it can be neglected.

In total, we obtain the following kinetic equations for the case of scattering in a moderately strong magnetic field:

$$\begin{aligned}
\frac{\partial n}{\partial r}(A \to A) &= \frac{\hbar n r_e^2}{mc}\left(I_1^{AA} + I_2^{AA} + I_3^{AA} + I_4^{AA}\right),\\
\frac{\partial n}{\partial r}(A \to B) &= \frac{\hbar n r_e^2}{mc}\left(I_1^{AB} + I_2^{AB}\right),\\
\frac{\partial n}{\partial r}(B \to A) &= \frac{\hbar n r_e^2}{mc}\left(I_1^{BA} + I_2^{BA}\right),\\
\frac{\partial n}{\partial r}(B \to B) &= \frac{\hbar n r_e^2}{mc}\left(I_1^{BB} + I_2^{BB}\right),
\end{aligned} \tag{8}$$

where $i \to j$ denotes the scattering from the state with i-polarization into the state with j-polarization, with $i, j = A, B$;

$$I_1^{AA} = \int d\gamma F \int \frac{\sin^2\theta \sin^2\theta_1}{\gamma^6\eta^3\eta_1^3}\left\{\frac{(\eta - \eta_1)^2}{\beta^2\gamma^3\eta_1^2}\frac{\partial n_1 k_1^2}{\partial k_1} + \right.$$

$$\left. + \frac{6(\eta_1 - \eta)n_1 k\eta^2}{\beta^2\gamma\eta_1^2}\left[1 - \frac{\eta + \eta_1}{2\gamma^2\eta\eta_1}\right]\right\} d\Omega_1;$$

$$I_2^{AA} = \int d\gamma F \int \frac{\omega^2}{\omega_G^2}\sin^2\Delta\phi\left\{\frac{(\eta - \eta_1)^2}{\beta^2\gamma^3\eta_1^2 k}\frac{\partial n_1 k_1^3}{\partial k_1}\frac{\left(1 - \eta\gamma^2\right)^2}{\beta^2\gamma^4\eta^2}\times\right.$$

$$\times\frac{\left(1 - \eta_1\gamma^2\right)^2}{\beta^2\gamma^4\eta_1^2} + \frac{2(\eta - \eta_1)kn_1\eta^3}{\beta^6\gamma^{11}\eta_1^3}\times$$

$$\times\left[\frac{\left(\eta\gamma^2 - 1\right)\left(\eta\gamma^2(2 - \eta) - 1\right)}{\eta^3}\frac{\left(1 - \eta_1\gamma^2\right)^2}{\eta_1^2} + \right.$$

$$\left.\left. + \frac{\left(\eta_1\gamma^2 - 1\right)\left(\eta_1\gamma^2(2 - \eta_1) - 1\right)}{\eta_1^3}\frac{\left(1 - \eta\gamma^2\right)^2}{\eta^2}\right]\right\} d\Omega_1;$$

$$I_3^{AA} = -\int d\gamma F \int \frac{\omega^2}{\omega_G^2}\frac{\sin 2\theta \sin 2\theta_1 \cos\Delta\phi}{\mu\mu_1\beta^2\gamma^3}\times$$

$$\times\left\{\frac{(\eta - \eta_1)^2}{\gamma^2\eta_1^2 k}\frac{\partial n_1 k_1^3}{\partial k_1} - \frac{(\eta - \eta_1)kn_1\eta^3}{\eta_1^3}\left[1 - \frac{\mu + \mu_1}{2\gamma^2\mu\mu_1}\right]\right\} d\Omega_1;$$

$$I_4^{AA} = \int d\gamma F \int \frac{\omega^4}{\omega_G^4}\frac{(\eta - \eta_1)n_1 k\eta^4\left(\eta\gamma^2 - 1\right)}{\eta_1^3\beta^2\gamma}\times$$

$$\times\left[2(1 + \sin^2\Delta\phi)\frac{\left(1 - \eta\gamma^2\right)^2}{\beta^2\gamma^4\eta^2}\times\right.$$

$$\left.\times\frac{\left(1 - \eta_1\gamma^2\right)^2}{\beta^2\gamma^4\eta_1^2} - \sin 2\theta \sin 2\theta_1 \cos\Delta\phi\right] d\Omega_1;$$

$$I_1^{AB} = \int d\gamma F \int \frac{\omega^2}{\omega_G^2} \cos^2 \Delta\phi \times$$

$$\times \left\{ \frac{(\eta - \eta_1)^2}{\beta^2 \gamma^3 \eta_1^2 k} \frac{\partial n_1 k_1^3}{\partial k_1} \frac{\left(1 - \eta\gamma^2\right)^2}{\beta^2 \gamma^4 \eta^2} + \right.$$

$$\left. + \frac{2(\eta - \eta_1) k n_1 \eta^3}{\eta_1^3} \frac{\eta\gamma^2 - 1}{\beta^4 \gamma^7 \eta^3} \left[\eta\gamma^2 (2 - \eta) - 1 \right] \right\} d\Omega_1;$$

$$I_2^{AB} = 2 \int d\gamma F \int \frac{\omega^4}{\omega_G^4} \left(1 + \cos^2 \Delta\phi\right) \times$$

$$\times \frac{\left(1 - \eta\gamma^2\right)^2}{\beta^2 \gamma^4 \eta^2} \frac{(\eta - \eta_1) n_1 k \eta^4 \left(\eta\gamma^2 - 1\right)}{\eta_1^3 \beta^2 \gamma} d\Omega_1;$$

$$I_1^{BA} = \int d\gamma F \int \frac{\omega^2}{\omega_G^2} \cos^2 \Delta\phi \times$$

$$\times \left\{ \frac{(\eta - \eta_1)^2}{\beta^2 \gamma^3 \eta_1^2 k} \frac{\partial n_1 k_1^3}{\partial k_1} \frac{\left(1 - \eta_1\gamma^2\right)^2}{\beta^2 \gamma^4 \eta_1^2} + \right.$$

$$\left. + \frac{2(\eta - \eta_1) k n_1 \eta^3}{\eta_1^3} \frac{\eta_1\gamma^2 - 1}{\beta^4 \gamma^7 \eta_1^3} \left[\eta_1\gamma^2 (2 - \eta_1) - 1 \right] \right\} d\Omega_1;$$

$$I_2^{BA} = 2 \int d\gamma F \int \frac{\omega^4}{\omega_G^4} \left(1 + \cos^2 \Delta\phi\right) \times$$

$$\times \frac{\left(1 - \eta_1\gamma^2\right)^2}{\beta^2 \gamma^4 \eta_1^2} \frac{(\eta - \eta_1) n_1 k \eta^4 \left(\eta\gamma^2 - 1\right)}{\eta_1^3 \beta^2 \gamma} d\Omega_1;$$

$$I_1^{BB} = \int d\gamma F \int \frac{\omega^2}{\omega_G^2} \sin^2 \Delta\phi \frac{(\eta - \eta_1)^2}{\beta^2 \gamma^3 \eta_1^2 k} \frac{\partial n_1 k_1^3}{\partial k_1} d\Omega_1;$$

$$I_2^{BB} = 2 \int d\gamma F \int \frac{\omega^4}{\omega_G^4} \left(1 + \sin^2 \Delta\phi\right) \times$$

$$\times \frac{(\eta - \eta_1) n_1 k \eta^4 \left(\eta\gamma^2 - 1\right)}{\eta_1^3 \beta^2 \gamma} d\Omega_1$$

(9)

$\mu \equiv 1 - \beta \cos 2\theta$ and $\mu_1 = 1 - \beta \cos 2\theta_1$.

Let us start the analysis of the kinetic equations from the case $B \to B$. The first term of the equation, I_1^{BB}, describes the monotonic shift of the photon distribution toward lower frequencies. The analogous evolution of the photon spectrum is characteristic of scattering in the absence of the magnetic field as well. The second term, I_2^{BB}, does not have an analogue in the non-magnetic case and is responsible for the photon redistribution between the states satisfying the condition $\omega\eta = \omega_1\eta_1$. Its sign is determined by the sign of the factor $(\eta - \eta_1)$, so that the occupation numbers decrease on account of scattering into the states with $\theta_1 > \theta$ and increase due to the photons coming from the states with $\theta_1 < \theta$. One can find that $I_2^{BB} / I_1^{BB} \approx \left(\omega^2\gamma^2\eta^2 / \omega_G^2\right)\chi^2\gamma^2$, where $\chi \equiv \min(\theta, \theta_1)$. As a rule, in the pulsar magnetosphere the angle of incidence of radiation satisfies the condition $1/\gamma \ll \theta < 1$, so that in the case of a moderately strong magnetic field I_2^{BB} makes the dominant contribution to the evolution of the occupation numbers. Note that $\left(I_2^{AB} / I_1^{AB}, I_2^{AB} / I_1^{AB}\right) > 1$ at the same condition.

The kinetic equation for the case $A \to A$ has a more intricate form. The term I_1^{AA} does not tend to zero at $\omega_G \to \infty$ and describes the longitudinal scattering (for a detailed investigation of this case see [21]). According to the estimates, $\left(I_2^{AA} / I_1^{AA}, I_3^{AA} / I_1^{AA}\right) \approx \chi^2\gamma^2\left(\omega^2\gamma^2\eta^2 / \omega_G^2\right)$ and $I_4^{AA} / I_1^{AA} \approx \chi^4\gamma^4\left(\omega^4\gamma^4\eta^4 / \omega_G^4\right)$. Thus, in a moderately strong field I_4^{AA} dominates and, similarly to the terms $I_2^{BB,AB,BA}$, describes the transverse scattering. Then the photons are transferred to the states with $\theta_1 > \theta$. It will be noted that in the regime of longitudinal scattering the photons are, on the contrary, transferred into the states with $\theta_1 < \theta$ (cf. the signs of I_4^{AA} and the second term in I_1^{AA}).

5. INDUCED TRANSVERSE SCATTERING OUT OF A NARROW BEAM

In the case of transverse scattering one can retain only the last terms of the kinetic equations (8) and write them in the form

$$\frac{\partial n}{\partial r}(i \to j) = \int d\gamma F \int \tilde{a} g^{ij} d\Omega_1, \qquad (10)$$

where

$$\tilde{a} = r_e^2 n(k) n_1(k\eta/\eta_1) \frac{2\hbar k}{mc} \frac{\omega^4\gamma^4\eta^4}{\omega_G^4} \frac{\eta-\eta_1}{\eta_1^3} \frac{\eta\gamma^2-1}{\beta^2\gamma^5}, \quad (11)$$

i, j denote the photon polarization in the initial and final states and

$$g^{AA} = \left(1+\sin^2\Delta\phi\right)\frac{\left(1-\eta\gamma^2\right)^2}{\beta^2\gamma^4\eta^2}\frac{\left(1-\eta_1\gamma^2\right)^2}{\beta^2\gamma^4\eta_1^2} -$$
$$-\frac{\sin 2\theta \sin 2\theta_1 \cos\Delta\phi}{2},$$
$$g^{AB} = \left(1+\cos^2\Delta\phi\right)\frac{\left(1-\eta\gamma^2\right)^2}{\beta^2\gamma^4\eta^2}, \quad (12)$$
$$g^{BA} = \left(1+\cos^2\Delta\phi\right)\frac{\left(1-\eta_1\gamma^2\right)^2}{\beta^2\gamma^4\eta_1^2},$$
$$g^{BB} = \left(1+\sin^2\Delta\phi\right).$$

The kinetic equations (10) differ only by the factors g^{ij}, which are usually of order unity. Note also the symmetry of these factors with respect to the initial and final states.

Let us consider the transverse induced scattering as applied to the pulsar magnetosphere. The pulsar radio emission is characterized by a strong directivity forward. In each point of the pulsar emission cone the radiation concentrates in a narrow beam with an opening angle $\approx 1/\gamma$, whereas the width of the cone itself is much larger, $w \gg 1/\gamma$. In our problem, one can neglect the width of the beam and describe it by a single wavevector $\vec{k}$. Then the difference in orientations of the wavevectors of the beams forming the pulsar emission cone determines the finitude of the observed radio pulse width. Note also that the transverse size of the scattering region, which is determined by the width of the pulsar emission cone, is sufficiently large not to impose substantial restrictions on scattering efficiency.

The beam propagates at an angle $1/\gamma \ll \theta < 1$ to the magnetic field, and the photons are scattered out of the beam. In case of efficient scattering, the radiation groups close to the direction $\theta_1^{\max}$ corresponding to the maximum scattering probability. In contrast to the case of longitudinal scattering, where $\theta_1^{\max} \approx 1/\gamma$ [21], for the transverse scattering $\theta_1^{\max} \approx \pi$ (see Eq. (11)) and, correspondingly, $\omega_1 = \omega\eta/\eta_1 = \omega\theta^2/4 < \omega$. Following [21], let us proceed from the occupation numbers to the spectral intensities $I_{a,b} \equiv \int i_{a,b} d\Omega_{a,b}$, where $i_a \equiv \hbar\omega^3 n(\vec{k})/\left(2\pi^2c^2\right)$, and $i_b \equiv \hbar\omega_1^3 n_1(\vec{k}_1)/\left(2\pi^2c^2\right)$, and write the set of equations describing the intensity redistribution between the two states in the form

$$\frac{dI_a}{dr} = -a g^{ij} I_a I_b, \qquad \frac{dI_b}{dr} = a g^{ij} I_a I_b, \quad (13)$$

where

$$a = \frac{8 n_e r_e^2}{m\gamma^3\nu^2\theta^4}\frac{\nu'^4}{\nu_G^4}, \quad (14)$$

γ is the characteristic Lorentz-factor of the scattering particles distribution, $\nu = \omega/(2\pi)$, $\nu' = \nu\gamma\eta$, and $\nu_G = \omega_G/(2\pi)$. The set of the form (13) is solved and investigated in detail in [21]:

$$I_a = \frac{I\left[I_a^{(0)}/I_b^{(0)}\right]\exp(-Iag^{ij}r)}{1+\left[I_a^{(0)}/I_b^{(0)}\right]\exp(-Iag^{ij}r)},$$
$$I_b = \frac{I}{1+\left[I_a^{(0)}/I_b^{(0)}\right]\exp(-Iag^{ij}r)},$$

where $I \equiv I_a + I_b \equiv I_a^{(0)} + I_b^{(0)}$. The background intensity grows substantially on condition that $x \equiv \left(I_a^{(0)}/I_b^{(0)}\right)\exp(\Gamma^{ij}) \geq 1$, where $\Gamma^{ij} \equiv Iag^{ij}r$ is the scattering efficiency. In the pulsar magnetosphere this condition is typically satisfied at $\Gamma^{ij} = 20 \div 30$.

It is interesting to compare the efficiencies of scattering out of the beam in the longitudinal and transverse regimes. As can be found from equation (9), for a fixed value of θ_1 the ratio $I_4^{AA}/I_1^{AA} \approx \theta^2\theta_1^2\gamma^4\nu'^4/\nu_G^4$. However it should be kept in mind that in the two regimes the scattering probability peaks at substantially different values of θ_1. Comparing equation (14) with equation (4) from [21], we find the ratio of the scattering efficiencies

$$\frac{\Gamma_t}{\Gamma_l} = \frac{\gamma^2}{3}\frac{\nu'^4}{\nu_G^4}, \quad (15)$$

where the indices t and l refer to the transverse and longitudinal scattering, respectively. One can see that not too far from the resonance the transverse scattering is much more efficient than the longitudinal one, bear in mind, however, that at higher altitudes in the pulsar magnetosphere the number density of the scattering particles and the intensity of the incident radiation decrease. In pulsars, both processes can be sufficiently efficient (the numerical estimate of Γ_l is given by equation (9) in [21]). Though note that if the condition $\nu'^4\gamma^2/\left(3\nu_G^4\right)>1$ is already fulfilled in the emission region, the longitudinal scattering does not occur at all.

6. DISCUSSION

Our consideration has proved that the induced scattering of the pulsar radio emission out of the beam in a moderately strong magnetic field may lead to a substantial intensity growth in the direction antiparallel to the velocity of the scattering particles, $\theta_1^{\max}=\pi$. Thus, the scattered component is directed backward – to the neutron star, – similarly to the bi-directional model [20]. In the case of orthogonal rotator, when the pulsar magnetic axis is almost aligned with the rotation axis, the scattered component should appear on the profile as an interpulse. Just as in the model [20], the region of the intepulse formation lies in the outer magnetosphere, but now its location is strictly specified: the transverse scattering takes place at the altitudes of order of the cyclotron resonance radius and, certainly, only in a small part of the open field line tube traversed by the pulsar radio beam.

Although the main pulse and interpulse originate at different altitudes in the magnetosphere, within the framework of our theory these components are physically connected, since the interpulse emission is the scattered emission of the main pulse. Consequently, one can expect that the intensity modulation of the main pulse is preserved in the interpulse. Recent observations of the subpulses in the pulsar B1702-19 [9] show indeed that the subpulse structure of the interpulse is modulated with the same periodicity as does the structure of the main pulse, with the corresponding shift by half of the pulsar period. Thus, our mechanism of the interpulse formation has the observational support.

In accordance with the numerical estimates (see equation (15) above and equation (9) in [21]), the shorter the pulsar period, the higher the radio luminosity and the lower the frequency, the more efficient is scattering. All these trends are confirmed by observations. Until the growth of the scattered component reaches the stage of saturation, the intensity dependence on scattering efficiency is tremendous, so that the interpulse should rapidly grow with the frequency decrease and can suddenly appear on the pulse profile. Some pulsars really show interpulses only in the decameter range [3-5].

In those cases when the interpulse is observed over a wide frequency range, the growth of the scattered component should approach the stage of saturation. Then the intensity changes with frequency not so dramatically, however the spectrum of the interpulse should still be somewhat steeper than the main pulse spectrum, which is in line with the observations. Note also that at the saturation stage the scattering should markedly change the main pulse intensity as well, especially at lower frequencies, so that the main pulse spectrum flattens.

It will be noted that the emission comes to the interpulse from the higher frequencies, $\nu_1\approx\nu\theta^2/4<\nu$. With the decreasing spectrum of the pulsar this implies that the interpulse intensity should be much less than the original intensity of the main pulse at the same frequency. The intensities of the two profile components may become comparable only if the main pulse is substantially suppressed by scattering.

The position angle of linear polarization of the scattered radiation is determined by the orientation of the $\vec{k}_1\times\vec{b}$ -plane in the scattering region and in general differs from the position angle of the main pulse, which is determined by the orientation of the $\vec{k}\times\vec{b}$ -plane in the emission region (here $\vec{b}$ is the unit vector along the magnetic field). In the outer magnetosphere, the radio beam occupies only a small part of the open field line tube, and, consequently, in the scattering region the magnetic field is almost homogeneous. Correspondingly, the position angle should be almost constant across the whole interpulse, which is in line with observations. Although both orthogonal polarization modes can grow due to scattering, the scattering efficiency may differ substantially, so that one of the modes will dominate and lead to high polarization of the interpulse emission.

7. CONCLUSIONS

The induced scattering of a narrow beam into the background off the particles of the magnetized ultrarelativistic electron-positron plasma of a pulsar is considered. The presence of an external magnetic field affects the scattering process on condition that $\omega'\ll\omega_G$, and

in this case the character of scattering can be different. In the superstrong magnetic field, $\omega'^4/\omega_G^4 \ll 1/\gamma^2$, the longitudinal scattering holds: the beam photons are scattered predominantly into the state with $\theta_1^{max} \approx 1/\gamma$ and $\omega_1 \approx \omega\theta^2\gamma^2 \gg \omega$, i.e. the scattered component is almost aligned with the external magnetic field. In a moderately strong field, $1/\gamma^2 \ll \omega'^4/\omega_G^4 \ll 1$, the transverse scattering takes place, with the photons being scattered chiefly backward, antiparallel to the velocity of the scattering particles, so that $\theta_1^{max} \approx \pi$ and $\omega_1 \approx \omega\theta^2/4 < \omega$. As the magnetic field strength decreases with distance from the neutron star, both scattering regimes are typically realized in the open field line tube. Then two scattered components may form, which are identified with the precursor and the interpulse of the pulsar, respectively.

In this paper, the kinetic equations for the case of transverse induced scattering are first derived and the formation of the interpulse component is considered. In the framework of the suggested physical model of the interpulse the spectral and polarization properties of this component as well as its connection to the main pulse are explained.

REFERENCES

1. Manchester, R. N., Lyne, A. G., Pulsar interpulses – two poles or one?, *Mon. Notic. Roy. Astron. Soc.*, 181:761-767, 1977.
2. Kramer, M., Xilouris, K. M., Lorimer, D. R., Doroshenko, O., Jessner, A., Wielebinski, R., Wolszczan, A., Camilo, F., The characteristics of millisecond pulsar emission. I. Spectra, pulse shapes, and the beaming fraction, *Astrophys. J.*, 501(1):270-285, 1998.
3. Bruck, Yu. M., Ustimenko, B. Yu., Some features of the pulsed radiation from the pulsar 1919+21 at 16.7, 20 and 25 MHz, *Astrophys. and Space Sci.*, 49:349-366, 1977.
4. Bruck, Yu. M., Ustimenko, B. Yu., The interpulse emission structure in pulsars, *Astron. and Astrophys.*, 80:170-173, 1979.
5. Bruck, Yu. M., Decametric emission by pulsars, *Aust. J. Phys.*, 40:861-870, 1987.
6. Rankin, J. M., Rathnasree, N., On the polarization and emission geometry of pulsar 1929+10: Does its emission come from a single pole or two poles?, *J. Astrophys. Astron.*, 18:91-131, 1997.
7. Hankins, T. H., Boriakoff, V., Microstructure in the pulsar 0950+08 interpulse at radio wavelengths, *Astrophys. J.*, 249(1):238-240, 1981.
8. Hankins, T. H., Cordes, J. M., Interpulse emission from pulsar 0950+08: How many poles?, *Astrophys. J.*, 249(1):241-253, 1981.
9. Weltevrede, P., Wright, G. A. E., Stappers, B. W., The main pulse-interpulse interaction in PSR B1702-19, *Astron. and Astrophys.*, 467:1163-1174, 2007.
10. Biggs, J. D., Main pulse/interpulse correlation and mode changing in PSR 1055-52, *Mon. Notic. Roy. Astron. Soc.*, 246:341-348, 1990.
11. Fowler, L. A., Wright, G. A. E., Morris, D., Unusual properties of the pulsar PSR 1822-09, *Astron. and Astrophys.*, 93(1):54-61, 1981.
12. Fowler, L. A., Wright, G. A. E., Pulse-interpulse interaction in pulsar PSR 1822-09, *Astron. and Astrophys.*, 109(2):279-281, 1982.
13. Gil, J. A., Jessner, A., Kijak, J., Kramer, M., Malofeev, V., Malov, I., Seiradakis, J. H., Sieber, W., Wielebinski, R., Multifrequency study of PSR 1822-09, *Astron. and Astrophys.*, 282(1):45-53, 1994.
14. Cognard, I., Shrauner, J. A., Taylor, J. H., Thorsett, S. E., Giant radio pulses from a millisecond pulsar, *Astrophys. J.*, 457:L81-L84, 1996.
15. Kinkhabwala, A., Thorsett, S. E., Multifrequency observations of giant radio pulses from the millisecond pulsar B1937+21, *Astrophys. J.*, 535(1):365-372, 2000.
16. Cordes, J. M., Bhat, N. D. R., Hankins, T. H., McLaughlin, M. A., Kern, J., The brightest pulses in the Universe: Multifrequency observations of the Crab pulsar's giant pulses, *Astrophys. J.*, 612(1):375-388, 2004.
17. Hankins, T. H., Eilek, J. A., Radio emission signatures in the Crab pulsar, *Astrophys. J.*, 670(1):693-701, 2007.
18. Manchester, R. N., Observations of pulsar polarization at 410 and 1665 MHz, *Astrophys. J. Suppl. Ser.*, 23:283-322, 1971.
19. Gil, J., Interpulse beams and profile components, *Astrophys. J.*, 299(1):154-160, 1985.
20. Dyks, J., Zhang, B., Gil, J., Reversals of radio emission direction in PSR B1822-09, *Astrophys. J.*, 626(1):L45-L47, 2005.
21. Petrova, S. A., The mechanism of component formation out of the main pulse of a radio pulsar. I. The precursor, *Radiofizika i Radioastronomia*, 13(1):5-14, 2008 (in Russian).
22. Blandford, R. D., Scharlemann, E. T., On the scattering and absorption of electromagnetic radiation within pulsar magnetospheres, *Mon. Notic. Roy. Astron. Soc.*, 174(1):59-85,1976.
23. Ochelkov, Yu. P., Usov, V. V., Compton scattering of electromagnetic radiation in pulsar magnetospheres, *Astrophys. and Space Sci.*, 96(1):55-81, 1983.
24. Lyubarskii, Yu. E., Petrova, S. A., Stimulated scattering of radio emission in pulsar magnetospheres, *Astron. Letters.*, 22(3):399-408, 1996.
25. Petrova, S. A., Toward explanation of microstructure in pulsar radio emission, *Astron. and Astrophys.*, 417:L29-L32, 2004.
26. Petrova, S. A., On the origin of giant pulses in radio pulsars, *Astron. and Astrophys.*, 424:227-236, 2004.
27. Canuto, V., Lodenquai, J., Ruderman, M., Thomson scattering in a strong magnetic field, *Phys. Rev. D.*, 3:2303-2308, 1971.

Radio Physics and Radio Astronomy, 1(1), 37–47 (2010)

NEAR-FIELD SCATTERING OF WAVES FROM A STATISTICALLY ROUGH SURFACE: I. FIELD FLUCTUATIONS

A. S. Bryukhovetski

A. Usikov Institute of Radio Physics and Electronics, National Academy of Sciences of Ukraine, 12, Academician Proskura St., Kharkiv 61085, Ukraine

*Address all correspondence to A. S. Bryukhovetski E-mail:ire@ire.kharkov.ua

An expression has been derived for the fluctuating field component scattered by a statistically rough surface. The expression represents the leading term of a series expansion with respect to a large parameter which determines the wave zone relative to the source and observation point positions.

The asymptotic representation is uniform with respect to the altitudes of these points above the surface and can be used as a basis for determining power characteristics of the fluctuating field in the near zone relative to the surface.

KEY WORDS: *scattering, fluctuations, asymptotic representation, rough surface, spectrum*

1. INTRODUCTION

Wave scattering by small random irregularities of interfaces have been theoretically investigated for more than fifty years. Nevertheless there are only few results on investigating near-field scattering which do not offer sufficient generality. Many papers on radar investigations of the disturbed sea surface involve the specific scattering cross-section obtained by Barrick [1] for a small scattering area within which the wave front curvature of the spherical wave can be neglected. Inadequacy of such a model for areas illuminated by the radar antenna pattern is quite evident. The reason is that the Fresnel parameter corresponding to the far-field zone of the antenna aperture is $\left(ka^2/R\right) \ll 1$, where a is the antenna aperture size; $k = 2\pi/\lambda$, with λ being the wavelength; and R is the range. Since the angular size of the antenna pattern is $\sim \lambda/a$, the transverse dimension of the illuminated area can be estimated as $L \sim R\lambda/a$. Therefore the respective Fresnel parameter for the scattering area is $\left(kL^2/R\right) \sim 4\pi^2 \left(ka^2/R\right)^{-1} \gg 1$, which means that the wave front curvature across the area should be taken into account.

The scattering model suggested by Bass and Fuks (see [2], § 10) seems to be deficient for the following reasons. First, the calculations have been performed for the soft and rigid surfaces. Second, the applicability of the calculation results to describing wave scattering by real surfaces still remains questionable. And third, the writers themselves cast doubt on that the introduction of the "spectrum separation range" (see footnote on page 107) is valid for aperiodic surfaces.

Thus investigation of near-field scattering by rough surfaces still remains a topical problem of great importance for practice.

2. INTEGRAL REPRESENTATION OF THE FLUCTUATING FIELD COMPONENT

Let us obtain a representation for the scattered field which would have no rigid limitations on the source and observation point altitudes and the scattering area

ISSN 2152-274X

size, and hence on the Fresnel parameter magnitude. In a particular case of scattering from an infinite surface $(L \to \infty)$ this parameter assumes infinite value for any observation point located at a finite range $(R < \infty)$ from the surface.

As we mentioned earlier [3], the perturbation method of the theory of wave scattering by random surface irregularities implies in fact three versions of the perturbation method which differ by the ranges of applicability. The most general of these seems to be the Kreichnan approximation [4] according to which the scattered (fluctuating) field $u\left(\vec{R}_2\right)$ at a time moment t (the time dependent factor $\exp(-i\omega_0 t)$ has been omitted) can be expressed as

$$u\left(\vec{R}_2\right) = -\frac{i}{4\pi^2}\iint_S \mathrm{d}^2\vec{r}_1 \iint \mathrm{d}^2\vec{k}_{2\perp} \frac{1}{k_{2z} + k\eta(\vec{k}_{2\perp})} \times$$

$$\times \exp\left(i\left[\vec{k}_{2\perp}\left(\vec{r}_2 - \vec{r}_1\right) + k_{2z}\left(z_2 - z_1\right)\right]\right) L_1\left(\varsigma_1 \langle U_1 \rangle\right)\Big|_{z_1=0}. \quad (1)$$

Here

$$L_1\left(\varsigma_1 \langle U_1 \rangle\right)\Big|_{z_1=0} =$$

$$= \left\{\nabla_1 \varsigma_1 \cdot \nabla_1 - \varsigma_1\left(\frac{\partial}{\partial z_1} + ik\eta_0\right)\right\}\langle U_1 \rangle\Big|_{z_1=0}; \quad (2)$$

$\langle U_1 \rangle = \left\langle U\left(\vec{R}_1\right)\right\rangle$ is the average field at the point $\vec{R}_1 = (\vec{r}_1, z_1)$; $\nabla_1 = \vec{i}_x \frac{\partial}{\partial x_1} + \vec{i}_y \frac{\partial}{\partial y_1}$ is the gradient with respect to the variables x_1 and y_1 within the mean plane S (see Fig. 1); $z = \varsigma_1 = \varsigma(\vec{r}_1)$ are random irregularities of the scattering surface with the mean value $\langle z \rangle = \langle z_1 \rangle = 0$ forming the plane S; $\eta_0 = \text{const}$ is the impedance of the unperturbed (smooth) surface; and $\eta\left(\vec{k}_{2\perp}\right)$ is the effective impedance which corresponds to the average field and can be found through solving the integral equation [4]

$$\eta\left(\vec{k}_{2\perp}\right) = \eta_0 + \frac{\sigma^2}{k}\iint_{-\infty}^{\infty} \mathrm{d}^2\vec{\chi} \frac{\tilde{W}\left(\vec{k}_{2\perp} - \vec{\chi}\right)}{\chi_z + k\eta(\vec{\chi})} \times$$

$$\times\left[k^2 - \vec{\chi}\vec{k}_{2\perp} - k^2\eta_0\eta\left(\vec{k}_{2\perp}\right)\right]\left[k^2 - \vec{\chi}\vec{k}_{2\perp} + k\eta_0\chi_z\right]. \quad (3)$$

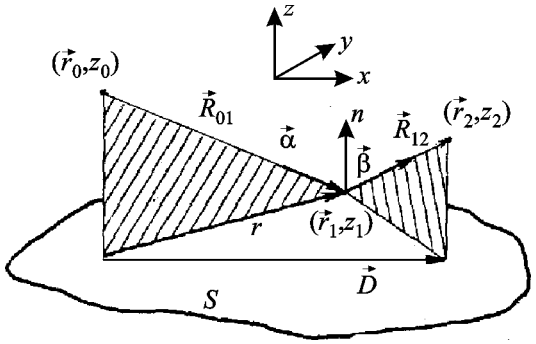

FIG. 1: Scattering geometry

The exponential terms in Eq. (1) with different components $\vec{k}_{2\perp}$ within the plane $z = 0$ correspond to a set of homogeneous $\left(\left|\vec{k}_{2\perp}\right| \le k\right)$ and inhomogeneous $\left(\left|\vec{k}_{2\perp}\right| > k\right)$ plane waves with wave vector projections on the *oz*-axis equal to $k_z = \sqrt{k^2 - k_{2\perp}^2}$, with $\mathrm{Im}\, k_z \ge 0$. Here $k = \omega_0/c$ is the wavenumber, with ω_0 and c being, respectively, the frequency and phase velocity of the wave.

Application of the iteration method to Eq. (3), with $\eta(\vec{\chi}) = \eta\left(\vec{k}_{2\perp}\right) = \eta_0$ having been used in the right-hand part as a zeroth-order approximation, yields an expression possessing the symmetric property

$$\eta\left(-\vec{k}_{2\perp}\right) = \eta\left(\vec{k}_{2\perp}\right), \quad (4)$$

which follows from the symmetric property $W(-\vec{K}) = W(\vec{K})$ for the real field of random irregularities [4].

According to paper [4], the average field at the point $\vec{R}_0 = (\vec{r}_0, z_0)$ above the rough surface produced by a point-size source located at the point $\vec{R}_1 = (\vec{r}_1, z_1)$ is

$$\langle U_1 \rangle \equiv \left\langle U\left(\vec{R}_1\right)\right\rangle = \frac{i}{2\pi}\iint_{-\infty}^{\infty} \mathrm{d}^2\vec{k}_\perp \frac{1}{k_z} \exp\left[i\vec{k}_\perp\left(\vec{r}_1 - \vec{r}_0\right)\right] \times$$

$$\times\left\{\exp\left[ik_z\left(z_1 - z_0\right)\right] + V\left(\vec{k}_\perp\right)\exp\left[ik_z\left(z_1 + z_0\right)\right]\right\}. \quad (5)$$

Here $k_z = \sqrt{k^2 - k_\perp^2}$, with $\mathrm{Im}\, k_z \ge 0$, and the reflection factors of plane waves from a plane surface with the effective impedance $\eta\left(\vec{k}_\perp\right)$,

$$V\left(\vec{k}_\perp\right)=\frac{k_z-k\eta\left(\vec{k}_\perp\right)}{k_z+k\eta\left(\vec{k}_\perp\right)}, \tag{6}$$

are determined by the relations as follows

$$1+V\left(\vec{k}_\perp\right)=\frac{2k_z}{k_z+k\eta\left(\vec{k}_\perp\right)} \tag{7}$$

and

$$1-V\left(\vec{k}_\perp\right)=\frac{2k\eta\left(\vec{k}_\perp\right)}{k_z+k\eta\left(\vec{k}_\perp\right)}. \tag{8}$$

With account of Eqs. (7) and (8), the expressions Eqs. (1) and (5) can be brought, after rather simple mathematics, to the form

$$u\left(\vec{R}_2\right)=-\frac{1}{4\pi^2}\iint_S \mathrm{d}^2\vec{r}_1 I_{12}L_1\left(\varsigma_1\left\langle U_1\right\rangle\right)\Big|_{z_1=0}, \tag{9}$$

$$\left\langle U_1\right\rangle\equiv I_{01}=\frac{\exp(ikR_{01})}{R_{01}}+\frac{\exp(ikR'_{01})}{R'_{01}}+I'_{01}, \tag{10}$$

with

$$I_{12}=\frac{\exp(ikR_{12})}{R_{12}}+\frac{\exp(ikR'_{12})}{R'_{12}}+I'_{12}. \tag{11}$$

In the derivations we have used the Weyl expansion (see [5], page 215) in plane inhomogeneous waves, viz.

$$\frac{\exp(ikR)}{R}=\frac{i}{2\pi}\int\int_{-\infty}^{\infty}\mathrm{d}^2\vec{k}_\perp\frac{1}{k_z}\exp\left[i(\vec{k}_\perp\vec{r}+k_z z)\right], \tag{12}$$

with $\vec{R}=(\vec{r},z)$, $z\geq 0$ and $\operatorname{Im}k_z\geq 0$,

and have introduced the notation $\vec{R}_{01}=\vec{R}_1-\vec{R}_0$, $\vec{R}_{12}=\vec{R}_2-\vec{R}_1$, $\vec{R}'_{01}=\vec{R}_1-\vec{R}'_0$, and $\vec{R}'_{12}=\vec{R}_2-\vec{R}'_1$, with $\vec{R}'_0=(\vec{r}_0,-z_0)$ and $\vec{R}'_1=(\vec{r}_1,-z_1)$ being radius vectors of the mirror reflections of the source and the scattering point within the plane $z=0$.

The expressions for the values I'_{01} and I'_{12} are as follows

$$I'_{01}=\frac{i}{2\pi}\int\int_{-\infty}^{\infty}\mathrm{d}^2\vec{k}_\perp\frac{1}{k_z}\left[V\left(\vec{k}_\perp\right)-1\right]\times$$
$$\times\exp\left(i\left[\vec{k}_\perp(\vec{r}_1-\vec{r}_0)+k_z(z_1+z_0)\right]\right) \tag{13}$$

and

$$I'_{12}=\frac{i}{2\pi}\int\int_{-\infty}^{\infty}\mathrm{d}^2\vec{k}_{2\perp}\frac{1}{k_{2z}}\left[V\left(\vec{k}_{2\perp}\right)-1\right]\times$$
$$\times\exp\left(i\left[\vec{k}_{2\perp}(\vec{r}_2-\vec{r}_1)+k_{2z}(z_2+z_1)\right]\right). \tag{14}$$

Here it has been allowed for that the condition $z_1\to 0$ results in $R'_{12}\to R_{12}$.

Thus to determine the scattered Eq. (9) and average Eq. (10) fields it is necessary to calculate the values given by Eqs. (13) and (14).

3. ASYMPTOTIC REPRESENTATIONS FOR I'_{01} AND I'_{12} IN THE WAVE ZONE ($kR'_{01}, kR'_{12}\gg 1$)

Let us introduce a spherical coordinate frame with the equatorial plane coincident with the plane $z=0$, i.e. with the surface *S*, and the polar axis pointed along the *oz*-axis. Then we can write

$$\vec{R}_{01}=\left(R_{01}\sin\theta_{01}\cos\varphi_{01}, R_{01}\sin\theta_{01}\sin\varphi_{01}, R_{01}\cos\theta_{01}\right). \tag{15}$$

Accordingly, the spherical coordinates for the vector $\vec{R}_{12}$ are R_{12}, θ_{12} and φ_{12}. The respective coordinates for the vectors $\vec{R}'_{01}$ and $\vec{R}'_{12}$ will be primed. The wave vector can be expressed as

$$\vec{k}=\vec{k}_\perp+\vec{i}_z k_z=\left(k\sin\theta\cos\varphi, k\sin\theta\sin\varphi, k\cos\theta\right). \tag{16}$$

The spherical coordinates for the vector $\vec{k}_2=\vec{k}_{2\perp}+\vec{i}_z k_{2z}$ are k, θ_2 and φ_2, with the ranges of variability as follows

$$0 \le \varphi, \varphi_2 \le 2\pi; \qquad 0 \le \theta, \theta_2 \le \frac{\pi}{2}; \tag{17}$$

and $\frac{\pi}{2} - i \cdot \infty \le \theta, \theta_2 \le \frac{\pi}{2}$.

The angles θ and θ_2 assume complex-valued magnitudes along a broken line given by the inequalities Eq. (17).

Then, the expressions Eqs. (13) and (14) take the form (see [5], page 216; and [6-8])

$$I'_{01} = \frac{ik}{2\pi}\int_0^{\frac{\pi}{2}-i\infty} d\theta \sin\theta \int_0^{2\pi} d\varphi \left[V(\theta,\varphi)-1\right]\times$$
$$\times \exp\left[ikr'_{01}\sin\theta\cos(\varphi-\varphi'_{01})\right]\exp\left(ikR'_{01}\cos\theta\cos\theta'_{01}\right), \tag{18}$$

$$I'_{12} = \frac{ik}{2\pi}\int_0^{\frac{\pi}{2}-i\infty} d\theta_2 \sin\theta_2 \int_0^{2\pi} d\varphi_2 \left[V(\theta_2,\varphi_2)-1\right]\times$$
$$\times \exp\left[ikr'_{12}\sin\theta_2\cos(\varphi_2-\varphi'_{12})\right]\exp\left(ikR'_{12}\cos\theta_2\cos\theta'_{12}\right). \tag{19}$$

Here $r'_{01} = R'_{01}\sin\theta'_{01}$ and $r'_{12} = R'_{12}\sin\theta'_{12}$, and the values $V(\theta,\varphi)$ and $V(\theta_2,\varphi_2)$ have been obtained through going over in the expressions for $V\left(\vec{k}_\perp\right)$ and $V\left(\vec{k}_{2\perp}\right)$ to the spherical coordinates of the vectors $\vec{k}_\perp$ and $\vec{k}_{2\perp}$.

Let us denote

$$f_V(\theta,\varphi) \equiv V(\theta,\varphi) - 1 = \frac{-2\eta(\theta,\varphi)}{\cos\theta + \eta(\theta,\varphi)}. \tag{20}$$

The symmetry of the relation Eq. (4) implies the symmetry of $f_V(\theta,\varphi)$ with respect to the changes $\theta \to -\theta$ or $\varphi \to \varphi \pm \pi$ (the changes result in $\vec{k}_\perp \to -\vec{k}_\perp$), viz.

$$f_V(-\theta,\varphi) = f_V(\theta,\varphi\pm\pi) = f_V(\theta,\varphi). \tag{21}$$

To integrate the expression Eq. (18) over φ, we will use the expansion (see [9], page 987)

$$\exp\left[ip\cos(\varphi-\varphi'_{01})\right] = \sum_{m=-\infty}^{\infty} i^m J_m(p)\exp\left[im(\varphi-\varphi'_{01})\right] =$$
$$= \sum i^m J_m(p)\exp\left[-im(\varphi-\varphi'_{01})\right], \tag{22}$$

where $p = kr'_{01}\sin\theta$, and the relations as follows (see [10], pages 180 and 183)

$$J_{2m}(p) = \frac{1}{2}\left[H^{(1)}_{2m}(p) + H^{(2)}_{2m}(p)\right] \tag{23}$$

and

$$H^{(2)}_{2m}\left(p\exp(-i\pi)\right) = -\exp(i2m\pi)H^{(1)}_{2m}(p). \tag{24}$$

The result is

$$I'_{01} = \frac{ik}{2}\sum_{m=-\infty}^{\infty}(-1)^m \exp(i2m\varphi'_{01})\left[\int_0^{\frac{\pi}{2}-i\infty} d\theta\sin\theta\times\right.$$
$$\times\exp\left(ikR'_{01}\cos\theta\cos\theta'_{01}\right)H^{(1)}_{2m}(p)C_{2m}(\theta) -$$
$$\left.-\int_0^{-\frac{\pi}{2}+i\infty} d\theta\sin\theta\exp\left(ikR'_{01}\cos\theta\cos\theta'_{01}\right)H^{(1)}_{2m}(p)C_{2m}(-\theta)\right], \tag{25}$$

where $C_{2m}(\theta) = \frac{1}{2\pi}\int_0^{2\pi}\exp(-i2m\varphi)f_V(\theta,\varphi)d\varphi$ are the expansion coefficients of $f_V(\theta,\varphi)$ in the Fourier series with respect to φ which allow for the symmetry of the transformation $\varphi \to \varphi \pm \pi$. As is usual for the wave zone $kR'_{01} \gg 1$ and for the saddle-point method [5, 6 and 8], we will confine the consideration to the first term in the asymptotic expansion

$$H^{(1)}_{2m}(p) \approx \sqrt{\frac{2}{\pi p}}(-1)^m \exp\left[i\left(p-\frac{\pi}{4}\right)\right]\left\{1 + i\frac{16m^2-1}{8p} + \ldots\right\}, \tag{26}$$

which is valid in the case of a weak dependence of $\eta(\theta,\varphi)$ on φ. Substitution of Eq. (26) into Eq. (25) yields

$$I'_{01} = \exp\left(i\frac{\pi}{4}\right)\sqrt{\frac{R}{2\pi r'_{01}}}\int_{-\frac{\pi}{2}+i\infty}^{\frac{\pi}{2}-i\infty} d\theta\sqrt{\sin\theta}\times$$
$$\times\left[V(\theta,\varphi'_{01})-1\right]\exp\left[ikR'_{01}\cos(\theta-\theta'_{01})\right]. \tag{27}$$

Here we have taken into account that $p = kr'_{01}\sin\theta$, where $r'_{01} = R'_{01}\sin\theta'_{01}$, and the Fourier expansion of $f_V(\theta,\varphi'_{01})$ is

$$f_V(\theta,\varphi'_{01}) = V(\theta,\varphi'_{01}) - 1 = \sum_{m=-\infty}^{\infty} C_{2m}(\theta)\exp(i2m\varphi'_{01}). \tag{28}$$

Thus integration over φ in the wave zone picks up in the expansion only those waves whose azimuthal direction coincides with the direction φ'_{01} of the vector $\vec{R}'_{01}$.

In a similar way we can obtain for the wave zone $(kR'_{12} \gg 1)$

$$I'_{12} = \exp\left(i\frac{\pi}{4}\right)\sqrt{\frac{R}{2\pi r'_{12}}}\int_{-\frac{\pi}{2}+i\infty}^{\frac{\pi}{2}-i\infty} d\theta_2\sqrt{\sin\theta_2}\times$$

$$\times\left[V(\theta_2,\varphi'_{12}) - 1\right]\exp\left[ikR'_{12}\cos(\theta_2 - \theta'_{12})\right]. \tag{29}$$

The integrals Eqs. (27) and (29) over a complex plane of angles are typical of the problem on the field from a point-size source above an interface [5, 6, 8], however with one complication, specifically, the impedance is dependent on the angle θ or θ_2. To the best author's knowledge, there is no precise method for calculating integrals like these. However, the saddle-point technique is quite an efficient asymptotic method for calculations in the wave zone.

4. SADDLE-POINT METHOD FOR THE INTEGRALS I'_{01} AND I'_{12}

The saddle-point technique is presented in monographs [5-8] with different degrees of furnishing the details required for our purposes. In the greatest detail the method is discussed in [8]. However the selection of the coordinate frame in this monograph differs from that used in the present study and in [5-7]. As a result, conformal maps of the complex plane are different too which necessitates a brief description of the technique using some details from [5-7]. Felsen and Marcuvitz [7] presented only schematically the solution of the problem on the filed produced by a point-size source field near an impedance plane. At the same time the assumption concerning the character of the solution ($\sin\theta_0 \sim 1$ or $\theta_0 \approx \pi/2$) made by Brekhovskikh [5] in the very beginning of § 20 (see page 236) does not allow the obtained results to be applicable for arbitrary locations of the source and observation point. Apparently, for this reason the solution was not included in the general form in the second edition of the monograph in 1973.

Going over from the complex plane of $k_\perp$ to the plane of θ requires the value $k_z = \left(k^2 - k_\perp^2\right)^{1/2}$ to be unambiguously determined on this plane. One of the conditions which determines such a selection for real-valued $k_z > 0$ is (see [6], page 27)

$$k_z > 0 \quad \text{for} \quad -k < k_\perp < k. \tag{30}$$

The requirement of finiteness of the integrand in Eq. (13) for $|k_z|\cdot|z_1 + z_0| \to \infty$ yields the second condition for all admissible complex-valued $k_\perp$, viz.

$$\operatorname{Im} k_z > 0, \tag{31}$$

To completely determine the two-valued function k_z, it is necessary to introduce a two-sheeted Riemannian surface of the complex-valued variable $k_\perp$, with the transition from one sheet of which to another being performed along the section line. The selection of the surface determines locations of the domains within the complex plane of $k_\perp$ which correspond to values of the square root with $\operatorname{Im} k_z > 0$ and $\operatorname{Im} k_z < 0$ (see [6], page 28).

Since $\sin\theta$ is a periodic function, the transformation

$$k_\perp = k\sin\theta, \tag{32}$$

involved in our consideration, maps the entire $k_\perp$-plane on any of the strips of width 2π lying within the θ-plane. The inverse function $\sin^{-1}(k_z/k)$ is multivalued on the $k_\perp$-plane, with the branching points given by the equality

$$\frac{dk_\perp}{d\theta} = k\cos\theta = 0.$$

The first-order branch points are located at $k_\perp = \pm k$.

Substitution of $\theta = \theta_r + i\theta_i$, with θ_r and θ_i being the real and imaginary parts of θ, into Eq. (32) yields for $k_\perp = k_{\perp r} + ik_{\perp i}$

$$k_{\perp r} = k \sin\theta_r \cosh\theta_i \quad \text{and} \quad k_{\perp i} = k \cos\theta_r \sinh\theta_i. \quad (33)$$

The four quadrants of the $k_\perp$-plane are mapped into four half-strips (see Fig. 2) which correspond to Eq. (33) and form the strip $-\frac{\pi}{2} \le \theta_r \le \frac{\pi}{2}$, $-\infty \le \theta_i \le \infty$. These ranges are periodically repeated within the θ-plane as θ_r is changed by a value multiple of 2π.

Let us draw cut sets within the $k_\perp$-plane along the real axis from $-k$ to $-\infty$ and from $+k$ to $+\infty$, and assume

$$k_z = \sqrt{k^2 - k_\perp^2} = +k\cos\theta = \\ = k(\cos\theta_r \cosh\theta_i - i \sin\theta_r \sinh\theta_i). \quad (34)$$

Since with $k_\perp = 0$ we have $k_z = k$, the choice of this sign corresponds to mapping the point $k_z = 0$ into the point $\theta = 0$. Moreover the strip $-\frac{\pi}{2} \le \theta \le \frac{\pi}{2}$ corresponds to the upper sheet of the surface where $\mathrm{Re}\, k_z > 0$, with $\mathrm{Im}\, k_z > 0$ within regions 2 and 4 while $\mathrm{Im}\, k_z < 0$ within regions 1 and 3. Any adjacent strip of width π on the plane of complex-valued θ can represent the second sheet of the Riemannian surface. Figs. 2 and 3 illustrate the correspondence of the regions for this mapping.

The function $f_V(\theta, \varphi'_{01})$ given by the relation Eq. (20) shows the presence of a pole in the point $\theta = \theta_p$ which is determined from the condition

$$\cos\theta + \eta(\theta, \varphi'_{01}) = 0. \quad (35)$$

In the case of small values of the impedance $(|\eta| \ll 1)$ Eq. (35) can be solved by the iteration method. With $\theta_p \approx \frac{\pi}{2}$ selected in the capacity of the zeroth-order approximation, the next iteration yields

$$\cos\theta_p = -\eta\left(\frac{\pi}{2}, \varphi'_{01}\right). \quad (36)$$

The physically realizable values of the impedance are characterized by $\mathrm{Re}\,\eta > 0$. Hence, θ_p lies within

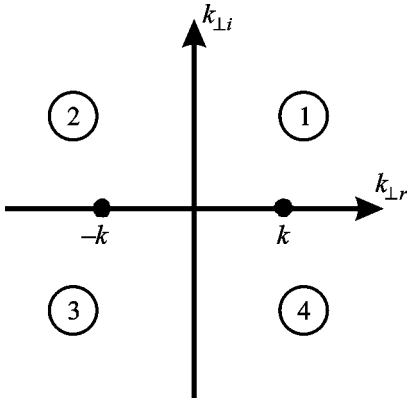

FIG. 2: The plane of complex-valued $k_\perp$

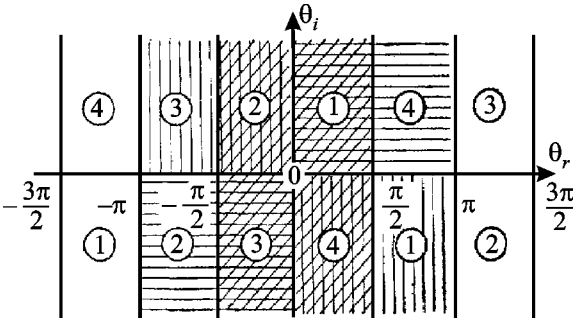

FIG. 3: The plane of complex-valued θ

either the plane $\left(\frac{\pi}{2}, \pi\right)$ or $\left(-\pi, -\frac{\pi}{2}\right)$ near the real axis. The second value can be disregarded [8]. The reason is that the corresponding point is located rather far from the saddle-point integration path and hence, provides for an exponentially small contribution. Therefore the value $\theta_p = \frac{\pi}{2} + \Delta\theta_p$, with $\sin\Delta\theta_p = \eta\left(\frac{\pi}{2}, \varphi'_{01}\right)$, remains alone to be taken into account. Whence it follows that

$$\theta_p \approx \frac{\pi}{2} + \eta\left(\frac{\pi}{2}, \varphi'_{01}\right). \quad (37)$$

Omitting the argument of the impedance for the sake of brevity of the notation, we can write for the real, θ_{pr}, and imaginary, θ_{pi}, parts of θ

$$\theta_{pr} = \frac{\pi}{2} + \eta_r \quad \text{and} \quad \theta_{pi} = \eta_i. \tag{38}$$

Under the condition $kR_{01} \gg 1$, the quick variations of the integrand in Eq. (27) with changing θ are provided by the exponential factor $\exp\left[ikR'_{01} f(\theta)\right]$, where

$$f(\theta) = i\cos(\theta - \theta'_{01}). \tag{39}$$

The stationary point $\theta_s = \theta'_{01}$ is determined from the condition

$$\left.\frac{df}{d\theta}\right|_{\theta_s} = -i\sin(\theta - \theta'_{01}) = 0, \tag{40}$$

with $f(\theta_s) = i\cos 0 = i$. According to the saddle-point technique let us introduce a new variable s through the relation $f(\theta) - f(\theta_s) = s^2$, whence it follows that

$$s = \pm\sqrt{2}\exp(i\pi/4)\sin\frac{\theta - \theta'_{01}}{2}. \tag{41}$$

The saddle-point integration path is determined from the condition

$$\operatorname{Im} f(\theta) = \operatorname{Im} f(\theta_s) = 1. \tag{42}$$

Making use of Eq. (41) we can obtain

$$\left.\frac{d\theta}{ds}\right|_{S=0} = \left(\frac{ds}{d\theta}\right)^{-1}_{\theta_s} = \pm\sqrt{2}\exp(i\pi/4). \tag{43}$$

The argument in Eq. (43) near $\theta = \theta_s$ should coincide with the argument $\theta - \theta_s$. Hence the upper sign "+" should be selected in Eqs. (41) and (43).

The equation (42) for the saddle-point integration path yields

$$\cos(\theta_r - \theta'_{01})\cosh\theta_i = 1 \tag{44}$$

or

$$\theta_r - \theta'_{01} = \cos^{-1}\left(1/\cosh\theta_i\right). \tag{45}$$

With $\theta_i \to \pm\infty$ the contour of integration asymptotically tends to $\theta_r - \theta'_{01} = \pm\pi/2$, as is shown in Fig. 4. The process of conversion of the initial contour into the saddle-point integration path can be traced using the transformation of the plane θ into the plane s given by Eq. (41). The branching points $s = \pm s_b = \pm\sqrt{2}\exp(i\pi/4)$ and cut sets are shown in Fig. 5 borrowed from [6] (see page 481).

The pole $\theta_p \approx \frac{\pi}{2} + \eta$ is transferred into the point $s = s_p$ according to the relation

$$s_p = \sqrt{2}\exp(i\pi/4)\sin\frac{\theta_p - \theta'_{01}}{2}. \tag{46}$$

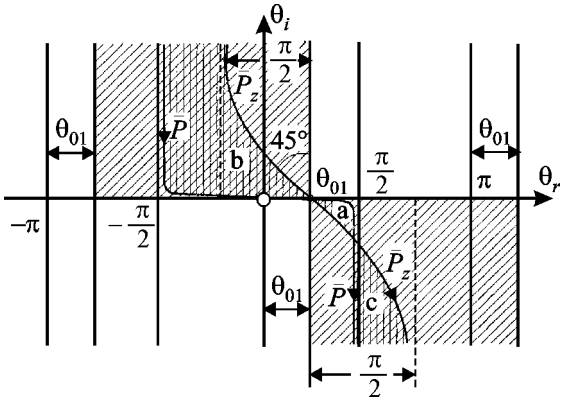

FIG. 4: The initial, $\bar{P}$, and modified, $\bar{P}_z$, contours of integration within the θ-plane

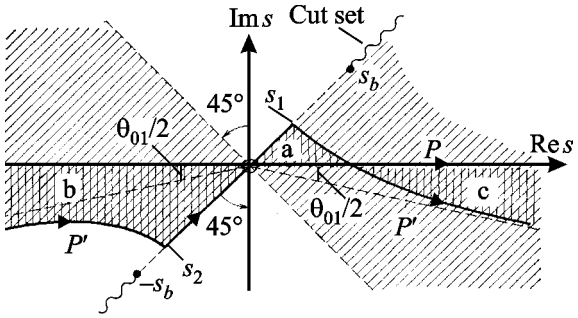

FIG. 5: The initial, P', and modified, P contours of integration within the s-plane, with $\left(s_{1,2} = +\sqrt{2}\exp(i\pi/4)\sin\left(\frac{\pi}{4} \pm \frac{\theta_{01}}{2}\right)\right)$

Making use of Eq. (46) we can obtain for small impedances $(|\eta| \ll 1)$ [8]

$$s_p \approx \exp(i\pi/4)\left[1+\eta\cos\theta'_{01}-\sqrt{1-\eta}\sin\theta'_{01}\right]^{1/2}. \quad (47)$$

By introducing the grazing angle

$$\psi'_{01} = \frac{\pi}{2} - \theta'_{01}, \quad (48)$$

it can be shown [8] that $\mathrm{Im}\, s_p < 0$ provided that

$$|\eta_i| > \eta_r + \psi'_{01} \quad \text{and} \quad \arg\eta < -\pi/4, \quad (49)$$

i.e. the impedance should be of a "strongly inductive" character. In this case the initial contour crosses the pole in the course of transformation into the saddle-point integration path. For this reason it is necessary to add the residue in the point $s = s_p$ to the integral taken over the contour of the quickest descent.

In the case of "weakly inductive" or "capacitive" impedances we have $\arg\eta > -\pi/4$, and hence the contour of integration does not cross the pole in the course of transformation since the latter lies within the upper half-plane $(\mathrm{Im}\, s_p > 0)$.

It follows from the condition Eq. (49) that the grazing angle for which $\mathrm{Im}\, s_p < 0$ with $\arg\eta < -\pi/4$ is small, viz.

$$\psi'_{01} < \psi_{cr} = |\eta_i| - \eta_r \ll 1.$$

To summarize we can write

$$I'_{01} = I_{qd} + \begin{cases} 0, & \text{if} \quad s_p > 0, \\ Q, & \text{if} \quad s_p < 0, \end{cases} \quad (51)$$

where

$$Q = -i4\pi\eta_p \exp(i\pi/4)\sqrt{\frac{k}{2\pi}}\frac{\exp(ikr'_{01})}{\sqrt{r'_{01}}}\times$$

$$\times\exp\left[-ik\eta_p(z_1+z_0)\right], \quad (52)$$

$$\eta_p = \eta(\theta_p, \varphi'_{01}) \approx \eta(\pi/2, \varphi'_{01}),$$

and I_{qd} is the integral taken over the modified contour of the quickest descent.

The value Q describes a surface wave (Cennek wave) decaying away from the boundary as $\exp\left[-ik\eta_p(z_0+z_1)\right]$, while as $1/\sqrt{r'_{01}}$ along the boundary.

The integral I_{qd} can be expressed as

$$I_{qd} = \sqrt{\frac{k}{\pi r'_{01}}}\exp(ikR'_{01})\int_{-\infty}^{\infty}\frac{\exp(-kR'_{01}s^2)}{s-s_p}\Phi(s)\mathrm{d}s, \quad (53)$$

$$\Phi(s) = \frac{(\sin\theta)^{1/2}}{\cos\dfrac{\theta-\theta'_{01}}{2}}\frac{-2\eta(\theta,\varphi'_{01})}{\cos\theta+\eta(\theta,\varphi'_{01})}(s-s_p). \quad (54)$$

Here $\theta = \theta(s)$ and $\mathrm{d}\theta = \left(\dfrac{\mathrm{d}s}{\mathrm{d}\theta}\right)^{-1}\mathrm{d}s$ are inverse functions of s determined from the dependences Eqs. (41) and (43), respectively.

When going over from θ to s we have multiplied and divided the integrand by $(s-s_p)$ in order to isolate the pole $(s-s_p)^{-1}$ in the explicit form. It is evident that $\Phi(s)$ in Eq. (54) is a regular function in the point $s = s_p$ and can be expanded in powers of s in the vicinity of the saddle point. Cutting the series expansion down to the leading term, we have

$$\Phi(s) = \Phi(0) + \ldots \approx \sqrt{\sin\theta'_{01}}\frac{-2\eta(\theta'_{01},\varphi'_{01})}{\cos\theta'_{01}+\eta(\theta'_{01},\varphi'_{01})}(-s_p). \quad (55)$$

Here we have taken into account that $\theta \to \theta'_{01}$ with $s \to 0$.

Multiplying the integrand by $\dfrac{s+s_p}{s+s_p} \equiv 1$ and taking into account the property of its parity we can obtain

$$I_{qd} \approx s_p^2\frac{2\eta(\theta'_{01},\varphi'_{01})}{\cos\theta'_{01}+\eta(\theta'_{01},\varphi'_{01})}\sqrt{\frac{kR'_{01}}{\pi}}\times$$

$$\times\frac{\exp(ikR'_{01})}{R'_{01}}\int_{-\infty}^{\infty}\frac{\exp(-kR'_{01}s^2)}{s^2-s_p^2}\mathrm{d}s. \quad (56)$$

Denoting $\nu = \sqrt{kR'_{01}}s$ and $\nu_p = \sqrt{kR'_{01}}s_p$ and taking into account the relation Eq. (20) we can write

$$I_{qd} = \left[1 - V(\theta'_\alpha, \varphi'_{01})\right] \frac{\exp(ikR'_{01})}{R'_{01}} \frac{\nu_p^2}{\sqrt{\pi}} \int_{-\infty}^{\infty} \frac{\exp(-\nu^2)}{\nu^2 - \nu_p^2} d\nu. \tag{57}$$

As can be shown [8], the integral in the right-hand part of Eq. (57) is reducible to an expression containing the error function of a complex-valued argument, viz.

$$I(\nu_p) = \frac{2\sqrt{\pi}}{\nu_p} \exp(-\nu_p^2) \int_{\nu_p}^{i\infty \cdot \alpha} \exp(\nu^2) d\nu, \tag{58}$$

where $\alpha = \operatorname{sgn} \operatorname{Im} \nu_p = \operatorname{sgn} \operatorname{Im} s_p$. Similar integrals in [5] (see page 241) and [6] (see page 496) can differ by the factor $\pm i$ in front of the integration variable.

In the presence of the residue θ in the pole we can combine it with I_{qd} to obtain a unique asymptotic representation (see Eq. (14.45) in [8]) which is independent of the value $\operatorname{sgn} \operatorname{Im} s_p$, viz.

$$I'_{01} = \left[1 - V(\theta'_{01}, \varphi'_{01})\right] \frac{\exp(ikR'_{01})}{R'_{01}} 2\nu_p \exp(-\nu_p^2) \times$$

$$\times \int_{-\infty}^{i\infty} \exp(\nu^2) d\nu. \tag{59}$$

Now let us substitute the obtained expression into the formula Eq. (27) and the result into Eq. (10). Then, making an identical transformation consisting of adding and subtracting the term $\frac{\exp(ikR'_{01})}{R'_{01}} V(\theta'_{01}, \varphi'_{01})$, we arrive at

$$I_{01} = \frac{\exp(ikR_{01})}{R_{01}} + V(\theta'_{01}, \varphi'_{01}) \frac{\exp(ikR'_{01})}{R'_{01}} +$$

$$+ \left[1 - V(\theta'_{01}, \varphi'_{01})\right] W'_{01} \frac{\exp(ikR'_{01})}{R'_{01}}, \tag{60}$$

where

$$W'_{01} = 1 + 2\nu_p \exp(-\nu_p^2) \int_{\nu_p}^{i\infty} \exp(\nu^2) d\nu \tag{61}$$

is the "propagation factor" for the path R'_{01}. It is evident that the "propagation factor" introduced in such a manner coincides with the respective expression for the vertical component of the electric field radiated by a vertical electric dipole (see [8], page 105).

In a similar way we can obtain

$$I_{12} = \frac{\exp(ikR_{12})}{R_{12}} + V(\theta'_{12}, \varphi'_{12}) \frac{\exp(ikR'_{12})}{R'_{12}} +$$

$$+ \left[1 - V(\theta'_{12}, \varphi'_{12})\right] W'_{12} \frac{\exp(ikR'_{12})}{R'_{12}}. \tag{62}$$

The asymptotic behavior shown by the "propagation factors" W'_{01} and W'_{12} is determined by magnitudes of the respective numerical distances. In the case of W'_{01} we have

$$w'_{01} = \left(\sqrt{kR'_{01}}s_p\right)^2 =$$

$$= ikR'_{01}\left[1 + \eta \sin\psi'_{01} - \sqrt{1 - \eta^2}\cos\psi'_{01}\right]. \tag{63}$$

Call to mind that ψ'_{01} is the grazing angle determined by Eq. (48). The corresponding expression for w'_{12} can be obtained by changing $R'_{01} \to R'_{12}$ and $\psi'_{12} \to \frac{\pi}{2} - \theta'_{12}$ in Eq. (63).

Numerical distances increase with the grazing angle. For $\psi'_{01} = \psi'_{12} = 0$ we have

$$w'_{01} \approx ikR'_{01}\eta^2/2 \quad \text{and} \quad w'_{12} \approx ikR'_{12}\eta^2/2, \tag{64}$$

whereas if $\psi'_{01} \to \psi'_{12} = \pi/2$, then

$$\left|w'_{01}\right| \approx kR'_{01}\left|1 + \eta\right| \gg 1 \text{ and } w'_{12} \approx kR'_{12}\left|1 + \eta\right| \gg 1. \tag{65}$$

In the case given by Eq. (64) $\left|w'_{01}\right|$ and $\left|w'_{12}\right|$ can assume both small and large magnitudes depending on the values kR'_{01} and kR'_{12}, and smallness of $\left|\eta^2\right|$. Excepting the case of a "strongly inductive" impedance $(\arg\eta > -\pi/4)$, the propagation factor can be asymptotically expressed as

$$W'_{01} \approx 1 + i\sqrt{\pi w'_{01}} + O(w'_{01}) \quad \text{for} \quad \left|w'_{01}\right| \ll 1 \tag{66}$$

or

$$W'_{01} \approx -\frac{1}{2w'_{01}}\left(1+\frac{3}{2w'_{01}}+...\right) \quad \text{for} \quad |w'_{01}| \gg 1. \qquad (67)$$

The behavior shown by I_{01} and I_{12} as the incidence (grazing) angle is changed can be rather easily analyzed for limiting cases. If $\psi'_{01}, \psi'_{12} \gg \psi_{Br}$, where $\psi_{Br} \sim |\eta|$ is the Brewster angle, then $\cos\theta'_{01}, \cos\theta'_{12} \gg |\eta|$ and $V(\theta'_{01}, \varphi'_{01}), V(\theta'_{12}, \varphi'_{12}) \to 1$ while the factor $[1-V]$ in Eq. (60) tends to zero ($[1-V] \to 0$). In addition the case given by Eq. (67) is realized. As a result, I_{01} and I_{12} describe the "two-beam interference" for the signal from a real source and that from the mirror source multiplied by the respective reflection factor. In the opposite case with $\psi'_{01}, \psi'_{12} \ll \psi_{Br}$ we have $\cos\theta'_{01}, \cos\theta'_{12} \ll |\eta|$ and accordingly $R'_{01} \to R_{01}$; $R'_{12} \to R_{12}$; $V(\theta'_{01}, \varphi'_{01}), V(\theta'_{12}, \varphi'_{12}) \to -1$ and $[1-V] \to +2$. As a result, the direct and mirror beams cancel each other and the field is determined by the effects of reradiation and attenuation due to the interface.

To substitute Eq. (2) into Eq. (1) it is necessary to calculate the respective derivatives of I_{01} at $z_1 = 0$. The structure of the formula Eq. (60) for I_{01} is such that the main contribution to the result of differentiation is provided by the exponential factors, viz.

$$\nabla_1 I_{01}\big|_{z=0} \approx ik\vec{\alpha}_\perp \frac{\exp(ikR_{01})}{R_{01}} \times$$

$$\times\left\{(1+V'_{01})+(1-V'_{01})W'_{01}+O(1/kR'_{01})\right\}_{z_1=0},$$

$$\frac{\partial}{\partial z_1} I_{01}\bigg|_{z_1=0} \approx ik\alpha_z \frac{\exp(ikR_{01})}{R_{01}} \times$$

$$\times\left\{(-1+V'_{01})+(1-V'_{01})W'_{01}+O\left(1/\sqrt{kR'_{01}}\right)\right\}_{z_1=0},$$

and

$$\frac{\partial^2}{\partial z_1^2} I_{01}\bigg|_{z_1=0} \approx -k^2\alpha_z^2 \frac{\exp(ikR_{01})}{R_{01}} \times$$

$$\times\left\{(1+V'_{01})+(1-V'_{01})W'_{01}+O\left(1/\sqrt{kR'_{01}}\right)\right\}_{z_1=0}.$$

Here $-\alpha_z = -\frac{z_0}{R_{01}}\bigg|_{z_1=0}$, $\alpha_z = \frac{z_0}{R'_{01}}\bigg|_{z_1=0}$ and $R_{01}|_{z_1=0} = R'_{01}|_{z_1=0}$. Also we have used the notation $V'_{01} = V(\theta'_{01}, \varphi'_{01})$ to make the writing shorter. If $\frac{1}{\sqrt{kR'_{01}}} \ll 1$, then in the above expressions we can confine ourselves to considering the terms represented in the explicit form.

Taking into account the above consideration the field fluctuations can be represented as

$$u(\vec{R}_2) = -\frac{1}{4\pi}\iint_S d^2\vec{r}_1 \frac{J_{01}J_{12}}{R_{01}R_{12}} \exp\left[ik(R_{01}+R_{12})\right]\Big|_{z_1=0}. \qquad (68)$$

Here

$$J_{01} = \Big\{[ik\vec{\alpha}_\perp \cdot \nabla_1\varsigma_1 + k^2\alpha_z^2\varsigma_1](1+V'_{01}) +$$

$$+k^2\alpha_z\eta_0(1-V'_{01})\varsigma_1 + [ik\vec{\alpha}_\perp \cdot \nabla_1\varsigma_1 + k^2\alpha_z^2\varsigma_1 +$$

$$+k^2\alpha_z\eta_0\varsigma_1](1-V'_{01})W'_{01}\Big\}\Big|_{z_1=0} \qquad (69)$$

and

$$J_{12} = \left\{(1+V'_{12})+(1-V'_{12})W'_{12}\right\}\Big|_{z_1=0}, \qquad (70)$$

where $\vec{\alpha}_\perp = \frac{\vec{r}_1}{R_{01}}$ and $\alpha_z = \frac{z_0}{R_{01}}$, with $R_{01} = \sqrt{r_1^2 + z_0^2}$ at $z_1 = 0$.

The integrand in Eq. (68) has been reduced under the assumption that the following conditions hold $kR'_{01} \gg 1$, $kR'_{12} \gg 1$ and $\cos\theta'_{01}, \cos\theta'_{12} \neq \pi/2$. The case where these conditions violate requires using suitable approximations which do not affect essentially the amount of the integral. The heights z_0 and z_1 can assume here any arbitrary magnitudes. With this in mind the expression Eq. (68) can be regarded as an initial relation for calculating other statistics of the fluctuating field.

REFERENCES

1. Barrick, D. E., First-Order Theory and Analysis of MF/HF/VHF Scatter from the Sea, *IEEE Trans. Antennas. Propag.*, AP-20(1):2-10, 1972 (in Russian).
2. Bass, F. G. and Fuks, I. M. Wave Scattering from Statistically Rough Surfacesm. Moscow: Nauka; 1972 (in Russian).
3. Bryukhovetski, A. S., The perturbation method in the theory of wave scattering by statistically rough surfaces, *Radiofizika i Radioastronomia*, 11(3):254-263, 2006 (in Russian).
4. Bryukhovetski, A. S., On a version of the perturbation method in the theory of wave scattering by statistically rough surfaces, *Izv. Vyssh. Uchebn. Zaved. Radiofiz. (Sov. Radiophys.)*, 31(3):321-326, 1988 (in Russian).
5. Brekhovskikh, L. M. Waves in layered media. Izd. Acad. Sci. USSR; 1957 (in Russian).
6. Felsen, L. B. and Marcuvitz, N. Radiation and Scattering of Waves. Vol. 1. Moscow: Mir; 1978 (in Russian).
7. Felsen, L. B. and Marcuvitz, N. Radiation and Scattering of Waves. Vol. 2. Moscow: Mir; 1978 (in Russian).
8. Makarov, G. I., Novikov, V. V., and Rybachek, S. T. Electromagnetic wave propagation over the Earth's surface. Moscow: Nauka; 1991 (in Russian).
9. Gradshteyn, I. S. and Ryzhik, I. M. Tables of Integrals, Sums, Series, and Products. Moscow: Fizmatgiz; 1962 (in Russian).
10. Abramowitz, M. and Stegun, I. A. Handbook of mathematical functions. Moscow: Nauka; 1979 (in Russian).

Radio Physics and Radio Astronomy, 1(1), 49–55 (2010)

NEAR-FIELD SCATTERING OF WAVES FROM A STATISTICALLY ROUGH SURFACE: II. AVERAGE INTENSITY AND FREQUENCY SPECTRUM OF FIELD FLUCTUATIONS

A. S. Bryukhovetski

A. Usikov Institute of Radio Physics and Electronics, National Academy of Sciences of Ukraine, 12, Academician Proskura St., Kharkiv 61085, Ukraine

*Address all correspondence to A. S. Bryukhovetsky E-mail:ire@ire.kharkov.ua

The average intensity and frequency spectrum of fluctuations of the near field scattered by a statistically rough surface is determined. The derivations are based on the asymptotic expansion of the fluctuating field obtained in Part I of the paper. Limiting transitions to the familiar particular cases are analyzed.

KEY WORDS: *scattering, fluctuations, roung surface, spectrum, intensity*

Part II of the paper is aimed at determining the average intensity and frequency spectrum of the fluctuating field component based on the integral representation for the field that has been derived in Part I [1].

Proceeding from the expression Eq. (68) of paper [1], let us represent the average intensity of field fluctuations as (the asterisk "*" stands for complex conjugation)

$$\left\langle \left| u\left(\vec{R}_2\right)\right|^2 \right\rangle \equiv \left\langle u\left(\vec{R}_2\right) u^*\left(\vec{R}_2\right)\right\rangle =$$

$$= \frac{1}{(4\pi)^2}\iint_S \mathrm{d}^2\vec{r}_1 \mathrm{d}^2\vec{r}_1' \frac{1}{R_{01}' R_{01} R_{12}' R_{12}} \times$$

$$\times \exp\left\{ik\left[R_{01}' - R_{01} + R_{12}' - R_{12}\right]\right\}\left\langle J_{01}^* J_{01}' \right\rangle J_{12}^* J_{12}'\Big|_{z_1=z_1'=0}, \quad (1)$$

where the substitutions as follows $\vec{r}_1 \to \vec{r}_1'$ and $z_1 \to z_1'$ have been made in all the primed values. Call to mind that

$$R_{01}\big|_{z_1=0} = \sqrt{r_{01}^2 + (z_1 - z_0)^2}\Big|_{z_1=0}, \text{ with } \vec{r}_{01} = \vec{r}_1 - \vec{r}_0, \text{ and}$$

$$R_{12}\big|_{z_1=0} = \sqrt{r_{12}^2 + (z_2 - z_1)^2}\Big|_{z_1=0} \text{ with } \vec{r}_{12} = \vec{r}_2 - \vec{r}_1,$$

where $(\vec{r}_0, z_0)$, $(\vec{r}_1, z_1)$ and $(\vec{r}_2, z_2)$ are coordinates of the source location, and the scattering and observation points, respectively; and J_{01} and J_{12} are determined by Eqs. (69) and (70) of paper [1].

Let us denote $\vec{\rho} = \vec{r}_{01}' - \vec{r}_{01}$ and use the Fresnel diffraction approximation. Then retaining in the expansions the second-order terms with respect to ρ, in contrast to [2] (see page 104), and selecting the coordinate origin at $\vec{r}_0 = 0$ (in this case $\vec{r}_{01} = \vec{r}_1$ and $\vec{r}_{12} = \vec{r}_2 = \vec{D}$), we can obtain

$$R_{01}'\big|_{z_1=0} = \sqrt{(\vec{r}_1 + \vec{\rho})^2 + z_0^2} \approx R_{01} + \vec{\rho}\vec{\alpha}_\perp + \frac{\rho^2 - (\vec{\rho}\vec{\alpha}_\perp)^2}{2R_{01}} + \ldots\Big|_{z_1=0}$$

and

$$R'_{12}\big|_{z_1=0} = \sqrt{(\vec{D}-\vec{r}_1-\vec{\rho})^2+z_2^2} \approx R_{12} - \vec{\rho}\vec{\beta}_\perp + \\ + \frac{\rho^2-(\vec{\rho}\vec{\beta}_\perp)^2}{2R_{12}} + \ldots \Bigg|_{z_1=0}.$$

Here $\vec{\alpha}_\perp = \frac{\vec{r}_1}{R_{01}}$ and $\vec{\beta}_\perp = \frac{\vec{D}-\vec{r}_1}{R_{12}}$.

In this notation we can write

$$R_{01} - R'_{01} + R_{12} - R'_{12} = (\vec{\beta}_\perp - \vec{\alpha}_\perp)\vec{\rho} + A\rho_x^2 + B\rho_y^2 + C\rho_x\rho_y, \quad (2)$$

where $\vec{\rho} = (\rho_x, \rho_y)$, with ρ_x and ρ_y being component of the vector $\vec{\rho}$ within the plane S, and $\vec{\alpha}_\perp = (\alpha_x, \alpha_y)$ and $\vec{\beta}_\perp = (\beta_x, \beta_y)$.

The equality Eq. (2) involves the following contracted notation for real-valued quantities

$$A = -\frac{1}{2}\left(\frac{1}{R_{01}} + \frac{1}{R_{12}}\right) + \frac{1}{2}\left(\frac{\alpha_x^2}{R_{01}} + \frac{\beta_x^2}{R_{12}}\right) < 0,$$

$$B = -\frac{1}{2}\left(\frac{1}{R_{01}} + \frac{1}{R_{12}}\right) + \frac{1}{2}\left(\frac{\alpha_y^2}{R_{01}} + \frac{\beta_y^2}{R_{12}}\right) < 0,$$

and $C = \frac{\alpha_x\alpha_y}{R_{01}} + \frac{\beta_x\beta_y}{R_{12}} \leqslant 0.$

Then the exponential term in the integral Eq. (1) can be brought to the form

$$\exp\{-ik(R_{01} - R'_{01} + R_{12} - R'_{12})\} = \\ = \exp\{-ik(\vec{\beta}_\perp - \vec{\alpha}_\perp)\vec{\rho}\} \cdot M(\vec{\rho}), \quad (3)$$

where the exponent $M(\vec{\rho})$ can be represented as the Fourier expansion

$$M(\vec{\rho}) = \exp\{-ik\left(A\rho_x^2 + B\rho_y^2 + C\rho_x\rho_y\right)\} = \\ = \int_{-\infty}^{\infty} dq_x \int_{-\infty}^{\infty} dq_y \exp(-i\vec{q}\vec{\rho})\tilde{M}(\vec{q}), \quad (4)$$

where

$$\tilde{M}(\vec{q}) = \frac{1}{(2\pi)^2}\int_{-\infty}^{\infty} d\rho_x \int_{-\infty}^{\infty} d\rho_y \exp(i\vec{q}\vec{\rho}) M(\vec{\rho}). \quad (5)$$

Calculation of the integral yields

$$\tilde{M}(\vec{q}) = \frac{1}{(2\pi)^2} \frac{\gamma_1\gamma_2}{k\sqrt{|B|\left|A - \frac{C^2}{4B}\right|}} \times \\ \times \exp\left[\frac{i}{4k}\left(\frac{q_y^2}{B} + \frac{\left(q_x - q_y\frac{C}{2B}\right)^2}{A - \frac{C^2}{4B}}\right)\right], \quad (6)$$

where $\gamma_1 = \sqrt{\pi}\exp\left(-i\frac{\pi}{4}\operatorname{sgn} B\right)$

and $\gamma_2 = \sqrt{\pi}\exp\left[-i\frac{\pi}{4}\operatorname{sgn}\left(A - \frac{C^2}{4B}\right)\right]$.

If in Eq. (6) $B \to 0$ or $A - \frac{C^2}{4B} \to 0$, then the respective part of the expression turns into the Dirac delta function.

Let us represent random elevations figuring in the values J_{01}^* and J'_{01} (see Eqs. (69) and (70) in [1]) as the Fourier expansion

$$\varsigma(\vec{r}_1) = \iint_{-\infty}^{\infty} d^2\vec{\chi}_1 \tilde{\varsigma}(\chi_1) \exp(i\vec{\chi}_1\vec{r}_1), \quad (7)$$

and proceed in a similar way with $\varsigma(\vec{r}_1') = \varsigma(\vec{r}_1 + \vec{\rho})$. Then going over in Eq. (1) to integration over $\vec{r}_1$ and $\vec{\rho}$ instead of $\vec{r}_1$ and $\vec{r}_1'$ we can obtain

$$\left\langle \left|u\left(\vec{R}_2\right)\right|^2 \right\rangle = \frac{1}{(4\pi)^2}\iint_S d^2\vec{r}_1 \int\int_{-\infty}^{\infty} d^2\vec{\rho} \frac{J'_{12}J_{12}^*}{R_{01}R_{01}^*R_{12}^*R_{12}} \times \\ \times \int\int_{-\infty}^{\infty} d^2\vec{\chi}_1 \int\int_{-\infty}^{\infty} d^2\vec{\chi}' \int\int_{-\infty}^{\infty} d^2\vec{q} \left\langle \tilde{\xi}^*(\vec{\chi}_1)\tilde{\xi}(\vec{\chi}_1')\right\rangle \times \\ \times \tilde{J}'_{01}(\vec{\chi}_1')\tilde{J}_{01}^*(\vec{\chi}_1) \cdot \tilde{M}(\vec{q}) \exp\left[-i\vec{q}\vec{\rho} + i\vec{\chi}_1'\vec{\rho} - ik(\vec{\beta}_\perp - \vec{\alpha}_\perp)\vec{\rho}\right] \times \\ \times \exp\left[-i(\vec{\chi}_1 - \vec{\chi}_1')\vec{r}_1\right]. \quad (8)$$

The formula Eq. (8) has been derived on the usual assumption that the correlation length of irregularities is much smaller than the characteristic size of the scattering surface. For this reason integration over $\vec{\rho}$ is performed in the infinite limits. Application of asymptotic computation techniques, like, for example, the stationary phase method, allows neglecting the difference ρ in expressions for the primed values R'_{01}, R'_{12}, ... in contrast to the unprimed ones. In addition the field of surface irregularities is assumed to be statistically homogeneous such that by virtue of the Wiener–Khinchin theorem we have

$$\left\langle \tilde{\varsigma}^*(\vec{\chi}_1)\tilde{\varsigma}(\vec{\chi}'_1)\right\rangle = \sigma^2\tilde{W}(\vec{\chi}_1)\delta(\vec{\chi}_1-\vec{\chi}'_1), \tag{9}$$

where $\sigma^2\tilde{W}(\vec{\chi}_1)$ is the spatial power spectrum of the irregularities.

The result of integration over $\vec{\rho}$ is $(2\pi)^2\delta\left[\vec{\chi}'_1-\vec{q}-k\left(\vec{\beta}_\perp-\vec{\alpha}_\perp\right)\right]$. Hence with account of Eq. (9) the formula Eq. (8) can be brought to the form

$$\left\langle\left|u\left(\vec{R}_2\right)\right|^2\right\rangle = \frac{\sigma^2}{4}\iint_S \mathrm{d}^2\vec{r}_1\frac{|J_{12}|^2}{R_{01}^2R_{12}^2}\times$$
$$\times\int\int_{-\infty}^{\infty}\mathrm{d}^2\vec{q}\left|\tilde{J}_{01}\left[k\left(\vec{\beta}_\perp-\vec{\alpha}_\perp\right)+\vec{q}\right]\right|^2\times$$
$$\times\tilde{W}\left[k\left(\vec{\beta}_\perp-\vec{\alpha}_\perp\right)+\vec{q}\right]\tilde{M}(\vec{q}). \tag{10}$$

The expression for $\tilde{J}_{01}(\vec{\chi}_1)$ can be obtained from the formula for J_{01} by replacing $\nabla_1\varsigma_1$ with $i\vec{\chi}_1$ and ς_1 with 1.

Let us go over in the inner integral over $\vec{q}$ to a dimensionless wavenumber $\vec{q}^\circ=\vec{q}/k$ $(\mathrm{d}^2\vec{q}=k^2\mathrm{d}^2\vec{q}^\circ)$ and denote the result as

$$I_q=\int\int_{-\infty}^{\infty}\mathrm{d}q_x^\circ\mathrm{d}q_y^\circ\exp\left[iGf(\vec{q}^\circ)\right]F(\vec{q}^\circ), \tag{11}$$

where $G=kR\gg 1$, $R=\frac{1}{2}\frac{R_{01}R_{12}}{R_{01}+R_{12}}$ is the geometric mean of R_{01} and R_{12},

$$f(\vec{q}^\circ)=\frac{q_y^{\circ 2}}{4RB}+\frac{\left(q_x^\circ-\frac{q_y^\circ C}{2B}\right)^2}{4R\left(A-\frac{C^2}{4B}\right)},\quad\text{and}$$

$$F(\vec{q}^\circ)=\frac{1}{(2\pi)^2}\frac{2k\gamma_1\gamma_2}{\sqrt{4|B|\left|A-\frac{C^2}{4B}\right|}}\times$$

$$\times\left|\tilde{J}_{01}\left[k\left(\vec{\beta}_\perp-\vec{\alpha}_\perp\right)+k\vec{q}^\circ\right]\right|^2\tilde{W}\left[k\left(\vec{\beta}_\perp-\vec{\alpha}_\perp\right)+k\vec{q}^\circ\right].$$

To calculate Eq. (11) we will apply the asymptotic method of stationary phase. Let us make a transformation whose Jackobian is equal to 1, viz. $\xi_1=q_x^\circ-\frac{q_y^\circ C}{2B}$ and $\xi_2=q_y^\circ$. Then we can write

$$I_q=\int_{-\infty}^{\infty}\mathrm{d}\xi_1\int_{-\infty}^{\infty}\mathrm{d}\xi_2\exp\left[iGf(\vec{\xi})\right]F(\vec{\xi}), \tag{12}$$

where $f(\vec{\xi})=\frac{\xi_2^2}{4RB}+\frac{B}{R(4AB-C^2)}\xi_1^2$.

The stationary point for $f(\vec{\xi})$ is $\vec{\xi}_s=0$. The Hessian value at the stationary point is $\left|\det\frac{\partial^2 f}{\partial\xi_{is}\partial\xi_{js}}\right|=\left|R\cdot 4B\left(A-\frac{C^2}{4B}\right)\right|^{-1}$, while the signs of the Hessian eigenvalues d_1 and d_2 are equal to $\operatorname{sgn}d_1=\operatorname{sgn}\left(A-\frac{C^2}{4B}\right)$ and $\operatorname{sgn}d_2=\operatorname{sgn}B$, respectively.

As a result the leading term of the asymptotic representation calculated by the stationary phase method (see [3], page 529) becomes

$$I_q=\left|\tilde{J}_{01}\left[k\left(\vec{\beta}_\perp-\vec{\alpha}_\perp\right)\right]\right|^2\tilde{W}\left[k\left(\vec{\beta}_\perp-\vec{\alpha}_\perp\right)\right]. \tag{13}$$

Substitution of Eq. (13) into Eq. (10) yields finally

$$\left\langle\left|u\left(\vec{R}_2\right)\right|^2\right\rangle=\frac{\sigma^2}{4}\iint_S\mathrm{d}^2\vec{r}_1\frac{|J_{12}|^2}{R_{01}^2R_{12}^2}\times$$

$$\times\left|\tilde{J}_{01}\left[k\left(\vec{\beta}_\perp-\vec{\alpha}_\perp\right)\right]\right|^2\tilde{W}\left[k\left(\vec{\beta}_\perp-\vec{\alpha}_\perp\right)\right]. \tag{14}$$

Now let us analyze the behavior of the integrand in the expression Eq. (14) for two limiting cases of great

and small grazing angles ψ'_{01} and ψ'_{12}. Recall that $\psi'_{01} = \frac{\pi}{2} - \theta'_{01}$ and $\psi'_{12} = \frac{\pi}{2} - \theta'_{12}$, with $\cos\theta'_{01} = z_0/R_{01}$, and $\cos\theta'_{12} = z_2/R_{12}$. If the Brewster angle is $\psi_{Br} \sim |\eta|$ and $\psi'_{01}, \psi'_{12} \gg \psi_{Br}$, then the Fresnel reflection factors V'_{01} and V'_{12} in the expressions

$$\tilde{J}_{01}\left[k\left(\vec{\beta}_\perp - \vec{\alpha}\right)\right] =$$

$$= \left[-k\vec{\alpha}_\perp\vec{\chi}_1 + k^2\alpha_z^2\right](1+V'_{01}) + k^2\alpha_z\eta_0(1-V'_{01}) +$$

$$+\left[-k\vec{\alpha}_\perp\vec{\chi}_1 + k^2\alpha_z^2 + k^2\alpha_z\eta_0\right](1-V'_{01})W'_{01}\Big|_{\vec{\chi}_1 = k\left(\vec{\beta}_\perp - \vec{\alpha}_\perp\right)} \tag{15}$$

and

$$J_{12} = (1+V'_{12}) + (1-V'_{12})W'_{12}, \tag{16}$$

with W'_{01} and W'_{12} being the propagation factors [1], both tend to one $(V'_{01}, V'_{12} \to 1)$.

As a result, taking into account that $\alpha_z^2 + \alpha_\perp^2 \equiv 1$ we can obtain

$$\tilde{J}_{01} \approx 2k^2\left[1 - \vec{\beta}_\perp\vec{\alpha}_\perp\right] \quad \text{and} \quad J_{12} \approx 2.$$

Then the formula Eq. (14) takes the form

$$\left\langle\left|u\left(\vec{R}_2\right)\right|^2\right\rangle = 4k^4\sigma^2\iint_S \mathrm{d}^2\vec{r}_1\,\frac{1}{R_{01}^2R_{12}^2}\times$$

$$\times\left(1 - \vec{\beta}_\perp\vec{\alpha}_\perp\right)^2\tilde{W}\left[k\left(\vec{\beta}_\perp - \vec{\alpha}_\perp\right)\right]. \tag{17}$$

The formula Eq. (17) is completely coincident with the expression Eq. (11) obtained by Bass and Fuks [2] (see page 105) for a rigid surface if the relationship between $\tilde{W}(\vec{\chi}_1)$ and the correlation function has been taken into account.

In the case of grazing propagation with $\psi'_{01}, \psi'_{12} \ll \psi_{Br}$, we have $V'_{01}, V'_{12} \to -1$, $\alpha_z \to 0$, $J_{12} \to 2W'_{12}$ and $\tilde{J}_{01} \to 2k^2\left(1 - \vec{\beta}_\perp\vec{\alpha}_\perp\right)W'_{01}$ such that the formula Eq. (14) takes the form

$$\left\langle\left|u\left(\vec{R}_2\right)\right|^2\right\rangle = 4k^4\sigma^2\iint_S \mathrm{d}^2\vec{r}_1\,\frac{1}{R_{01}^2R_{12}^2}\left(1 - \vec{\beta}_\perp\vec{\alpha}_\perp\right)^2\times$$

$$\times W'_{01}W'_{12}\tilde{W}\left[k\left(\vec{\beta}_\perp - \vec{\alpha}_\perp\right)\right]. \tag{18}$$

The transition to the soft surface in Eq. (14) cannot be performed since it implies another kind of the boundary conditions $(|\eta_0| \to \infty)$ and accordingly another kind of the reflection factors.

POWER FREQUENCY SPECTRUM OF THE FLUCTUATING FIELD COMPONENT

Let us consider wave scattering from an oscillating random surface $z = \varsigma(\vec{r}, t)$. With the assumption that these oscillations represent a quasistationary process $\left(\Omega \ll \omega_0, \text{ where } \Omega \sim \left|\frac{\partial\varsigma}{\partial t}\right| \Big/ |\varsigma|\right)$ the fluctuating field is described as before by the formula Eq. (68) of [4], however with changing $\varsigma(\vec{r}_1)$ to $\varsigma(\vec{r}_1, t)$ where t is regarded as a parameter, viz.

$$u\left(\vec{R}_2, t\right) = -\frac{\exp(-i\omega_0 t)}{4\pi}\times$$

$$\times\iint_S \mathrm{d}^2\vec{r}\,\frac{\exp\left[ik(R_{01}+R_{12})\right]}{R_{01}R_{12}}J_{01}J_{12}\Big|_{z_1=0}. \tag{19}$$

The formula Eq. (19) contains the explicit form of the time dependent factor $\exp(-i\omega_0 t)$ which has been omitted before. The factors J_{01} and J_{12} are given by the formulas Eq. (69) and (70), respectively, from [1], however with the first one involving now $\varsigma_1 = \varsigma(\vec{r}_1)$ instead of $\varsigma_1 = \varsigma(\vec{r}_1, t)$.

Let us construct the time-domain correlation function

$$B(\tau) = \left\langle u\left(\vec{R}_2, t+\tau\right)u^*\left(\vec{R}_2, t\right)\right\rangle =$$

$$= \frac{\exp(-i\omega_0\tau)}{(4\pi)^2}\iint_S\iint_S \mathrm{d}^2\vec{r}_1\mathrm{d}^2\vec{r}'_1\,\frac{J^*_{12}J'_{12}}{R_{01}R'_{01}R_{12}R'_{12}}\times$$

$$\times\left\langle J^*_{01}J'_{01}\right\rangle\exp\left[-ik(R_{01} - R'_{01} + R_{12} - R'_{12})\right]\Big|_{z_1=z'_1=0}. \tag{20}$$

This expression is similar to the formula Eq. (1) for the mean intensity apart from the factor $\exp(-i\omega_0\tau)$ and the time shift of the value $\varsigma(\vec{r}_1', t+\tau)$ figuring in J_{01}'. The rest of the primed values are the same as in Eq. (1).

Now let us represent $\varsigma(\vec{r}_1, t)$ as a Fourier expansion, viz.

$$\varsigma(\vec{r}_1, t) = \int_{-\infty}^{\infty} d\omega_1 \iint_{-\infty}^{\infty} d^2\vec{\chi}_1 \times$$
$$\times \sum_{j=\pm} \tilde{\varsigma}_j(\vec{\chi}_1) \exp\left[i(\vec{\chi}_1\vec{r}_1 - \omega_1 t)\right] \delta(\omega_1 - \omega_j), \qquad (21)$$

where $\omega_j = \Omega_j(\vec{\chi}_1)$ are frequencies determined by the dispersion relation for the surface oscillations. Substitution of Eq. (21) into the expressions for J_{01}' and J_{01}^* yields

$$\left\langle J_{01}^* J_{01}' \right\rangle = \int_{-\infty}^{\infty} d\omega_1 \int_{-\infty}^{\infty} d\omega_1' \iint_{-\infty}^{\infty} d^2\vec{\chi}_1 \times$$
$$\times \iint_{-\infty}^{\infty} d^2\vec{\chi}_1' \sum_{j=\pm} \sum_{j'=\pm} \tilde{J}_{01}^*(\vec{\chi}_1) \tilde{J}_{01}'(\vec{\chi}_1') \times$$
$$\times \exp\left[-i(\vec{\chi}_1 - \vec{\chi}_1')\vec{r}_1\right] \exp(i\vec{\chi}_1'\vec{\rho}) \exp\left[i(\omega_1 - \omega_1')t - i\omega_1'\tau\right] \times$$
$$\times \left\langle \tilde{\varsigma}_j^*(\vec{\chi}_1) \tilde{\varsigma}_{j'}(\vec{\chi}_1') \right\rangle \delta(\omega_1 - \omega_j) \delta(\omega_1' - \omega_{j'}). \qquad (22)$$

The values $\tilde{J}_{01}(\vec{\chi}_1')$ and $\tilde{J}_{01}^*(\vec{\chi}_1)$ are determined by Eq. (15).

Let the random field of irregularities be statistically homogeneous and stationary. Then making use of the Wiener–Khinchin theorem the correlation function of the spectral amplitudes [4] can be represented as

$$\left\langle \tilde{\varsigma}_j^*(\vec{\chi}_1) \tilde{\varsigma}_{j'}(\vec{\chi}_1') \right\rangle = \frac{\sigma^2}{2} \tilde{W}_j(\vec{\chi}_1) \delta_{jj'} \delta(\vec{\chi}_1 - \vec{\chi}_1'). \qquad (23)$$

Whence it follows that

$$\left\langle J_{01}^* J_{01}' \right\rangle = \frac{\sigma^2}{2} \iint_{-\infty}^{\infty} d^2\vec{\chi}_1 \sum_{j=\pm} \left|\tilde{J}_{01}(\vec{\chi}_1)\right|^2 \tilde{W}_j(\vec{\chi}_1) \times$$
$$\times \exp\left[i(\vec{\chi}_1\vec{\rho} - \omega_j\tau)\right]. \qquad (24)$$

Substituting Eq. (24) into Eq. (22) and then the result into Eq. (20) we arrive at

$$B(\tau) = \frac{\exp(-i\omega_0\tau)}{(4\pi)^2} \frac{\sigma^2}{2} \times$$
$$\times \iint_S d^2\vec{r}_1 \iint_{-\infty}^{\infty} d^2\vec{\rho} \frac{\exp\left[-ik\left(\vec{\beta}_\perp - \vec{\alpha}_\perp\right)\vec{\rho}\right]}{R_{01}^2 R_{12}^2} \times$$
$$\times \exp\left[-ik(A\rho_x^2 + B\rho_y^2 + C\rho_x\rho_y)\right] \left|J_{12}\right|^2 \times$$
$$\times \iint_{-\infty}^{\infty} d^2\vec{\chi}_1 \sum_{j=\pm} \left|\tilde{J}_{01}(\vec{\chi}_1)\right|^2 \tilde{W}_j(\vec{\chi}_1) \exp\left[i(\vec{\chi}_1\vec{\rho} - \omega_j\tau)\right]. \qquad (25)$$

Making use of the Fourier expansion Eqs. (4) through (6) for $M(\vec{\rho})$ we can obtain

$$B(\tau) = \frac{\exp(-i\omega_0\tau)}{4} \frac{\sigma^2}{2} \iint_S d^2\vec{r}_1 \frac{\left|J_{12}\right|^2}{R_{01}^2 R_{12}^2} \times$$
$$\times \iint_{-\infty}^{\infty} d^2\vec{\chi}_1 \tilde{M}\left[\vec{\chi}_1 - k\left(\vec{\beta}_\perp - \vec{\alpha}_\perp\right)\right] \times$$
$$\times \sum_{j=\pm} \left|\tilde{J}_{01}(\vec{\chi}_1)\right|^2 \tilde{W}_j(\vec{\chi}_1) \exp(-i\omega_j\tau). \qquad (26)$$

Now let us determine the frequency spectrum

$$S(\omega) = \frac{1}{2\pi} \int_{-\infty}^{\infty} B(\tau) \exp(i\omega\tau) d\tau, \qquad (27)$$

$$S(\omega) \equiv S(\omega_0 + \Delta\omega) = \frac{\sigma^2}{8} \iint_S d^2\vec{r}_1 \frac{\left|J_{12}\right|^2}{R_{01}^2 R_{12}^2} \times$$
$$\times \iint_{-\infty}^{\infty} d^2\vec{\chi}_1 \tilde{M}\left[\vec{\chi}_1 - k\left(\vec{\beta}_\perp - \vec{\alpha}_\perp\right)\right] \times$$
$$\times \sum_{j=\pm} \left|\tilde{J}_{01}(\vec{\chi}_1)\right|^2 \tilde{W}_j(\vec{\chi}_1) \delta(\Delta\omega - \omega_j), \qquad (28)$$

where $\Delta\omega = \omega - \omega_0$.

The expression Eq. (28) has much in common with the formula Eq. (10) for the mean intensity, which becomes especially clear after changing the variable $\vec{\chi}_1 \to k\left(\vec{\beta}_\perp - \vec{\alpha}_\perp\right) + \vec{q}$.

What essentially differs Eq. (28) from Eq. (10) is the presence of $\delta\left[\Delta\omega-\omega_j(\vec{\chi}_1)\right]$ under the integral. This makes it necessary to integrate first over the wavenumbers $\vec{\chi}_1$ figuring in the argument of the delta function regardless the quickness of variations in the rest part of the integrand.

Analysis of the spectrum Eq. (28) in the general case represents a rather complicated problem. For this reason we will confine ourselves to considering simplest particular cases.

Let us consider a specific kind of surface oscillations, namely, the gravity waves on a deep liquid in which case the dispersion relation is

$$\omega_j = j\sqrt{g\chi_1}, \quad \text{with} \quad j=\pm,$$

where g is the acceleration of gravity.

We will start from the situation where the quadratic terms $\sim k\rho^2/R$ in the exponential factor of $M(\vec{\rho})$ (formula Eq. (4)) can be neglected. This means that we can assume $A,B,C\to 0$ such that Eq. (5) yields $\tilde{M}(\vec{q})=\delta(\vec{q})$ and hence the correlation function becomes

$$B(\tau)=\frac{\exp(-i\omega_0\tau)}{4}\frac{\sigma^2}{2}\iint_S \mathrm{d}^2\vec{r}_1\frac{|J_{12}|^2}{R_{01}^2R_{12}^2}\times$$

$$\times\sum_{j=\pm}\left|\tilde{J}_{01}\left[k\left(\vec{\beta}_\perp-\vec{\alpha}_\perp\right)\right]\right|^2\tilde{W}_j\left[k\left(\vec{\beta}_\perp-\vec{\alpha}_\perp\right)\right]\exp(-i\omega_{1j}\tau). \tag{30}$$

Accordingly the spectrum can be expressed as

$$S(\omega)\equiv S(\omega_0+\Delta\omega)=\frac{\sigma^2}{8}\iint_S \mathrm{d}^2\vec{r}_1\frac{|J_{12}|^2}{R_{01}^2R_{12}^2}\times$$

$$\times\sum_{j=\pm}\left|\tilde{J}_{01}\left[k\left(\vec{\beta}_\perp-\vec{\alpha}_\perp\right)\right]\right|^2\tilde{W}_j\left[k\left(\vec{\beta}_\perp-\vec{\alpha}_\perp\right)\right]\delta[\Delta\omega-\omega_j], \tag{31}$$

where $\Delta\omega=\omega-\omega_0$ and $\omega_j=j\sqrt{gk\left|\vec{\beta}_\perp-\vec{\alpha}_\perp\right|}$, with $j=\pm$.

If the grazing angles for the paths $\vec{R}_{01}$ and $\vec{R}_{12}$ are much greater than the Brewster angle, then Eq. (31) goes over into the formula (1b) by Bass and Fuks [2] (see page 139).

As follows from Eq. (31), the spectrum is formed by certain points of scattering and lies around the frequency ω_0 within the frequency range

$$\Delta\omega=\pm\sqrt{gk\left|\vec{\beta}_\perp-\vec{\alpha}_\perp\right|_{\max}}. \tag{32}$$

In the most general case of an infinite scattering surface S the value of $\left|\vec{\beta}_\perp-\vec{\alpha}_\perp\right|$ for different scattering points varies within the interval

$$0\le\left|\vec{\beta}_\perp-\vec{\alpha}_\perp\right|\le 2. \tag{33}$$

If S is of a finite size, then the range of possible variations in $\left|\vec{\beta}_\perp-\vec{\alpha}_\perp\right|$ can be much smaller and is determined by the specific geometry of the problem. Strictly speaking the initial formula Eq. (1) in [1] has been derived under the assumption that the surface S represents an infinite plane. For this reason application of the results which follow from the expression, to a surface S of a finite size greater than the wavelength should be considered as a short-wave asymptotic for the boundary-value problem of the Helmholtz equation (see [5], Chapter 1).

Of special interest is the case of wave backscattering ($\vec{R}_{12}=-\vec{R}_{01}$ and $\vec{\beta}_\perp=-\vec{\alpha}_\perp$) when

$$\Delta\omega=\pm\sqrt{2gk|\vec{\alpha}_\perp|}. \tag{34}$$

It is evident that the scattering at a given frequency is provided by those points of the surface for which $|\vec{\alpha}_\perp|=\text{const}$ independently of the azimuthal angle. The range of possible variations of the angle of incidence determines the spectrum width.

In the absolutely degenerated case of grazing propagation ($z_0=0$) the angle of incidence (and scattering) is fixed and equals to $\pi/2$. Hence $|\vec{\alpha}_\perp|=1$ and all the points of scattering contribute at the same frequency shift, viz.

$$\Delta\omega=\pm\sqrt{2gk}. \tag{35}$$

In this case the argument of the function $\delta\left[\Delta\omega \pm \sqrt{2gk}\right]$ is independent of $\vec{r}_1$. Hence the function can be factored out from the integral in the formula which follows from Eq. (31) at $\vec{\beta}_\perp = -\vec{\alpha}_\perp$. The spectrum of field fluctuations in this case consists of two infinitesimally thin (as a result of the mathematical idealization admitted before) lines.

In all other cases the argument of the delta function is dependent on the scattering point $\vec{r}_1$ and hence factoring it out from the integral as has been done by Bass and Fuks [2] (see Eq. (2) on page 139) is inadmissible.

The effect of the phase front curvature of the incident and scattered fields is essential at the distances R_{01} and R_{12}, where the phase of $M(\vec{\rho})$ is much greater than unity. The spectrum Eq. (28) in this case is determined through double integration over points of the scattering surface and double integration over wave vectors of the spatial spectrum of the surface irregularities.

Taking the integral over the wave vectors is a rather difficult problem even in the particular case of the wave backscattering and will be not considered in the present paper. The same concerns the general case of an arbitrary geometry. This consideration can be a subject of a special investigation.

Thus the results of Parts I and II of the paper allow describing the near-field scattering of waves by rough surfaces in terms of both the wave field fluctuations and the mean intensity of the fluctuations and its frequency spectrum. Further analysis of these characteristics will contribute to a more detailed understanding the effects of wave scattering.

REFERENCES

1. Bryukhovetski, A. S., Near-field scattering of waves from a statistically rough surface: I. Field fluctuations, *Radiofizika i Radioastronomia*, 12(4):399-409, 2007 (in Russian).
2. Bass, F. G. and Fuks, I. M. Wave Scattering from Statistically Rough Surfaces. Moscow: Nauka; 1972 (in Russian).
3. Felsen, L. B. and Marcuvitz, N. Radiation and Scattering of Waves. Vol. 1. Moscow: Mir; 1978 (in Russian).
4. Monin, A. S. and Krasitski, V. P. Phenomena on the ocean surface. Leningrad: Gidrometeoizdat; 1985 (in Russian).
5. Kryukovski, A. S., Lukin, D. S., and Palkin, E. A. Edge and angular catastrophes in the problems of wave diffraction and propagation. Kazan: KAI; 1988 (in Russian).

Radio Physics and Radio Astronomy, 1(1), 57–61 (2010)

ARRAY ANTENNAS OF SIZE 8×8 BASED ON HADAMARD DIFFERENCE SETS

L. E. Kopilovich

A. Ya. Usikov Institute of Radio Physics and Electronics, NAS Ukraine, 12, Acad. Proskura St., Kharkiv, 61085, Ukraine

*Address all correspondence to L. E. Kopilovich E-mail:kopil@ire.kharkov.ua

The problem of synthesizing the optimized equi-amplitude array antenna (AA) on the 8×8 grid based on a Hadamard difference set is considered. By using newly found sets of this type on the 8×8 grid the 28- and 36-element AAs having a low sidelobe level are obtained.

A numerical experiment showed that by a small alteration of the structure of such a set, further reduction of the AA sidelobe radiation is possible.

KEY WORDS: *array antenna, synthezing, numerical experiment, difference sets, power pattern*

1. INTRODUCTION

The idea of using cyclic difference sets (DSs) for synthesizing aperiodic linear array antennas (AAs) with a low sidelobe level (SLL) was suggested in [1], and it was generalized to the 2-D case in [2]. Further investigation of this issue in both linear and planar cases was described in monograph [3]. In particular, there it was shown that the basic DS class appropriate for the construction of planar aperiodic AAs is that of Hadamard difference sets (*H* sets [4]).

It will be mentioned that one can build the *H* sets only on integer grids of definite sizes [5]. In each case there exist several inequivalent versions of such a set, where the number of the inequivalent *H* sets has a tendency to grow with the larger grid size. Each of these sets generates an ensemble of equivalent *H* sets, which can be obtained from the initial one by a definite procedure (see below); and after finding in each of the ensembles the set ensuring the minimum SLL for the AA, the best of them is then chosen.

The difficulty lies in the fact that now the complete collection of inequivalent *H* sets is built only for the grids of sizes 4×4, 6×6, and 3×12; as for the grids of larger sizes, little is known in this respect.

In the recent paper [6] several new inequivalent *H* sets on square $n\times n$ grids with $n = 8, 12, 16$ and 24 were obtained, and the corresponding AAs having the minimized SLL were synthesized. To further this line, the knowledge of new inequivalent *H* sets is required.

This paper continues investigation of the AAs based on *H* sets on the 8×8 grid. In this case, the number of the found inequivalent *H* sets is brought up to twenty that enables obtaining an AA with improved characteristics. Also, a numerical experiment to clarify the possibility of further reducing of the AA SLL when the structure of the underlying *H* set undergoes small alterations is carried out.

2. GENERAL INFORMATION ON *H* SETS

By definition [7], a *k*-element DS $\{(a_i, b_i)\}$ on an integer $\nu_x\times\nu_y$ grid is such a set that any nonzero node $(\overline{a}, \overline{b})$ of the grid has exactly Λ representations of the form

$$\bar{a} \equiv a_i - a_j \bmod \nu_x, \qquad \bar{b} \equiv b_i - b_j \bmod \nu_y,$$

where

$$\Lambda = k(k-1)/(V-1), \qquad V = \nu_x \cdot \nu_y. \tag{1}$$

An H set is a DS whose parameters satisfy the additial condition [8]

$$V = 4(k - \Lambda). \tag{2}$$

H sets exist on grids with [5]

$$\nu_x = 2^n, 3 \cdot 2^n, \qquad \nu_y = \nu_x, \qquad n \geq 1, \tag{3a}$$

and

$$\nu_x = 2^{n+1}, 3 \cdot 2^{n+1}, \qquad \nu_y = \nu_x/4, \qquad n \geq 1. \tag{3b}$$

(An H set on the $s \times t$ grid is equivalent to a perfect binary array PBA $(s \times t)$ [9] which represents a binary array of size $s \times t$ whose autocorrelation function remains constant with all cyclic shifts of its elements along the both grid sides [10]. Further, we make no distinction between an H set and the corresponding PBA.)

It follows from (1)–(3) that the element number of an H set is determined by parameter V:

$$k = \sqrt{V}\left(\sqrt{V} \pm 1\right)/2. \tag{4}$$

Note that with the "–" in (4) the fill factor of the array $\beta = k/V < 0.5$. The H set for which one "+" is taken in (4) is called complementary. Its elements are placed in all grid nodes empty from those of the first set, so its element number is $k_1 = \nu - k$.

For a square grid, $\nu_x = \nu_y = \nu$, and $k = \nu(\nu \pm 1)/2$. Thus, H sets with 28 and 36 elements can be build on the 8×8 grid.

It is known [7] that if there exists a DS with given parameters, then there also exists an ensemble of equivalent sets having the same parameter values; in the 2-D case, these sets are obtained from the initial one by a simultaneous cyclic shifting all its elements along the grid sides, and also by the grid automorphisms transforming it by the formulas

$$a_{i1} = c_{11} \cdot a_i + c_{12} \cdot b_i, \qquad b_{i1} = c_{21} \cdot a_i + c_{22} \cdot b_i, \tag{5}$$

with $c_{11}, c_{12}, c_{21}, c_{22}$ integers (a_{i1}, b_{i1} are then taken modulo ν_x, modulo ν_y, respectively), provided the determinant of the equation system (5)

$$\mathrm{Det} = c_{11} \cdot c_{22} - c_{21} \cdot c_{12}$$

is a number co-prime with the grid sidelengths [11].

In all known cases the 2-D H sets exist in a number of inequivalent versions unobtainable one from another by the described procedure. Each of such sets possesses its own ensemble of the equivalent ones, so the total number of H sets with given parameters is proportional to that of the inequivalent sets.

3. NEW INEQUIVALENT *H* SETS ON THE 8×8 GRID

For the 8×8 grid, two inequivalent H sets are given in [12] and [13], and three more – in [6]. To our knowledge, no more inequivalent H sets are given in the literature.

Here, we found 15 new inequivalent H sets. Several such sets are obtained by using the formula [14]

$$w_{2i+r,j} = u_{i,2j+r},$$

where $0 \leq i \leq s$, $0 \leq j < t$, $0 \leq r \leq 1$, $U = (u_{ij})$ is a PBA of size $s \times (2t)$, and $W = (w_{ij})$ is an array of size $(2s) \times t$. Under specific conditions, W is also a PBA. The fulfilment of these conditions is difficult to check, however, one can make sure by direct verification that in our case (at $s = 4$, $t = 8$), W is an H set on the 8×8 grid. This allows to obtain H sets on this grid by using the known H sets on the 4×16 grid, and choose the inequivalent ones among them. As a main source for obtaining H sets on the 8×8 grid by this method a wealth of H sets on the 4×16 grid given in [15] was used; so, 8 new inequivalent H sets were found. Besides, one such set was obtained from [12] in this way.

One more method consists in transforming an H set $\{(a_i, b_i)\}$ into the set $\{(a_{i1}, b_{i1})\}$ on the grid of the same

size following the rule: if sum $a_i + b_i$ is an even number then $a_{i1} = a_i$, $b_{i1} = b_i$, whereas in the opposite case its odd component decreases by 1 and its even component increases by 1 (thus, in all cases, $a_{i1} + b_{i1} = a_i + b_i$). As the result, an H set is again obtained, and among the sets obtained in such a way 6 new inequivalent ones occured.

The found collection of the inequivalent H sets is probably still incomplete, however, by using these sets the AAs having lower SLL than those obtained earlier were synthesized.

4. SEARCHING PROCEDURE FOR THE AA WITH MINIMIZED SLL

The normalized power pattern of a planar equiamplitude AA is

$$F(q_x, q_y) = \left| \frac{1}{k} \sum_{j=1}^{k} \exp\left[i(a_j \cdot q_x + b_j \cdot q_y) \right] \right|^2, \qquad (6)$$

where a_j, b_j are now co-ordinates of an array element, q_x and q_y are the generalized space coordinates: $q_x = 2\pi d(l - l_0)/\lambda$, $q_y = 2\pi d(m - m_0)/\lambda$; d is the distance between the adjacent nodes in an array row or column; λ is the wavelength; l, m are the cosines of the angles between the beam and the axes x and y; and (l_0, m_0) is the direction towards which the beam is pointed. In what follows, pattern (6) is optimized on the domain $(-\pi \le q_x \le \pi, \quad 0 \le q_y \le \pi)$, therefore, the results obtained are valid for any values of d/λ and l_0, m_0; without losing generality, one can take $d = \lambda/2$ and $l_0 = m_0 = 0$.

When set $\{(a_j, b_j)\}$ represents a DS, function (6) takes the constant value $F_c = (k - \lambda)/k^2$ over the net of space points $\{(2\pi s/\nu, 2\pi t/\nu)\}$, $s + t \ge 0$ [4]. Therefore, we may expect that for a square AA, F takes its maximum value near a point of the net

$$\{(s\pi/\nu, t\pi/\nu)\}; \qquad s = -(\nu - 1), ..., -1, 0, 1, ..., \nu - 1; \qquad (7)$$

under the conditions

$$\mathrm{Abs}(s) > 2 \quad \text{or} \quad t > 2; \ (s \cdot t) \bmod 4 > 0, \qquad (8)$$

first of which means that only the sidelobe region is considered, and the second one – that the points at which $F = F_c$ are excluded.

The calculation was described in [6]; briefly, it is as follows. An H set for which the quantity $Fm = \max F$ (dB) over the space points net (7) does not exceed some given M is found; then the value of Fm over the net of double thickness is found, and so on. The process of double thickening continues until the magnitude of Fm is stabilized, coming to a certain quantity F_0.

Further, an H set giving a value of Fm over net (7), (8) which is less than that for the initial set is searched for, and the described procedure giving now a new value of F_0 is repeated; if this value is smaller than the preceding one, such set is stored, and so on.

Note that a smaller value of Fm does not inevitably lead to a smaller value of F_0; therefore, to diminish the probability of omitting the real minimum value of the latter over the whole considered ensemble of H sets, the described process was periodically repeated, beginning in each case from a new H set of the ensemble.

The calculation was carried out through the ensembles corresponding to all known inequivalent H sets on the 8×8 grid. As the result, the 28-element AA having the SLL –12.59 dB, and the 36-element AA with the SLL –13.86 dB were synthesized. The power patterns of these AAs, together with the schemes of their element arrangement are given in Figs. 1 and 2.

5. ON THE POSSIBILITY OF FURTHER SLL REDUCTION

Recently, the so called genetic algorithms were applied to the synthesis of linear AAs in a number of papers, including those where cyclic DSs as initial ones were taken [16]. In some cases, one can pass from a linear grid to a rectangular one having coprime sidelengths, thus obtaining a planar AA.

In this way, it is impossible to obtain a square AA. However, in this case one can search for an AA with a still smaller SLL by slightly altering the underlying H set, e.g., by shifting a few of its elements from their places to other grid nodes, and then calculating through the ensemble of sets obtainable from such a set by the same described procedure.

We made a numerical experiment using inequivalent H sets having a structure of the form shown in Fig. 3. Here, in three rows of the grid there are two set ele-

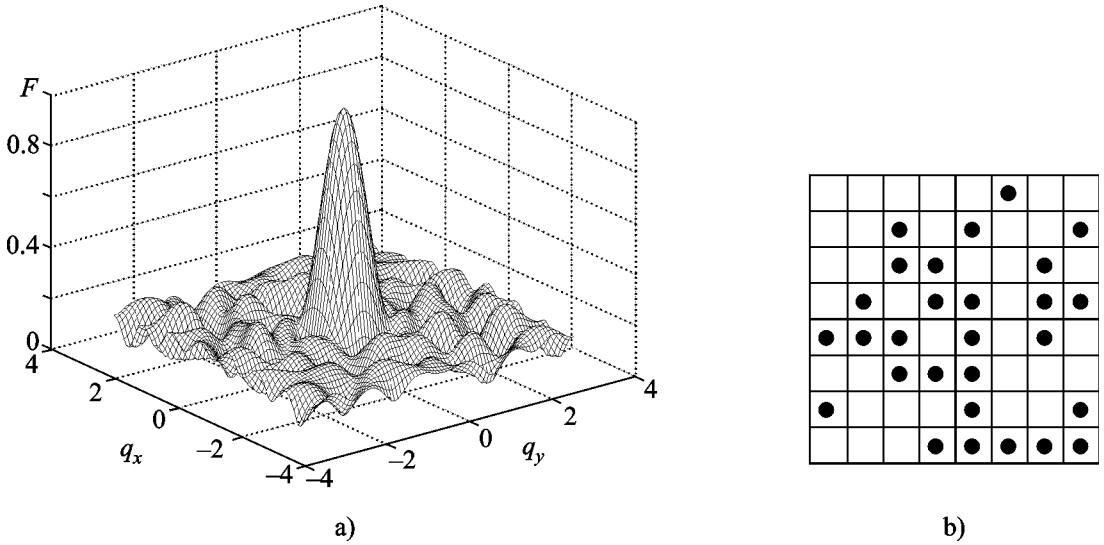

FIG. 1: The power pattern of the optimized 28-element AA (a), and the scheme of its element arrangement (b)

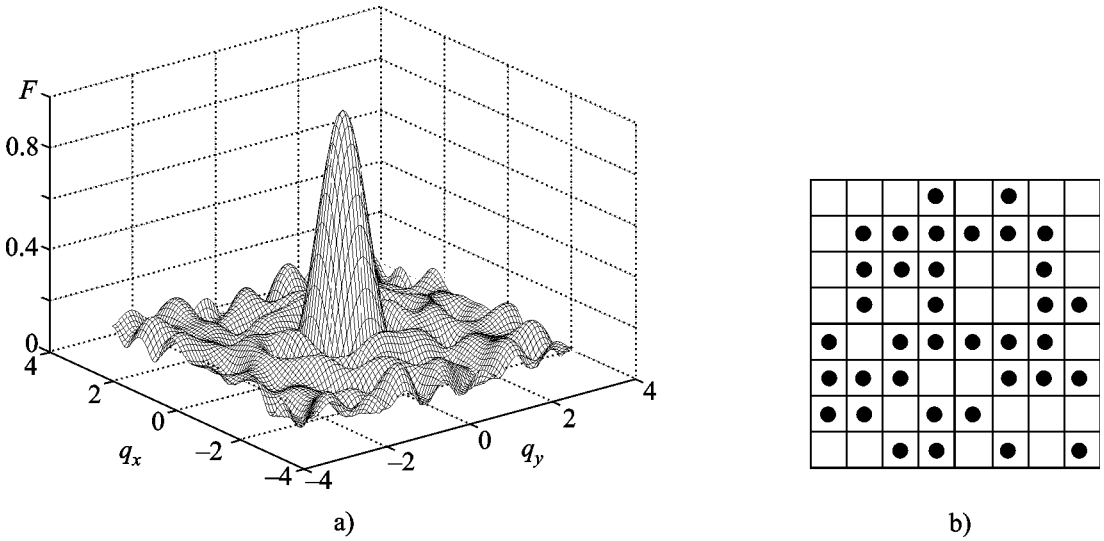

FIG. 2: The power pattern of the optimized 36-element AA (a), and the scheme of its element arrangement (b)

ments, six elements in one row and four elements in each of the rest rows. While making by turns all possible element shifting in the rows containing only two elements of the set, one obtains, in each case, a "disturbed" H set, and when taking this set and that complementary to it as the initial ones, we obtain, by using the aforesaid procedure, the ensembles of 28- and 36-element sets.

The calculation through these set ensembles has shown that in this way the AAs with smaller SLLs can be synthesized. As an example, a "disturbed" 36-element set ensuring the SLL –14.43 dB is shown in Fig. 4.

6. CONCLUSION

The collection of the inequivalent H sets found also allows obtaining optimized AAs of larger sizes. Thus, by the method suggested in [14, 15] and somewhat simpli-

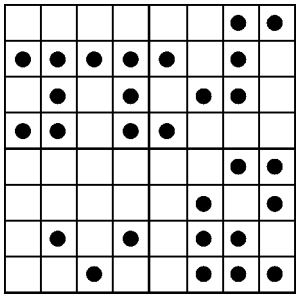

FIG. 3: The scheme of the element arrangement in the *H* sets used in the numerical experiment

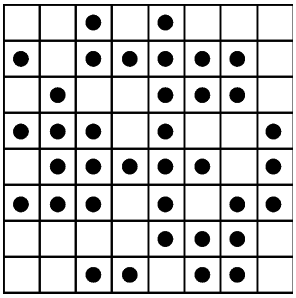

FIG. 4: The 36-element "disturbed" *H* set ensuring the reduced SLL of –14.43 dB

fied in [3], when having an *H* set on the $s \times t$ grid, one can obtain the *H* set on the $(2s) \times (2t)$ grid. In this way the *H* sets on the 16×16 grid can be built, and on their base the AAs with a large number (120 and 136) of elements having a low SLL synthesized, that becomes pressing in the development of modern radio telescopes [17].

REFERENCES

1. Leeper, D. G., inventor; Thinned periodic antenna arrays with improved peak sidelobe level control, United States patent 4071848. 1978 Jan 31.
2. Kopilovich, L. E. and Sodin, L. G., Two-dimensional aperiodic antenna arrays with a low sidelobe level, *IEE Proc., pt. H*, 138(3):233-237, 1991.
3. Kopilovich, L. E. and Sodin, L. G. Multielement, G. System Design in Astronomy and Radio Science. Dordrecht/ Boston/ London: Kluwer Academic Publishers, Astrophysics and Space Science Library vol. 268, 2001, 190 p.
4. Turyn, R. J., Character sums and difference sets, *Pacific J. Math*., 15(1):319-346, 1965.
5. Wild, P., Infinite families of perfect binary arrays, *Electron. Lett*., 24(14):845-847, 1988.
6. Kopilovich, L. E., Square array antennas based on Hadamard difference sets, *IEEE Trans. Antennas Propag.,* AP-56:263-266, Jan. 2008.
7. Hall Jun, M. Combinatorial Theory. 2nd ed. New York: Wiley; 1986.
8. Menon, P. K., On difference sets whose parameters satisfy a certain relation, *Proc. Am. Math. Soc*., 13(5):739-745, 1962.
9. Chan, Y. K., Siu, M. K., and Tong, P., Two-dimensional binary arrays with good autocorrelation, *Information and Control*, 42:125-130, 1979.
10. Calabro, D. and Wolf, J. K., On the synthesis of two-dimensional arrays with desirable correlation properties, *Information and Control*, 11:537-560, 1968.
11. Kurosh, A. G., Theory of Groups. New York: Chelsea; 1958.
12. Jungnickel, D. and Pott, A. Abelian difference sets. In: Colbourn, Ch. D. and Dinitz, J. H., editors. The CRC Handbook of Combinatorial Designs. Roca Baton: CRC Press; 1996, p. 15-64.
13. Bömer, L. and Antweiler, M., Two-dimensional perfect binary arrays with 64 elements, *IEEE Trans. Inf. Theory*, IT-36(2):411-414, 1990.
14. Jedwab, J. and Mitchell, C., Constructing new perfect binary arrays," *Electron. Lett*, 24(11):650-652, 1988.
15. Arasu, K. T. and Reis, J. On Abelian group of order 64 that have difference sets. Tech. report. Dept of Math. and Stat. of Wright State University, Dayton; 1987 Okt. Tech. Rep. No.: 1987.10.
16. Caorsi, S., Lommi, A., Massa, A., and Pastorino, M., Peak sidelobe level reduction with a hybrid approach based on GAs and difference sets, *IEEE Trans. Antennas Propag.*, 52:1116-1121, Apr. 2004.
17. Kogan, L., Optimizing a large array configuration to minimize the sidelobes, *IEEE Trans. Antennas Propag*, 48:1075-1078, July 2000.

Radio Physics and Radio Astronomy, 1(1), 63–67 (2010)

EMPIRICAL ESTIMATE FOR THE MAXIMUM ELEMENT NUMBER OF A NONREDUNDANT CONFIGURATION ON SQUARE ARRAY ANTENNA

L. E. Kopilovich

O. Ya. Usikov Institute for Radiophysics and Electronics of NAS of Ukraine, 12, Acad. Proskury St., Kharkiv, 61085, Ukraine

*Address all correspondence to L. E. Kopilovich E-mail:kopil@ire.kharkov.ua

The maximum number of elements of a nonredundant configuration on a square array antenna is estimated empirically employing the investigated structure of differences between the elements of the configuration mapping onto the scan.

KEY WORDS: *array antenna, nonredundant configuration, analysis*

1. INTRODUCTION

The problem of constructing a nonredundant configuration (NRC) of elements is of urgent necessity for radio interferometry. Here, a momentous problem is how to build the NRC with the maximum number of elements to obtain the maximum number of interferometer baselines. Such NRCs on square $n \times n$ grids (so called "Golomb squares" [1]) with the maximum possible elements are found at $n \le 22$ in a number of papers [1-7]. At the same time, the size of modern array antenna, as well as the number of its elements, can substantially exceed these values [8] that requires the elaboration of methods for building NRCs on large grids.

Such NRCs were obtained in [4] with using combinatorial constructions – cyclic difference sets (see also [9]). However, it remains unclarified to what degree the element number of the NRC thus found is close to a maximum.

The rigorous estimates for the NRC element number on a square grid were obtained in [1, 3], however, the former is too overrated, while for applying the latter the information on NRCs on linear grids of large lengths, unavailable to date, is required. In this connection, the obtainment of the upper estimate based on available empirical data is of interest.

2. ANALYSIS OF THE MAPPING STRUCTURE OF THE NRC ON THE SQUARE GRID SCAN

Consider an arbitrary k-element NRC on the $n \times n$ grid and analyze the system of vector differences between its elements (see Fig. 1). Number the cells of the first grid row from 1 to n, of the second one – from $n+1$ to $2n$, and so on. The vector connecting the cells can be pointed rightwards or strictly downwards (type I), or leftwards (type II). When scanning the grid, the NRC on it passes to a point system on the segment, and the differences between these points can be either one-fold (i.e. non-repeated) or two-fold ones. Obviously, vector differences on a 2-D grid belonging to the same type cannot pass to equal differences on the scan, while only some part of these belonging to the opposite types passes to the equal

ISSN 2152-274X

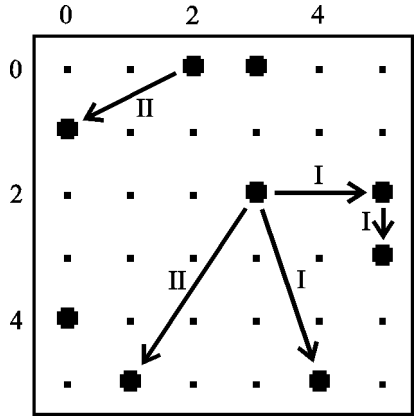

FIG. 1: An example of a nonredundant configuration (NRC) on the square grid. The NRC elements are denoted with bold dots. The vectors connecting the elements are pointed rigthwards or strictly downwards (type I) or leftwards (type II)

ones. Thus, the share of the one-fold differences on the scan can be expected to exceed half of their total number $K = k(k-1)/2$. Besides, it should be taken into account that the NRC placed on a square grid, the latter being rotated through 90°, would give an alternative point system on the scan (see Fig. 2). In addition, for most of n values, at least, several different NRCs with a maximum number of elements can be built [7]. This allows suggestion that for almost all values of n a maximum-element NRC on the $n \times n$ grid can be built for which the share (α) of the non-repeated differences on the scan exceeds 50 % of their total number,

$$\alpha > 50\ \%. \qquad (1)$$

These qualitative considerations were verified by using the available data. The $n \times n$ grids at $3 \le n \le 22$ with the NRCs found in [4, 6, 7] placed on them were scanned in two variants (as in Fig. 2), and it was found out that for all n in this range, except for $n = 7$, this suggestion was validated at least in one of such variants (see Table 1).

Now we will seek the upper estimate for the NRC element number under the assumption that for $n > 7$ a maximum-element NRC can be found for which condition (1) is fulfilled.

3. UPPER ESTIMATE OF THE NRC ELEMENT NUMBER

Consider a k-element NRC placed on the $n \times n$ grid. When scanning the grid, the NRC elements pass to a point sequence

$$a_1 < a_2 < \ldots < a_k \qquad (2)$$

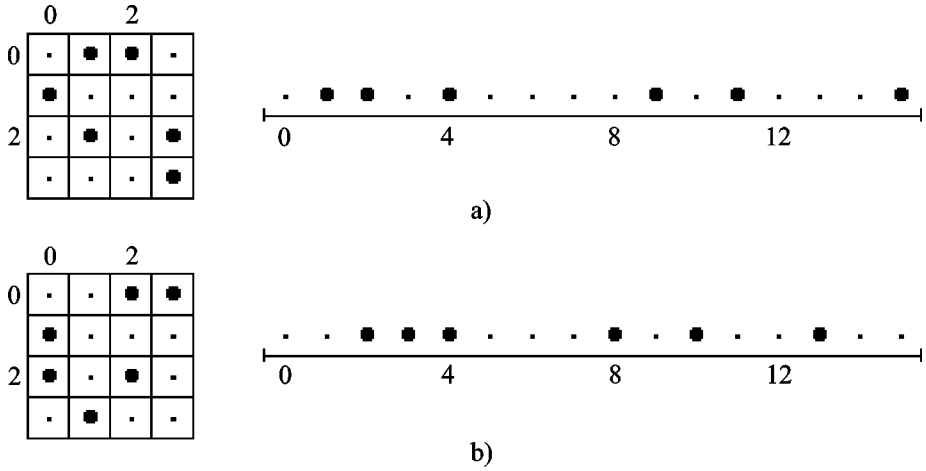

FIG. 2: A grid with an NRC placed on it, and its scan (a). The same grid rotated through 90°, and its scan (b). The share of non-repeated differences between the points on the scan is denoted with α (%)

Table 1: The characteristics of the maximum-element NRCs and point sequences obtained from them when scanning the location grids. Here, n is the grid sidelength, k is the number of the NRC elements, m is the number of non-repeated differences between points on the scan, and α is their share in the total number of differences equal to $K = k(k-1)/2$

n	k	m	K	a (%)
3	5	6	10	60.0
4	6	11	15	73.3
5	8	16	28	57.4
6	9	24	36	66.7
7	11	27	55	49.1
8	12	34	66	51.5
9	13	45	78	56.7
10	15	53	105	50.5
11	16	64	120	53.3
12	17	82	136	60.3
13	18	87	153	56.9
14	19	101	171	59.1
15	21	112	210	53.3
16	22	125	231	54.1
17	23	149	253	58.9
18	24	168	276	60.9
19	25	184	300	61.3
20	26	198	325	60.9
22	29	244	406	60.1

on the scan.

Here, we apply the approach suggested for the linear case [10]. The order of differences between elements a_j and a_i of sequence (2), $j > i$, is the difference $j - i$, at this point, the sum of differences of the first order is

$$(a_2 - a_1) + ... + (a_k - a_{k-1}) < n^2,$$

and similarly, the sum of differences of order ν is

$$(a_{\nu+1} - a_1) + ... + (a_k - a_{k-\nu}) < \nu n^2.$$

It follows that the sum of differences of orders up to t is

$$S_t < n^2 t(t+1)/2. \quad (3)$$

On the other hand, the number of these differences is

$$(k-1) + ... + (k-t) = kt - t(t+1)/2 = ts, \quad (4)$$

where $s = k - (t+1)/2,\ 1 \le t \le k.$

Should the differences between the elements on the scan be all distinct then one might write

$$S_t \ge 1 + ... + ts,$$

and comparing the last inequality with (3) find the estimate of the maximum element number. Virtually, in such a way the estimate for the maximum element number of an NRC on a linear grid can be obtained [10].

In our case, some part of differences on the scan are two-fold, but using condition (1) and with the Eq. (4) considered, we may write

$$S_t \ge 2\left(1 + ... + [ts/4]\right) + \left([ts/4] + 1\right) + ... + [3ts/4], \quad (5)$$

where $[c]$ means integer part of c. If one writes $ts = 4r + \beta$, with the r integer and $\beta = 0, 1, 2$ or 3, inequality (5) can be rewritten in the form

$$S_t \ge 2(1 + ... + r) + (r+1) + ... + (4r + \beta - r).$$

When performing here the summation operations and returning again to the ts one obtains

$$S_t \ge \frac{5}{16}(ts)^2 + \left(\frac{\beta}{8} + \frac{1}{2}\right)ts + \frac{1}{16}\beta^2 > \frac{5}{16}(ts)^2.$$

Further, one correlates the last inequality with (3) and obtains:

$$\frac{5}{16}(ts)^2 < \frac{t(t+1)n^2}{2},$$

whence

$$s < nb\sqrt{1+1/t} \cong nb\left(1+1/(2t)\right),$$

with $b = \sqrt{8/5} = 1.265,$
and

$$k < (t+1)/2 + nb\left(1+1/(2t)\right) = f(t).$$

Function $f(t)$ has its minimum at $t = \sqrt{nb},$ thus

$$k < 1.265n + 1.124\sqrt{n} + 0.5 \qquad (6)$$

or $k \le k_e,$ where k_e is the integer part of the expression in the right-hand side of (6).

4. RESULTS

Table 2 shows the maximal found element numbers of NRCs placed on $n \times n$ grids at $n > 7$ taken from [7], in comparison with their estimates as obtained by (6) and those known from literature. It can be seen that the values of k_e are smaller than the estimates given in [1]; as for the estimates in [3], obtained only for $n \le 11,$ in this range they roughly equal to ours.

As is seen from Table 2, there is a "reserve" kept in the discrepancy between k_e and the corresponding value of k. Apparently, owing to this estimate (6) is valid also for the case of a possible value of n when condition (1) is not fulfilled.

The comparison of the estimates for large arrays given by (6) with the results obtained in [4] (see Table 3) shows that the number of NRC elements given by the suggested method, though not maximum, is nevertheless wholly acceptable for feasible purposes.

5. CONCLUSION

The upper estimate obtained for the element number of an NRC on a square grid is more efficient than those earlier known. It can serve a guiding line when building a large size array antenna with the maximum NRC element number.

Table 2: The estimates of the maximum number of the NRC elements on square grids. Here, n and k are the same as in Fig. 1, k_e is estimated with (6), k_r and k_{r1} are the estimates of k taken from [1] and [3], respectively

n	k	k_e	k_r	k_{r1}
8	12	13	13	13
9	13	15	15	14
10	15	16	17	16
11	16	18	19	18
12	17	19	21	–
13	18	21	23	–
14	19	22	25	–
15	21	23	27	–
16	22	25	28	–
17	23	26	29	–
18	24	28	31	–
19	25	29	33	–
20	26	30	34	–
21	27	32	–	–
22	29	33	–	–

Table 3: The element numbers in the NRCs on large grids [6], and their estimates with (6)

n	k	k_e
25	30	37
30	35	44
40	47	58
50	58	71

REFERENCES

1. Robinson, J. P., Golomb rectangles, *IEEE Trans*, IT-31(6):781-787, 1985.
2. Shearer, J. B., Some new Golomb rectangles, *Electron. J. Comb.*, 2(R12), 1995.
3. Robinson, J. P., Golomb rectangles as folded rulers, *IEEE Trans*, IT-43(1):290-293, 1997.

4. Kopilovich, L. E., Nonredundant apertures for optical interferometric systems: maximization of the number of elements, *J. Mod. Opt.*, 45(11):2417-2424, 1998.
5. Robinson, J. P., Genetic search for Golomb arrays, *IEEE Trans*, IT-46(6):781-787, 2000.
6. Kornienko, Yu. V., Construction of nonredundant antenna configurations on square grids by a random search technique, *Telecommunications and Radio Engineering*, 57(2&3):23-30, 2002.
7. Shearer, J. B., Symmetric Golomb squares, *IEEE Trans*, IT-50(8):1846-1847, 2004.
8. Schultz, R., Radio astronomy antennas by the Thousands, *Experimental Astronomy*, 17:119-139, 2004.
9. Kopilovich, L. E., and Sodin, L. G. Multielement System Design in Astronomy and Radio Science. Vol. 268. Dordrecht/Boston/London: Kluwer Academic Publishers, Astrophysics and Space Science Library; 2001, 190 p.
10. Lindström, B., On inequality for B-sequences, *J. Combin. Theory*, A6(2):211-212, 1969.

Radio Physics and Radio Astronomy, 1(1), 69–77 (2010)

RADIATION DIFFUSE SCATTERING BY A DENSELY PACKED LAYER OF SPHERICAL PARTICLES

V. P. Tishkovets

Institute of Radio Astronomy, National Academy of Sciences of Ukraine, 4, Chervonopraporna St., Kharkiv, 61002, Ukraine

*Address all correspondence to V. P. Tishkovets E-mail:tishkovets@ri.kharkov.ua

A vector equation to describe the radiation diffuse scattering by a random densely packed medium of similar spherical particles has been obtained. The medium is a statistically homogeneous, plane parallel layer illuminated by an oblique plane electromagnetic wave. The assemble averaging of the relationships for the elements of the radiation reflection matrix is due to the quasi-crystalline approximation. The obtained equation takes into complete account the wave nonuniformities near the scatterers. In the limiting case of sparse medium, the equation turns into the classical vector radiative transfer equation.

KEY WORDS: *diffuse scattering, spherical particles, statistically homogeneous, quasi-crystalline approximation, vector, equation, nonuniformities*

1. INTRODUCTION

Effects of electromagnetic wave scattering and absorption are widely exploited in science and technology to realize remote sensing of objects and quality control of materials. The interpretation of radar, optical and other information from the remote sensing of objects calls for sufficiently reliable theory of wave scattering by various media. In this connection, of particular interest are theoretical models of electromagnetic wave scattering by discrete media with a scatterer size of the wavelength order, in which case the scattered radiation characteristics are most sensitive to wavelength variations. The theoretical treatment of the radiation scattered by the materials of the nature is a challenge because a great number of effects not occurring in sparse media must be taken into account. In particular, the correlation between the particles complicates the assemble averaging of the scattering characteristics [1, 2].

In sparse media, the particle spacing much exceeds the radiation wavelength and the particle size. In this case, all medium scatterers are in the far zones of one another, which means that the wave coming to a scatterer from another one is spherical and can be modeled, by virtue of large distances between the particles, by a uniform plane wave [3-5]. On this basis, the medium multiple scattering can be handled using such instruments of the well developed theory of single scattering [4, 6] as scattering matrix, extinction cross section, scattering and absorption.

In dense media, the wave coming from a scatterer to its nearest neighbor is a nonuniform one [7, 8]. Besides, for describing the sparse medium scattering, we have right to restrict ourselves to only the ladder and cyclic diagram summation in the diagram representation of the Bethe-Salpeter equation [4, 9]. In the dense medium case, some more diagrams must be taken into account, such as those corresponding to the interference of waves scattered by neighboring scatterers or the waves with different scattering orders [2, 10]. All these complicate noticeably the theoretical treatment of the scattering by dense media.

To alleviate the above-mentioned difficulties, works [2, 11, 12] suggest employing the classical vector transfer equation. In it, the radiation attenuation coefficient and the scattering characteristics are adapted to the

ISSN 2152-274X

so-called elementary volume in the dense medium case. Yet the transfer equation, considering its derivation from Maxwell's equations, is valid when the medium scatterers are far apart from one another. Hence it is true for sparse media [3-5], and the results from this approach may happen to be unreliable. Another way [10] calls for deriving the relevant equations for the sums of all diagrams contributing significantly to the scattered radiation. It is not efficient for media of small-size particles because a large number of different type diagrams must be taken into account. When the scatterer size is of the wavelength order and larger, not many diagram types contribute clearly to the scattered radiation. In particular, one of the main contributions corresponds to the ladder diagram summation characterizing the noncoherent (diffuse) part of the scattered radiation. In the sparse medium case, this summation is governed by the classical radiative transfer equation [3-5]. In [10], the relevant equation was obtained for the sum of these diagrams in the case of a densely packed medium of similar spherical scatterers. The medium was assumed to be a semi-infinite layer, the incident radiation was normal to the medium surface. Examples of the numerical solution of this equation for a medium scatterer comparable in size with the radiation wavelength showed that the field nonuniformities about the scatterers exerted a fairly large effect on the reflection matrix elements. The effect was pronounced even for not too densely packed scatterers. The role of the field nonuniformities in the forming of the scattered radiation has yet to be studied. Hence the development of theoretical methods to describe the electromagnetic wave scattering by densely packed media is very important. The present paper seeks to extend the equation obtained in [10] to the case of a finitely thick medium layer and oblique wave incidence. As in [10], the medium is assumed to be statistically uniform and isotropic and consisting of similar spherical scatterers.

2. ESSENTIAL RELATIONSHIPS IN ELECTROMAGNETIC WAVE SCATTERING THEORY FOR SETS OF SCATTERERS

The theory of scattering by a set of spherical particles (see, e.g. [4]) will form the basis of the transfer equation derivation. The notations were chosen for consistency with that of works [10, 13].

The coordinate systems required for the transfer equation derivation are given in Fig. 1. Let us consider the scattering of radiation by a medium layer of geometrical thickness Z_0. The upper boundary of the layer coincides with the plane x_0y_0 of the coordinate system $(x_0y_0z_0)$ whose axis z_0 is given by unit vector $\mathbf{n}_0$ and directed inward the material. This coordinate system is symbolized by $\hat{\mathbf{n}}_0$. The jth particle is located by the radius-vector $\mathbf{R}_j$ $(j = 1, ..., \tilde{N},$ where $\tilde{N}$ is the number of particles in the layer, $\tilde{N} \gg 1)$. The incident plane wave is given in the coordinate system $\hat{\mathbf{k}}_0$ with the z axis directed along the wave vector $\mathbf{k}_0$ $(k_0 = 2\pi/\lambda,$ and λ is the wavelength). The scattered radiation is described in the coordinate system $\hat{\mathbf{k}}_{sc}$ with the axis z_{sc} aligned with the wave vector $\mathbf{k}_{sc}$ $(k_{sc} = k_0)$. The rotation of the coordinate system $\hat{\mathbf{n}}_0$ to the system $\hat{\mathbf{k}}_0$ is defined by the Eulerian angles φ_0, ϑ_0, γ_0, and the $\hat{\mathbf{n}}_0$ to $\hat{\mathbf{k}}_{sc}$ rotation is given by the angles φ, ϑ, γ.

The electromagnetic wave scattering is convenient to describe in a circular wave basis (the so-called SP-representation). In it, an incident circularly polarized plane wave can be expressed in the form [4, 14]

$$\mathbf{E}_n^{(0)} = E_n^{(0)} \mathbf{e}_n(\hat{\mathbf{k}}_0) \exp(i\mathbf{k}_0\mathbf{r}), \qquad (1)$$

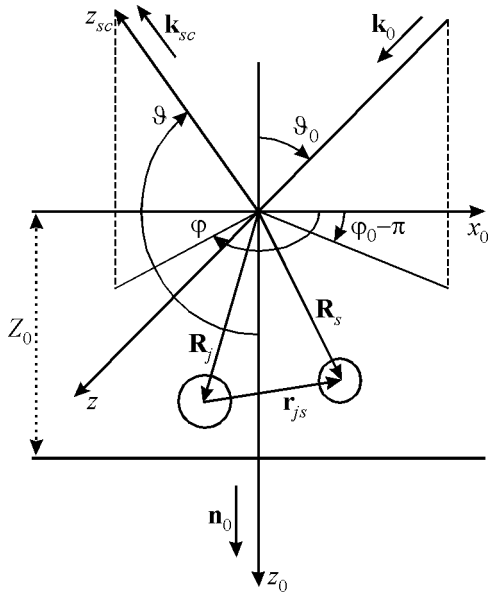

FIG. 1: The medium layer radiation scattering geometry

where $n=\pm 1$, $E_n^{(0)}$ is the wave amplitude, $\mathbf{e}_n(\hat{\mathbf{k}}_0)$ is the covariant cyclic unit vector [15] in the coordinate system $\hat{\mathbf{k}}_0$. Throughout the paper the time dependence $\exp(-i\omega t)$ is always omitted. For $n=1$, the sense of rotation of wave electric vector (1) is that of a right-handed screw when looking in the direction of wave vector $\mathbf{k}_0$, and of a left-handed screw for $n=-1$.

The field scattered by the medium can be written as

$$\mathbf{E}=\sum_j \mathbf{E}^{(j)}, \tag{2}$$

where $\mathbf{E}^{(j)}$ is the field scattered by the jth particle. The scattered amplitude matrix T_{pn} $(p, n=\pm 1)$ of the medium can be defined as [4]

$$\begin{pmatrix} E_1 \\ E_{-1} \end{pmatrix} = \frac{\exp(ik_0 r)}{-ik_0 r} \begin{pmatrix} T_{11} & T_{1-1} \\ T_{-11} & T_{-1-1} \end{pmatrix} \begin{pmatrix} E_1^{(0)} \\ E_{-1}^{(0)} \end{pmatrix}. \tag{3}$$

Here r is the distance from the origin of the coordinate system $\hat{\mathbf{n}}_0$ to the observation point.

Matrix (3) relates the vector components of the incident and the scattered waves given in different coordinate systems. At the oblique incidence on the medium layer, the polarization state of the incident radiation is convenient to determine in the plane produced by the vectors $\mathbf{n}_0$ and $\mathbf{k}_0$. For the scattered radiation, the corresponding plane is that given by the vectors $\mathbf{n}_0$ and $\mathbf{k}_{sc}$ [4]. Hereinafter it will be assumed that matrix (3) relates the vector components given in these planes.

According to (2), the components of the scattering amplitude matrix are

$$T_{pn}=\sum_j t_{pn}^{(j)},$$

where $t_{pn}^{(j)}$ is the scattered amplitude matrix of the jth particle [4].

The scattering matrix translating the Stokes parameters of the incident wave into the Stokes parameters of the scattered wave is established by the relationship [4, 10-13]

$$S_{pn\mu\nu}=\left\langle \sum_j t_{pn}^{(j)} t_{\mu\nu}^{*(j)} \right\rangle + \left\langle \sum_{j,s\neq j} t_{pn}^{(j)} t_{\mu\nu}^{*(s)} \right\rangle, \tag{4}$$

where the angle brackets indicate the assemble averaging, $\mu,\nu=\pm 1$. The first term on the right-hand side of this equation corresponds to the noncoherent (diffuse) component and the interference component produced by the interference of waves traveling along some looped trajectories in the medium [5]. The second term corresponds to the interference of waves, including the one demonstrating itself in the phenomenon of backscattering coherent amplification [5, 9, 13]. Here, only the noncoherent component will be considered.

To find $t_{pn}^{(j)}$, refer to the theory of radiation scattering by systems of spherical particles (see, e.g. [4]). Then the field $\mathbf{E}^{(j)}$ can be expressed as [10, 13]

$$\mathbf{E}^{(j)}=\frac{\exp(ik_0 r_j)}{-ik_0 r_j}\times$$

$$\times\sum_{L=1}^{\infty}\sum_{M=-L}^{L}\sum_{p=\pm 1}\frac{2L+1}{2}A_{LM}^{(jpn)}D_{Mp}^{*L}(\hat{\mathbf{n}}_0,\hat{\mathbf{k}}_{sc})\mathbf{e}_p(\hat{\mathbf{k}}_{sc}). \tag{5}$$

Here r_j is the distance from the jth particle to the observation point, $\mathbf{e}_p(\hat{\mathbf{k}}_{sc})$ is the cyclic unit vector [15] in the coordinate system $\hat{\mathbf{k}}_{sc}$ $(p=\pm 1)$, and $D_{Mp}^{L}(\hat{\mathbf{n}}_0,\hat{\mathbf{k}}_{sc})=D_{Mp}^{L}(\varphi,\vartheta,\gamma)$ is the Wigner function [15] governing the rotation from the coordinate system $\hat{\mathbf{n}}_0$ to the system $\hat{\mathbf{k}}_{sc}$. The scattering directions are assumed to be the same for all the particles.

The coefficients $A_{LM}^{(jpn)}$ come from the system of equations [10, 13]

$$A_{LM}^{(jpn)}=a_L^{(pn)}\exp(i\mathbf{k}_0\mathbf{R}_j)D_{Mn}^{L}(\hat{\mathbf{n}}_0,\hat{\mathbf{k}}_0)+$$

$$+\sum_q a_L^{(pq)}\sum_{s\neq j}\sum_{l,m}A_{lm}^{(sqn)}H_{LMlm}^{(q)}(\hat{\mathbf{n}}_0,\hat{\mathbf{r}}_{js}). \tag{6}$$

Here $q=\pm 1$, $a_L^{(pn)}=a_L+pnb_L$, a_L, b_L are the Mie coefficients [4]. When L is of the order of the parameter $\tilde{x}_0=k_0\tilde{a}$, and over, where $\tilde{a}$ is the particle radius, these coefficients tend to vanish rapidly. This establishes the order of equation system (6) and the upper values of the indices in (5). The symbols $H_{LMlm}^{(q)}(\hat{\mathbf{n}}_0,\hat{\mathbf{r}}_{js})$ represent the coefficients of the addition theorems for the Helmholtz vector harmonics [16, 17]

$$H_{LMlm}^{(q)}(\hat{\mathbf{n}}_0,\hat{\mathbf{r}}_{js})=\frac{2l+1}{2}(-1)^m\times$$

$$\times\sum_{l_1,m_1} i^{-l_1}h_{l_1}(k_0 r_{js})D_{m_1 0}^{l_1}(\hat{\mathbf{n}}_0,\hat{\mathbf{r}}_{js})C_{LMl-m}^{l_1 m_1}C_{Lql-q}^{l_1 0}, \tag{7}$$

where $\hat{\mathbf{r}}_{js}$ is the coordinate system whose axis z_{js} is aligned with the radius-vector of the *s*th particle in the *j*th particle coordinate system (the axes of the coordinate system related to the center of the *j*th particle are parallel to the axes of the coordinate system $\hat{\mathbf{n}}_0$), $h_{l_1}(k_0 r_{js})$ is the spherical Hankel function, symbol *C* stands for the Clebsch–Gordan coefficients [15]. The Clebsch–Gordan coefficients are other than zero provided that $m_1 = M - m$ and $|L - l| \le l_1 \le L + l$ [15]. This property of the coefficients establishes a range of indices in (7) and in the following formulas. It must be mentioned that the Wigner function $D^{l_1}_{m_1 0}(\hat{\mathbf{n}}_0, \hat{\mathbf{r}}_{js})$ in (7) depends only on the two Eulerian angles defining the sense of the vector $\mathbf{r}_{js}$ in the coordinate system $\hat{\mathbf{n}}_0$. The third Eulerian angle characterizing the rotation of the coordinate system $\hat{\mathbf{r}}_{js}$ about the axis z_{js} is arbitrary.

In equation system (6), coefficients (7) include all features of the field outside the particles. When the particle spacing is far larger than λ and the particle size, these coefficients describe the spherical wave traveling from the *s*th particle to the *j*th one [5, 13].

Field relation (5) yields the $t^{(j)}_{pn}$ matrix [5, 10, 13]

$$t^{(j)}_{pn} = \exp(-i\mathbf{k}_{sc}\mathbf{R}_j + in\gamma_0 - ip\gamma)\times$$

$$\times \sum_{L,M} \frac{2L+1}{2} A^{(jpn)}_{LM} D^{*L}_{Mp}(\hat{\mathbf{n}}_0, \hat{\mathbf{k}}_{sc}). \qquad (8)$$

3. THE RADIATIVE TRANSFER EQUATION

The formulas above allow us to derive the equation for the noncoherent (diffuse) part of the first term on the right-hand side of (4). The relevant method for a semi-infinite medium and the normal incidence of radiation is presented in [10]. It is not too different from the sparse medium approach (see, e.g. [3-5] with the references) and is as follows. Substitute (8) in (4) to get the expression carrying the coefficient product $A^{(jpn)}_{LM} A^{*(j\mu\nu)}_{lm}$. For these coefficients, the system of equations corresponding to the noncoherent part of the scattered radiation is derived in the following way. The solution of system (6) is available by iteration. The so obtained series corresponds to the expansion of the solution of system (6) in wave scattering orders with the initial wave polarization *n* and the final polarization *p*. Next, a similar series is written for a wave with the initial polarization ν and the final polarization μ. Multiply the first series by the complex conjugate of the second series, keeping only those terms of the product series which refer to the same propagation trajectories of both waves. These scattering schemes correspond to the diffuse component of the scattered radiation. In the sparse medium case, these schemes lead to the equation which, on assemble averaging, yields the radiative transfer equation [2-5, 10, 14]. The medium characterization by the effective refractive index quite facilitates the assemble averaging. The complex effective refractive index m_{ef} can be calculated, for one, in the quasi-crystalline approximation of the medium [18, 2]. The introduction of the effective refractive index of the medium provides a means for describing the change of the wave amplitude and phase in the medium. For this purpose, the wave vector $\mathbf{k}_0$ in the medium is replaced by the vector $m_{ef}\mathbf{k}_0$. Then the wave vector $\mathbf{k}_0$ in (6) is substituted by the vector

$$\mathbf{K}_0 = \mathbf{k}_0 + k_0 \mathbf{n}_0 \frac{m_{ef} - 1}{\cos\vartheta_0}, \qquad (9)$$

and the vector $\mathbf{k}_{sc}$ in (8) is substituted by the vector

$$\mathbf{K} = \mathbf{k}_{sc} + k_0 \mathbf{n}_0 \frac{m_{ef} - 1}{\cos\vartheta}. \qquad (10)$$

The introduction of vectors (9) and (10) allows describing the changes of the wave amplitude and phase when it travels from the point where the wave enters the medium to the *j*th particle and from the *j*th particle to the point where the wave leaves the medium [13] (supposedly the layer backscattering area is considered). Then the matrix component product $t^{(j)}_{pn} t^{*(j)}_{\mu\nu}$ appears to be [10, 13]

$$t^{(j)}_{pn} t^{*(j)}_{\mu\nu} = \exp\left(i\mathbf{R}_j(\mathbf{K}^* - \mathbf{K})\right)\times$$

$$\times \exp\left[-i\gamma_0(\nu - n) + i\gamma(\mu - p)\right] \sum_{L,M,l,m} \frac{(2L+1)(2l+1)}{4}\times$$

$$\times A^{(jpn)}_{LM} A^{*(j\mu\nu)}_{lm} D^{*L}_{Mp}(\hat{\mathbf{n}}_0, \hat{\mathbf{k}}_{sc}) D^{l}_{m\mu}(\hat{\mathbf{n}}_0, \hat{\mathbf{k}}_{sc}), \qquad (11)$$

and the equation system for the coefficient product $A^{(jpn)}_{LM} A^{*(j\mu\nu)}_{lm}$ becomes [10, 13]

$$A_{LM}^{(jpn)}A_{L_1M_1}^{*(j\mu\nu)} = a_L^{(pn)}a_{L_1}^{*(\mu\nu)}D_{Mn}^{L}(\hat{\mathbf{n}}_0,\hat{\mathbf{k}}_0)D_{M_1\nu}^{*L_1}(\hat{\mathbf{n}}_0,\hat{\mathbf{k}}_0)\times$$

$$\times\exp\left[i\mathbf{R}_j(\mathbf{K}_0-\mathbf{K}_0^*)\right]+\sum_{q,q_1}a_L^{(pq)}a_{L_1}^{*(\mu q_1)}\times$$

$$\times\sum_{s,l,m,l_1,m_1}A_{lm}^{(sqn)}A_{l_1m_1}^{*(sq_1\nu)}H_{LMlm}^{(q)}(\hat{\mathbf{n}}_0,\hat{\mathbf{r}}_{js})H_{L_1M_1l_1m_1}^{*(q_1)}(\hat{\mathbf{n}}_0,\hat{\mathbf{r}}_{js}). \tag{12}$$

The coefficients $H_{LMlm}^{(q)}(\hat{\mathbf{n}}_0,\hat{\mathbf{r}}_{js})$ describe the wave propagation in between the scatterers. To take their refractive index m_{ef} into account, represent Hankel function (7) in the form

$$h_l(k_0x)=\frac{\exp(ik_0x)}{k_0x}\varsigma_l(k_0x), \tag{13}$$

where the function $\varsigma_l(x)$ allows the recurrent relation

$$\varsigma_{l+1}(x)=\frac{(2l+1)}{x}\varsigma_l(x)-\varsigma_{l-1}(x)$$

starting with the values

$$\varsigma_0(x)=-i, \qquad \varsigma_1(x)=-\left(1+\frac{i}{x}\right).$$

When the particle spacing substantially exceeds the particle size, $\varsigma_l(x)\approx(-i)^{l+1}$, and coefficients (7) describe a spherical wave. When the particle spacing is of the order of the particle size, coefficients (7) include all wave peculiarities outside the scatterers. Replace k_0 by $m_{ef}k_0$, in the exponent in (13) and consider the amplitude and phase change accompanying the wave traveling in between the scatterers.

Next transformations lie in the assemble averaging of matrix (11). The averaging is available in the quasi-crystalline approximation [18, 2] consisting in the following. The distribution function of the particles $p(\mathbf{r}_1,...,\mathbf{r}_N)$ (the probability density to find $\tilde{N}$ particles at the points $\mathbf{r}_1,...,\mathbf{r}_{\tilde{N}}$) can be written as [2, 18]

$$p(\mathbf{r}_1,...,\mathbf{r}_{\tilde{N}})=p(\mathbf{r}_i)p(\mathbf{r}_1,...,\mathbf{r}_i',...,\mathbf{r}_{\tilde{N}}\,|\,\mathbf{r}_i)=$$

$$=p(\mathbf{r}_i)p(\mathbf{r}_j\,|\,\mathbf{r}_i)p(\mathbf{r}_1,...,\mathbf{r}_i',...,\mathbf{r}_j',...,\mathbf{r}_{\tilde{N}}\,|\,\mathbf{r}_i,\mathbf{r}_j'). \tag{14}$$

Here $p(\mathbf{r}_i)$ is the probability density to find the ith particle at the point $\mathbf{r}_i$. Then $p(\mathbf{r}_1,...,\mathbf{r}_i',...,\mathbf{r}_{\tilde{N}}\,|\,\mathbf{r}_i)$ is the conventional probability to find the rest of particles at relevant points (the prime over $\mathbf{r}_i$ indicates that the variable $\mathbf{r}_i$ is absent) and $p(\mathbf{r}_j\,|\,\mathbf{r}_i)$ is the conventional probability to find the jth particle at the point $\mathbf{r}_j$ with the ith particle fixed. When $\tilde{N}$ is large and the collection of particles is homogeneous and isotropic,

$$p(\mathbf{r}_j\,|\,\mathbf{r}_i)\simeq\eta g\left(|\,\mathbf{r}_j-\mathbf{r}_i\,|\right)\Big/\tilde{N} \tag{15}$$

(see, e.g. [2, 18]), where η is the concentration of particles and $g(r)$ is the pair correlation function [19, 20]).

The expansion in (14) can be extended to the case with two particles fixed, three particles fixed and so on. Then the assemble average of (11) will be expressed via the coefficient products $A_{LM}^{(jpn)}A_{lm}^{*(j\mu\nu)}$, assemble averaged with the jth particle fixed. In turn, the averages of these products with the jth particle fixed will come from (12) in terms of their averages with the jth and the sth particles fixed and so on. Thus, the hierarchy of equations has been obtained for finding the assemble average of (11) [2]. The quasi-crystalline approximation suggests that the average with two particles fixed is approximately equal to the average with one particle fixed [2, 18]. This assumption reduces the equation hierarchy to only one equation. The calculation of the average of coefficient product $A_{LM}^{(jpn)}A_{lm}^{*(j\mu\nu)}$ (12) becomes relatively simple, and so does, consequently, the calculation of the average of reflection matrix (11). We emphasize that this approximation is similar to the ladder diagram summation presented in [4] for a sparse medium but, in addition, it includes the pair correlations [2, 21]. In other words, the same as in Tverskoy's theory for a sparse medium (see, e.g. [1,4]), this approximation also does not include the scattering schemes of double, triple, etc. wave scattering from the same obstacle.

Multiply (11) and (12) by (14) and integrate it over the medium volume to get the assemble-averaged reflection matrix. Denote

$$B_{LL_1lM_2}^{(j)(pn)(\mu\nu)}=\sum_{M,m}\frac{(2L+1)(2l+1)}{4}\times$$

$$\times A_{LM}^{(jpn)}A_{lm}^{*(j\mu\nu)}C_{LMl-m}^{L_2M_2}(-1)^{m+\mu}\exp\left(i\gamma_0(n-\nu)\right) \tag{16}$$

and

$$B^{(z)(pn)(\mu\nu)}_{LL_1lM_2} = \left\langle B^{(j)(pn)(\mu\nu)}_{LL_1lM_2} \right\rangle.$$

Expand the product of the two Wigner functions in the Clebsch–Gordan series [15]. From (11), after simple manipulations,

$$S^{(nc)}_{pn\mu\nu} = \frac{\eta}{k_0} \sum_{L,L_1,L_2,M} D^{*L_2}_{MN_0}(\varphi,\theta,0) C^{L_2N_0}_{LpL_1-\mu} \times$$

$$\times \int_0^{k_0 Z_0} B^{(\tilde{z})(pn)(\mu\nu)}_{L_2MLL_1} \exp\left(\frac{\tau\tilde{z}}{\cos\vartheta}\right) d\tilde{z}. \qquad (17)$$

Here the reflection matrix $S^{(nc)}_{pn\mu\nu}$ for the noncoherent portion of the scattered radiation is normalized to the unit area of the medium surface, $N_0 = p - \mu$, and $\tau = 2\,\mathrm{Im}(m_{ef})$. Matrix (17) can be also adopted for describing the scattered radiation in the directions $\vartheta < \pi/2$. For this, $\tilde{z}$ in (17) is replaced by $\tilde{z} - k_0 Z_0$ [13]. Then the exponential factor will describe the radiation absorption on the way from the $\tilde{z}$ point to the point of the radiation exit from the medium in the directions $\vartheta < \pi/2$.

The system of equations for the coefficients $B^{(z)(pn)(\mu\nu)}_{L_2M_2LL_1}$ comes from system (12). Multiply (12) by the coefficients of $A^{(jpn)}_{LM} A^{*(j\mu\nu)}_{lm}$ in (16), sum up over indices M and m and employ the quasi-crystalline approximation to have the system of equations for the coefficients $B^{(z)(pn)(\mu\nu)}_{L_2M_2LL_1}$. In this case, after the product of the two Wigner functions has been expanded into the Clebsch–Gordan series in view of the unitary property of the Clebsch–Gordan coefficients [15], the first term on the right-hand side in (12) takes a simple form. To calculate the average of the second term on the right-hand side of (12), we substitute

$$g(r_{js}) H^{(q)}_{LMlm}(\hat{\mathbf{n}}_0, \hat{\mathbf{r}}_{js}) H^{*(q_1)}_{L_1M_1l_1m_1}(\hat{\mathbf{n}}_0, \hat{\mathbf{r}}_{js}) =$$

$$= \Big[g(r_{js}) H^{(q)}_{LMlm}(\hat{\mathbf{n}}_0, \hat{\mathbf{r}}_{js}) H^{*(q_1)}_{L_1M_1l_1m_1}(\hat{\mathbf{n}}_0, \hat{\mathbf{r}}_{js}) -$$

$$- \tilde{H}^{(q)}_{LMlm}(\hat{\mathbf{n}}_0, \hat{\mathbf{r}}_{js}) \tilde{H}^{*(q_1)}_{L_1M_1l_1m_1}(\hat{\mathbf{n}}_0, \hat{\mathbf{r}}_{js}) \Big] +$$

$$+ \tilde{H}^{(q)}_{LMlm}(\hat{\mathbf{n}}_0, \hat{\mathbf{r}}_{js}) \tilde{H}^{*(q_1)}_{L_1M_1l_1m_1}(\hat{\mathbf{n}}_0, \hat{\mathbf{r}}_{js}).$$

Here the coefficients $\tilde{H}^{(q)}_{LMlm}(\hat{\mathbf{n}}_0, \hat{\mathbf{r}}_{js})$, differ from coefficients (7) in that the Hankel functions are replaced by their asymptotical values at $k_0 r_{js} \gg l_1$, i.e. these coefficients correspond to a sparse medium. Then practically the same as in [10], we arrive at the following equation system for the coefficients $B^{(z)(pn)(\mu\nu)}_{L_2MLL_1}$:

$$B^{(z)(pn)(\mu\nu)}_{L_2MLL_1} = A^{(z)(pn)(\mu\nu)}_{L_2MLL_1} + \frac{4\pi\eta}{k_0^3} \times$$

$$\times \sum_{q,q_1} \frac{(2L+1)(2L_1+1)}{4} a^{(pq)}_L a^{*(\mu q_1)}_{L_1} \sum_{l,l_1,l_2} B^{(z)(qn)(q_1\nu)}_{l_2Mll_1} G^{(qq_1)}_{L_2MLL_1ll_1l_2} +$$

$$+ \frac{2\pi\eta}{k_0^3} \sum_{q,q_1} \chi^{(pq)(\mu q_1)}_{L_2LL_1} \sum_{l,l_1,l_2} C^{l_2N}_{lql_1-q_1} \times$$

$$\times \int B^{(y)(qn)(q_1\nu)}_{l_2Mll_1} \exp(-\tau x) d^{L_2}_{MN}(\omega) d^{l_2}_{MN}(\omega) \sin\omega\, d\omega dx. \qquad (18)$$

Here $y = z - x\cos\omega$, the angle ω is measured from the $-\mathbf{n}_0$ direction. The upper limit of the integration with respect to x is $z/\cos\omega$, if $\omega < \pi/2$, and it is $(z - Z_0 k_0)/\cos\omega$, if $\omega > \pi/2$; $d^L_{MN}(\omega)$ is the Wigner function [15], $N = q - q_1$;

$$A^{(z)(pn)(\mu\nu)}_{L_2MLL_1} = \chi^{(pn)(\mu\nu)}_{L_2LL_1} \exp\left(-\frac{\tau z}{\cos\vartheta_0}\right) D^{L_2}_{Mn-\nu}(\varphi_0, \vartheta_0, 0); \qquad (19)$$

$$\chi^{(pn)(\mu\nu)}_{L_2Ll} = \frac{(2L+1)(2l+1)}{4} a^{(pn)}_L a^{*(\mu\nu)}_l C^{L_2n-\nu}_{Lnl-\nu};$$

$$G^{(qq_1)}_{L_2MLL_1ll_1l_2} = (-1)^{M+L_1+l+l_2} \sum_{b,c,d} i^{d-b-c} \Pi_{L_2l_2bc} C^{b0}_{Lql-q} \times$$

$$\times C^{c0}_{L_1q_1l_1-q_1} C^{d0}_{b0c0} C^{d0}_{L_2Ml_2-M} Y_{bcd} \begin{Bmatrix} l_1 & L_1 & c \\ l & L & b \\ l_2 & L_2 & d \end{Bmatrix}; \qquad (20)$$

$$\Pi_{bcdf} = \sqrt{(2b+1)(2c+1)(2d+1)(2f+1)};$$

$$Y_{bcd} = \int_{\rho_0}^{\infty} \Big[g(x)\varsigma_b(x)\varsigma^*_c(x) - i^{c-b} \Big] j_d(i\tau x) \exp(-\tau x) dx. \qquad (21)$$

In the formulas above, $\rho_0 = 2k_0\tilde{a}$, $\tilde{a}$ is the medium particle radius, $j_l(x)$ is the spherical Bessel function, and $g(x)$ is the pair correlation function (15). The braced expression in (20) is the 9j Wigner symbol [15].

The transfer equation in the form of (17) and (18) is the medium layer equation in a circular polarization basis. This equation can be rewritten as a series in azimuthal harmonics, which is standard practice for the classical transfer equation in a sparse medium [22]. Then formula (17) takes the form

$$S_{pn\mu\nu}^{(nc)} = \frac{\eta}{k_0} \sum_{L,L_1,L_2,M} \exp\left(iM(\varphi-\varphi_0)\right) \mathrm{d}_{MN_0}^{L_2}(\theta)\, C_{LpL_1-\mu}^{L_2N_0} \times$$

$$\times \int_0^{k_0Z_0} B_{L_2MLL_1}^{(\tilde{z})(pn)(\mu\nu)} \exp\left(\frac{\tau\tilde{z}}{\cos\vartheta}\right) \mathrm{d}\tilde{z}. \qquad (22)$$

In this case, only the first right term of (18) has a change. We mean coefficients (19), where the function $D_{Mn-\nu}^{L_2}(\varphi_0,\vartheta_0,0)$ has to be replaced by $d_{Mn-\nu}^{L_2}(\vartheta_0)$.

The obtained transfer equation is a more general one than the equation for the incident radiation normal to the semi-infinite medium layer in [10]. Also, a mention should be made of one more difference between the just obtained transfer equation and the equation from [10]. It refers to the appearance of coefficients (21). In [10], the size of medium scatterers is supposed to be of the wavelength order and larger, the medium absorption inconsiderable $\left(\mathrm{Im}(m_{ef}) \ll 1\right)$. On these assumptions, coefficients (21) appear to be [10]

$$Y_{bcd} = \int_{\rho_0}^{\infty} \left(g(x)-1\right) \varsigma_b(x) \varsigma_c^*(x) j_d(i\tau x) \exp(-\tau x)\mathrm{d}x. \qquad (23)$$

Coefficients (23) vanish if $g(x)=1$, i.e. for a sparse medium. In this case, the scatterers supposedly reside far apart from one another. No assumptions were made for the (21) derivation. In particular, coefficients (21) are still valid for scatterers that are small compared to the wavelength. For them, coefficients (21) vanish if $g(x)=1$ with the proviso that the scatterers are far from one another. In the far zone, $\varsigma_l(x) \simeq (-i)^{l+1}$ and, as seen from (21), these coefficients vanish unless the correlation is included.

Formulas (22) and (18) coincide with those from [10] as $Z_0 \to \infty$ and $\vartheta_0 = 0$. In this case,

$$A_{L_2MLL_1}^{(z)(pn)(\mu\nu)} = \chi_{L_2LL_1}^{(pn)(\mu\nu)} \exp(-\tau z)\delta_{Mn-\nu} \qquad (24)$$

and, as seen, $M = n-\nu$ in (18). The Stokes parameters of the incident radiation lie in the plane of $\mathbf{n}_0$ and $\mathbf{k}_0$ vectors. The Stokes parameters of the scattered radiation are in the plane of $\mathbf{n}_0$ and $\mathbf{k}_{sc}$ vectors (Fig. 1). Therefore expression (22) depends on the azimuthal difference between the incident and scattered radiation directions. When the incident radiation is normal to the medium layer, the Stokes parameters are convenient to define in the plane of $\mathbf{k}_0$ and $\mathbf{k}_{sc}$ vectors. Then formula (22) will be azimuthally independent.

The relationship between the medium packing density and the transfer equation is established by coefficient G involved in equation system (18). The correlation function $g(x)$ is introduced in this coefficient via formula (21). When the medium is free from the correlation and the scatterers are far apart from one another, the coefficient G vanishes. Then the complexity of the obtained formulas goes down substantially. The summation over L, L_1 in (22) yields [10]

$$S_{pn\mu\nu}^{(nc)} = \frac{\eta}{k_0} \sum_{L,M} \exp\left(iM(\varphi-\varphi_0)\right) \mathrm{d}_{MN_0}^{L}(\theta) \times$$

$$\times \int_0^{k_0Z_0} \alpha_{LM}^{(\tilde{z})(pn)(\mu\nu)} \exp\left(\frac{\tau\tilde{z}}{\cos\vartheta}\right) \mathrm{d}\tilde{z}, \qquad (25)$$

where coefficients $\alpha_{LM}^{(z)(pn)(\mu\nu)}$ are available from the equation system

$$\alpha_{LM}^{(z)(pn)(\mu\nu)} = \chi_L^{(pn)(\mu\nu)} d_{Mn-\nu}^{L}(\vartheta_0) \exp\left(-\frac{\tau z}{\cos\vartheta_0}\right) +$$

$$+ \frac{2\pi\eta}{k_0^3} \sum_{q,q_1} \chi_L^{(pq)(\mu q_1)} \times$$

$$\times \sum_l \int \alpha_{lM}^{(y)(qn)(q_1\nu)} \exp(-\tau x) d_{MN}^{L}(\omega) d_{MN}^{l}(\omega) \sin\omega \mathrm{d}\omega \mathrm{d}x. \qquad (26)$$

Here it has been introduced the notation

$$\chi_{L_1}^{(pn)(\mu\nu)} = \sum_{L,l} \frac{(2L+1)(2l+1)}{4} a_L^{(pn)} a_l^{*(\mu\nu)} C_{Lnl-\nu}^{L_1 n-\nu} C_{Lpl-\mu}^{L_1 p-\mu}.$$

Formulas (25), (26) represent the vector equation of radiation transfer for a sparse medium layer in a circular polarization basis. For its derivation from Maxwell's equations, refer to works [4, 5, 13]. For scalar waves, equation (26) is presented in [22] as a source function in a medium. Some examples of the numerical solution of equation (22) in the case of a semi-infinite medium and the normal incidence on the medium surface can be found in [10] together with the relevant code for system (22) solution.

Let us estimate how much the wave nonuniformity around the particles acts on the radiation reflection intensity from an optically thin medium layer when the incident radiation is normal to the layer surface. In this case, coefficients (19) are written in the form of (24). That the layer is optically thin allows the approximation $B^{(\tilde{z})(pn)(\mu\nu)}_{L_2MLL_1} \simeq \exp(-\tau\tilde{z})\tilde{B}^{(pn)(\mu\nu)}_{L_2MLL_1}$, in system (18). The integral involved in the last right term in (18) can be written as

$$\int B^{(y)(qn)(q_1\nu)}_{l_2Mll_1} \exp(-\tau x) d^{L_2}_{MN}(\omega) d^{l_2}_{MN}(\omega) \sin\omega d\omega dx \simeq$$

$$\simeq \frac{\exp(-\tau\tilde{z})}{\tau} \tilde{B}^{(pn)(\mu\nu)}_{L_2MLL_1} d^{L_2}_{MN}(\pi/2) d^{l_2}_{MN}(\pi/2).$$

Denote by $\xi = 4\eta\pi\tilde{a}^3/3$ the medium packing density. From (22) and (18) after some manipulations,

$$S^{(nc)}_{pn\mu\nu} = \frac{3\xi k_0^2 \cos\vartheta\left[1-\exp(-\tau k_0 Z_0 \beta)\right]}{4\pi\tau\tilde{x}_0^3(\cos\vartheta - 1)} \times$$

$$\times \sum_{L,L_1,L_2} d^{L_2}_{MN_0}(\theta) C^{L_2N_0}_{LpL_1-\mu} \tilde{B}^{(pn)(\mu\nu)}_{L_2MLL_1}, \qquad (27)$$

where $M = n-\nu$, $N_0 = p-\mu$, $\beta = (\cos\vartheta - 1)/\cos\vartheta$, and the coefficients $\tilde{B}^{(pn)(\mu\nu)}_{L_2MLL_1}$ come from the system

$$\tilde{B}^{(pn)(\mu\nu)}_{L_2MLL_1} = \chi^{(pn)(\mu\nu)}_{L_2LL_1}\delta_{M,n-\nu} +$$

$$+\frac{3\xi}{\tilde{x}_0^3}\sum_{q,q_1}\frac{(2L+1)(2L_1+1)}{4} a^{(pq)}_L a^{*(\mu q_1)}_{L_1} \times$$

$$\times \sum_{l,l_1,l_2} \tilde{B}^{(qn)(q_1\nu)}_{l_2Mll_1} G^{(qq_1)}_{L_2MLL_1ll_1l_2} + \frac{3\xi}{2\tau\tilde{x}_0^3}\sum_{q,q_1}\chi^{(pq)(\mu q_1)}_{L_2LL_1} \times$$

$$\times \sum_{l,l_1,l_2} C^{l_2N}_{lql_1-q_1} \tilde{B}^{(qn)(q_1\nu)}_{l_2Mll_1} d^{L_2}_{MN}(\pi/2) d^{l_2}_{MN}(\pi/2).$$

Here $N = q - q_1$.

The reflected radiation intensity is characterized by the reflection matrix component $R_{11} = U\sum_{p,n} S^{(nc)}_{pnpn}$, where $U = -\pi/\left(2k_0^2\cos\vartheta\right)$ (see [4, 10, 13]). Examples of this component calculation are reported in Fig. 2 for a $k_0 Z_0 = 10$ thick medium layer filled with particles of the size $\tilde{x}_0 = k_0\tilde{a} = 2$ and the refractive index $\tilde{m} = 1.5 + i0.0$. The effective refractive index of the medium has been calculated in the quasi-crystalline approximation [2]. The imaginary parts for this refractive index for cases of packing density ξ shown in Fig. 2 are: $\mathrm{Im}(m_{ef}) = 0.026$ ($\xi = 0.1$), $\mathrm{Im}(m_{ef}) = 0.035$ ($\xi = 0.2$), $\mathrm{Im}(m_{ef}) = 0.033$ ($\xi = 0.3$), $\mathrm{Im}(m_{ef}) = 0.026$ ($\xi = 0.4$). The solid curves correspond to the calculations in the uniform wave approximation, i.e. for $\varsigma_l(x) = (-i)^{l+1}$ in (21). The dashed curves correspond to the calculations with the wave nonuniformities involved. That the element R_{11} increases with packing density is caused by both the ξ growth (see formula (27)) and by a larger contribution from the mul-

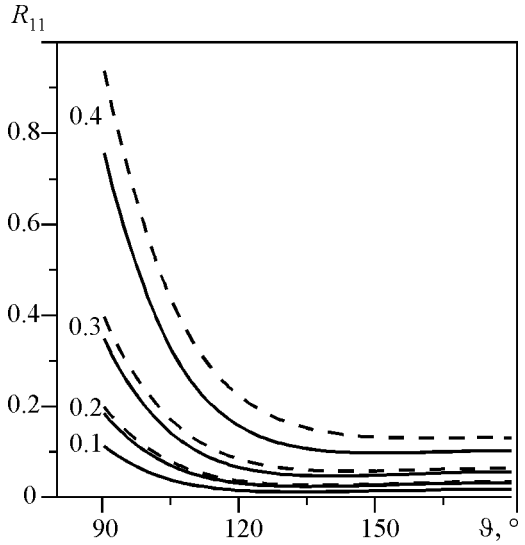

FIG. 2: The reflection matrix component R_{11} versus the scattering angle for different packing densities ξ of particles in an optically thin medium layer. The ξ values are indicated on the curves. The particle parameters are $k_0\tilde{a} = 2$, $\tilde{m} = 1.5 + i0.0$. The solid line corresponds to the calculations involving only the particle correlation (the uniform wave approximation). The dotted line is for both particle correlation and wave nonuniformities around the particles involved

tiple scattering. As seen from Fig. 2, the wave nonuniformities around the scatterers take effect for a packing density $\xi \geq 0.3$. A similar result as to the packing density estimation was obtained in [10] for a semi-infinite medium of absorbing particles.

4. CONCLUSIONS

The obtained equation of radiative diffuse transfer in a layer of a dense-packing medium of similar spherical scatterers is more general than the equation from work [10], which corresponds to the radiation normal incidence on the medium surface. The assemble averaging employs the quasi-crystalline approximation which includes the two-particle correlation between the scatterers. The equation was obtained in full regard to the wave nonuniformities near the scatterers. The allowance for these nonuniformities substantially complicates the transfer equation compared to the sparse medium case. The equation describes the diffuse part of the medium scattered radiation, which corresponds to the ladder diagram summation in the diagram representation of the Bethe–Salpeter equation. In this case, the interference of waves scattered by closest neighbors is not included. Therefore the equation can be employed when the scatterer size is of the radiation wavelength order and larger. The wave interference leading to the backscattering coherent amplification (weak localization) is not considered either [4, 5, 9, 13]. The contribution from the interference part of the scattered radiation to the medium reflection matrix is left to a separate paper.

REFERENCES

1. Ishimaru, A. Wave Propagation and Scattering in Random Media. Vol. 1. New York: Academic, 1978.
2. Tsang, L. and Kong, J. A. Scattering of electromagnetic waves. Advanced topics. New York: Wiley-Interscience; 2001.
3. Borovoi, A. G. Multiple scattering of short waves by uncorrelated and correlated scatterers. In: Kokhanovski, A. editor. Light Scattering Reviews. Chichester: Praxis Publishing Ltd, UK; 2006. p. 181-248.
4. Mishchenko, M. I., Travis, L. D., and Lacis, A. A. Multiple Scattering of Light by Particles. Radiative Transfer and Coherent Backscattering. Cambridge: Cambridge University Press; 2006.
5. Tishkovets, V. P., Multiple scattering of light by a layer of discrete random medium: backscattering, *J. Quant. Spectrosc. Radiat. Transfer*, 72:123-137, 2002.
6. Bohren, C. F. and Huffman, D. R. Absorption and Scattering of Light by Small Particles. New York: Wiley; 1983.
7. Tishkovets, V. P., Backscattering of light by densely packed systems of particles, *Opt. i Spektr*., 85(2):233-238, 1998 (in Russian).
8. Tishkovets, V. P. and Litvinov, P. V., Opposition effects in scattering of light by regolith-type media, *Astron. Vestn*., 33(2):186-192, 1999 (in Russian).
9. Barabanenkov, Yu. N., Kravtsov, Yu. A., Ozrin, V. D., and Saichev, A. I. Enhanced backscattering in optics. In: Wolf, E., editor. Progress in Optics XXIX. Vol. 29. Amsterdam: Elsevier; 1991. p. 65-197.
10. Tishkovets, V. P. and Jockers, K., Multiple scattering of light by densely packed random media of spherical particles: Dense media vector radiative transfer equation, *J. Quant. Spectrosc. Radiat. Transfer*., 101:54-72, 2006.
11. Tsang, L., Chen, C.-T., Chang, A. T. C., Guo, J., and Ding, K.-H., Dense media radiative transfer theory on quasi-crystalline approximation with applications to passive microwave remote sensing of snow, *Radio Sci*., 35:731-749, 2000.
12. Tsang, L., Kong, J. A., and Shin, R. T., Radiative transfer theory for active remote sensing of a layer of nonspherical particles, *Radio Sci*., 19:629-642, 1984.
13. Tishkovets, V. P. and Mishchenko, M. I., Coherent backscattering of light by a layer of discrete random medium, *J. Quant. Spectrosc. Radiat. Transfer*., 86:161-180, 2004.
14. Newton, R. Scattering Theory of Waves and Particles. Moscow: Mir; 1969 (in Russian).
15. Varshalovich, D. A., Moskalev, A. N., and Khersonski, V. K. Quantum Theory of Angular Momentum. Moscow: Nauka; 1975 (in Russian).
16. Tishkovets, V. P. and Litvinov, P. V., Coefficients of light attenuation by chaotic orientation clusters of spherical particles in double scattering approximation, *Opt. i Spektr*., 81:319-322, 1996 (in Russian).
17. Felderhof, B. U. and Jones, R. B., Addition theorems for spherical wave solutions of the vector Helmholtz equation, *J. Math. Phys*., 28:836-839, 1987.
18. Lax, M., Multiple scattering of waves. II. The effective field in dense systems, *Phys. Rev.* 85:621-629, 1952.
19. Lifshits, I. M., Gredeskul, S. A., and Pastur, L. A. Introduction to Theory of Disordered Systems. Moscow: Nauka; 1982 (in Russian).
20. Percus, J. K. and Yevick, G. J., Analysis of classical statistical mechanics by means of collective coordinates, *Phys. Rev.* 110:1-13, 1958.
21. Bringi, V. N., Seliga, T. A., Varadan, V. K., and Varadan, V. V. Bulk propagation characteristics of discrete random media. In: Chow, P. L., Kohler, W. E., and Papanicolaou, G. C., editors. Multiple Scattering and Waves in Random Media. Amsterdam: North-Holland Publishing Company; 1981. p. 43-75.
22. Yanovitski, E. G. The Scattering of Light in Nonuniform Atmospheres. Kyiv: Naukova Dumka; 1995(in Russian).

Radio Physics and Radio Astronomy, 1(1), 79–89 (2010)

MUTUAL SCREENING OF SCATTERERS IN THE NEAR FIELD

V. P. Tishkovets

Institute of Radio Astronomy, National Academy of Sciences of Ukraine, 4, Chervonopraporna St., 61002 Kharkiv, Ukraine

*Address all correspondence to V. P. Tishkovets E-mail:tishkovets@ri.kharkov.ua

The equations in theory of electromagnetic wave scattering by a cluster (aggregate) of spherical particles are analyzed in terms of two scattering models: one involves the near field, the other ignores it. For some cluster examples, the radiation scattered by cluster particles was calculated to find out that the radiation intensity in the directions of mutual screening of particles is substantially larger from the model ignoring the near field than from that considering it.

KEY WORDS: *cattering, screening, cluster, spherical particles, intensity, radiation*

1. INTRODUCTION

At present the theoretical treatment of multiple scattering of electromagnetic waves (EMW) by discrete media rests on the idea that the secondary waves traveling outside medium scatterers are spherical. In particular, the classical equation of radiation transport comes from Maxwell's equations right under the assumption that the scatterers are in the far zones of one another [1, 2]. In spite of the fact that this assumption is reasonable for sparse media where the scatterer spacing exceeds the scatterer size tremendously, the transport equation and its modifications are also being of common use when radiation reflection characteristics of dense packing media are treated [3-6]. One such modification of the classical transport equation is the so-called diffuse approximation. The practice exists [7] to instantly apply it to dense media, paying no attention that the assumption that waves traveling outside the medium scatteres are spherical drops a number of characteristic features of the EMW scattering by dense-packing systems. In particular, peculiarities of the near-field scattering are ignored.

The near field effect on the radiation scattering characteristics of discrete media has yet to be studied. Only rather few works study specific features of the near-field scattering in dense-packing systems of several scatterers (see [8-14] with the references). In particular, the emphasis was [8-12] on the amount of linear polarization of the scattered radiation in the near field. About the scatterer, the total (incident plus scattered) field is nonuniform, which makes the electric vector depart from the electric vector of the incident wave. As a result, the field vector component parallel to the incident wave vector appears. For clusters (aggregates) of particles compared in size with the wavelength, the mentioned departure of the field vector produces some negative linear polarization in the area of the opposition scattering angles. As to the intensity of the scattered radiation, the field vector departure diminishes it in the forward and backward scattering directions and raises it in the side directions [8-12].

The present paper considers one more effect related to the near field. This is the mutual screening of scatterers. This phenomenon can grow important when the scatterer spacing is comparable with its size. When the scatterer is vastly larger than the incident wave-

ISSN 2152-274X

length, the mutual screening is analogous to the shading effect (see [3] and [13, 14]). Yet the mutual screening phenomenon will be also encountered in systems of scatterers far less in size than the wavelength.

The screening effect will be considered by examples of clusters of spherical scatterers. Section 2 contains essential formulas of EMW scattering theory for systems of such scatterers. The near field is thoroughly analyzed. For the scatterer systems, the calculation relationships of radiation scattering characteristics are given in both model terms: with the near field included or ignored. On this basis, both models are compared for scattered field intensity in Section 3. The comparison starts with a simplest-kind cluster consisting of two similar scatterers and is extended to complicated chaotic-orientation clusters (with equally probable orientation distribution function) for cases of 50, 100 and 200 similar near-spherical particles randomly distributed over the cluster, the packing density being of about 0.2.

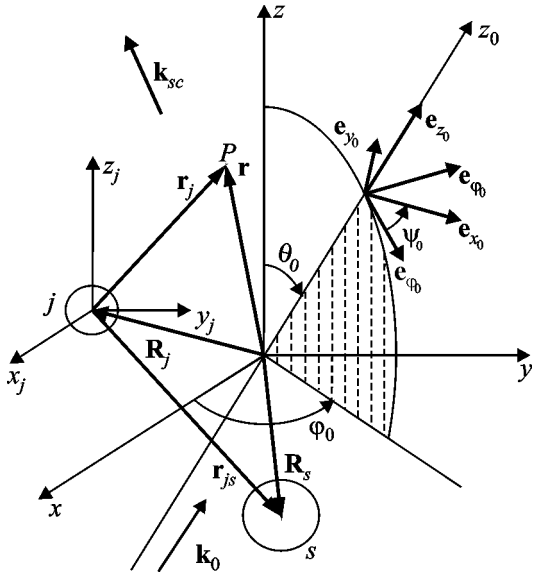

FIG. 1: The coordinate systems for describing the EMW scattering by a cluster

2. EMW SCATTERING BY A SYSTEM OF SPHERICAL PARTICLES. THE NEAR FIELD

The EMW scattering theory for systems (clusters) of arbitrary-size spherical scatterers of an arbitrary refractive index can be found in the literature (see, e.g. monographs [15, 16] with the references). The essential equations are presented below, the notations adopted to coincide with those [17, 18].

The coordinate systems to describe the EMW scattering by a cluster are shown in Fig. 1. Let a cluster consist of N particles located by their radius-vectors $\mathbf{R}_j$ $(j=1...N)$ in a laboratory coordinate system $\hat{\mathbf{n}}_0$ such that the x, y, z axes and the origin are at the center of the minimum-radius sphere enveloping the cluster. A caret over a symbol, for instance $\hat{\mathbf{v}}$, indicates a right-handed coordinate system with the z axis directed along the vector $\mathbf{v}$. The incident plane wave is considered in the coordinate system $\hat{\mathbf{k}}_0$, the axis z_0 aligned with the incident wave vector $\mathbf{k}_0$ ($k_0 = 2\pi/\lambda$ and λ is the wavelength). The wave scattered by the cluster travels to the observation point along the wave vector $\mathbf{k}_{sc}$ in the coordinate system $\hat{\mathbf{k}}_{sc}$. The rotation from the coordinate system $\hat{\mathbf{n}}_0$ to the coordinate system $\hat{\mathbf{k}}_0$ is given by the Eulerian angles φ_0, θ_0, ψ_0. The $\hat{\mathbf{n}}_0$ to $\hat{\mathbf{k}}_{sc}$ rotation is given by the Eulerian angles φ_{sc}, θ_{sc}, ψ_{sc}. The $\hat{\mathbf{k}}_0$ to $\hat{\mathbf{k}}_{sc}$ rotation is given by the Eulerian angles φ, θ, ψ. These systems are completed with local coordinates related to each scatterer. Their origins are at the centers of the scatterers, the axes are aligned with the axes of the laboratory coordinate system (Fig.1). The local coordinate systems are required for describing the waves acting on each particle from the side of the rest members of the cluster.

The EMW scattering is convenient to consider in a circular polarization basis (the so-called CP-representation [15]). For a plane circularly polarized monochromatic wave, the electric field at the point P (Fig. 1) can be written as follows

$$\mathbf{E}^{(0)} = \mathbf{e}_n(\hat{\mathbf{k}}_0)\exp(i\mathbf{k}_0\mathbf{r} - i\omega t). \qquad (1)$$

Here $n = \pm 1$, ω is the frequency, and $\mathbf{e}_n(\hat{\mathbf{k}}_0)$ is the covariant cyclic unit vector [19] generated by the unit vectors $\mathbf{e}_{x_0}$, $\mathbf{e}_{y_0}$ in the coordinate system $\hat{\mathbf{k}}_0$ (Fig. 1). For $n = 1$, the sense of rotation of vector (1) is that of a right-hand screw when looking in the direction of vector $\mathbf{k}_0$ and a left-handed screw for $n = -1$. The corresponding circular polarization of waves is said to be right-handed or left-handed, respectively [15]. The scattered wave dependence on time t is $\exp(-i\omega t)$ and will be omitted.

At any point outside the particles, the scattered field is supposed to be the sum of the fields scattered by each particle of the cluster [15]

$$\mathbf{E}=\sum_{j=1}^{N}\mathbf{E}^{(j)}, \tag{2}$$

where (see, e.g. [17])

$$\mathbf{E}^{(j)}=\sum_{LM}\Bigg[B_{LM}^{(j)}h_L(k_0r_j)\mathbf{X}_{LM}(\theta_j,\varphi_j)+$$

$$+\frac{1}{k_0}A_{LM}^{(j)}\nabla\times h_L(k_0r_j)\mathbf{X}_{LM}(\theta_j,\varphi_j)\Bigg]. \tag{3}$$

Equation (3) expresses the wave scattered by the *j*th particle with respect to the coordinate system whose origin is at this particle center and the axes are parallel to the $\hat{\mathbf{n}}_0$ system axes (Fig. 1). Here θ_j, φ_j are the angular coordinates of the observation point (vector $\mathbf{r}_j=\mathbf{r}-\mathbf{R}_j$) in the *j*th coordinate system, $h_L(x)$ is the spherical Hankel function, and $\mathbf{X}_{LM}(\theta_j,\varphi_j)$ is the vector spherical function [16, 19] ($L=1, 2..., -L\le M\le L$). Notice that (3) is the general solution to the Helmholtz vector equation when the field divergence is zero (no free charges). A particular appearance of the scattered field is determined by the coefficients $A_{LM}^{(j)}$ and $B_{LM}^{(j)}$ available from the boundary condition that the field tangential components are continuous across the scatterer surface. Solving these equations with the boundary conditions applied delivers these coefficients depending on the size and the refractive index of the scatterer.

The common practice is that the scattered radiation characteristics of the cluster are considered in the far zone defined by the conditions [2] $k_0(r-a_m)\gg 1$, $2k_0r\gg(k_0a_m)^2$, and $r\gg a_m$. Here a_m is the radius of the minimum sphere circumscribed around the cluster and *r* is the observation point distance in the laboratory coordinate system. Upon the asymptotical representation $h_L(x)\approx i^{-L-1}\exp(ix)/x$ ($x\gg L$, $x\gg 1$), the cluster far field comes from (3) in the form [17]:

$$\mathbf{E}^{(j)}=\frac{\exp(ik_0r)}{-ik_0r}\exp(-i\mathbf{k}_{sc}\mathbf{R}_j)\times$$

$$\times\sum_{LMp}\frac{2L+1}{2}A_{LM}^{(jpn)}D_{Mp}^{*L}(\hat{\mathbf{n}}_0,\hat{\mathbf{k}}_{sc})\mathbf{e}_p(\hat{\mathbf{k}}_{sc}). \tag{4}$$

Here $p=\pm 1$, $\mathbf{e}_p(\hat{\mathbf{k}}_{sc})$ is the covariant cyclic unit vector [19] in the coordinate system $\hat{\mathbf{k}}_{sc}$, $D_{Mn}^{L}(\hat{\mathbf{n}}_0,\hat{\mathbf{k}}_{sc})=D_{Mn}^{L}(\varphi_{sc},\theta_{sc},\psi_{sc})=\exp(-iM\varphi_{sc})d_{Mn}^{L}(\theta_{sc})\exp(-in\psi_{sc})$ is the Wigner function [19], the asterisk stands for the complex conjugation, and

$$A_{LM}^{(jpn)}=i^{-L}\sqrt{\frac{1}{2\pi(2L+1)}}\left(A_{LM}^{(j)}+pB_{LM}^{(j)}\right). \tag{5}$$

The coefficients $A_{LM}^{(jpn)}$ come from the equation system (see, e.g. [17]) in the form

$$A_{LM}^{(jpn)}=a_L^{(jpn)}\exp(i\mathbf{k}_0\mathbf{R}_j)D_{Mn}^{L}(\hat{\mathbf{n}}_0,\hat{\mathbf{k}}_0)+$$

$$+\sum_q a_L^{(jpq)}\sum_{s\ne j}^{N}\sum_{lm}A_{lm}^{(sqn)}H_{LMlm}^{(q)}(\hat{\mathbf{n}}_0,\hat{\mathbf{r}}_{js}). \tag{6}$$

Here $\hat{\mathbf{r}}_{js}$ is the coordinate system with the axis z_{js} aligned with the vector $\mathbf{r}_{js}$ (Fig. 1), $q=\pm 1$; $a_L^{(jpn)}=a_L^{(j)}+pnb_L^{(j)}$, where $a_L^{(j)}$, $b_L^{(j)}$ are the coefficients of field expansion (3) for the *j*th particle isolated [2], and

$$H_{LMlm}^{(q)}(\hat{\mathbf{n}}_0,\hat{\mathbf{r}}_{js})=\frac{2l+1}{2}(-1)^m\times$$

$$\times\sum_{l_1}i^{-l_1}h_{l_1}(k_0r_{js})D_{m_1 0}^{l_1}(\hat{\mathbf{n}}_0,\hat{\mathbf{r}}_{js})C_{LMl-m}^{l_1m_1}C_{Lql-q}^{l_1 0} \tag{7}$$

are the coefficients of the addition theorems for the Helmholtz vector harmonics (see, e.g. [17]), where symbols *C* stand for the Clebsch–Gordan coefficients [19], $m_1=M-m$.

Notice that equation system (6) can be solved by the iteration method. For this system, $|M|\le L$, and the maximum of index *L* is usually the integer of $X_j+4X_j^{1/3}+2$ [2], where $X_j=k_0\tilde{a}_j$, and $\tilde{a}_j$ is the *j*th particle radius.

Expression (4) is the transverse spherical wave leaving the *j*th particle. The substitution of (4) into (2) yields the transverse spherical wave leaving the cluster. In this case, the cluster size is assumed small compared to the observation point distance. So, the observation point direction is the same for all particles of the cluster (Fig. 1). The amplitude of wave (4) varies directly with r^{-1}, where *r* is the cluster distance. Unlike (4),

field (3) is not a transverse spherical wave. This field contains a radial (along the vector $\mathbf{r}_j$) component and terms decaying like r^{-n_1} for $n_1 > 1$. The latter follows from the Hankel function $h_l(x)$ expansion in the finite series carrying x^{-n_1} degrees, $n_1 = 1, 2, 3, ..., l+1$ (see, e.g. [20]). In the literature, the terms proportional to r^{-n_1}, $n_1 > 1$, are identified with the near field [21]. The scattering of this complex field from each particle of the cluster is described by equation system (6). Coefficients (7) of this system determine the field outside the particles. The field behavior depends on the distances between them. Generally coefficients (7) contain terms decaying faster than r_{js}^{-1}. Keeping only terms proportional to r_{js}^{-1} offers these coefficients in the form [17]

$$H_{LMlm}^{(q)}(\hat{\mathbf{n}}_0, \hat{\mathbf{r}}_{js}) = \frac{2l+1}{2} \frac{\exp(ik_0 r_{js})}{-ik_0 r_{js}} \times$$

$$\times D_{Mq}^{L}(\hat{\mathbf{n}}_0, \hat{\mathbf{r}}_{sj}) D_{mq}^{*l}(\hat{\mathbf{n}}_0, \hat{\mathbf{r}}_{sj}). \quad (8)$$

Coefficients (8) govern the spherical wave traveling from the *s*th particle to the *j*th particle. Hence a disregard of the near field in (7) only keeps the terms referring to spherical waves propagating outside the scatterers, no matter what the scatterer spacing is. This means that the description of the field outside the scatterers ignores the scatterer size with respect to its separation. Formally coefficients (8) can come from (7) under the conditions $k_0 r_{js} \gg 1$, $2k_0 r_{js} \gg (k_0 \tilde{a}_s + k_0 \tilde{a}_j)^2$ and $r_{js} \gg \tilde{a}_j + \tilde{a}_s$ ($\tilde{a}_i$ is the *i*th scatterer radius), that is the scatterers are assumed to be far apart from one another. Later on, a comparison between the scattering models will be made upon coefficients (8) whatever the scatterer spacing. Notice that the second of the two conditions right above estimates the average spacing under which the screening can take effect. This estimation is true for particles whose size is of the wavelength order and more. For equal particles, in particular, this condition takes the appearance $k_0 r_{js} \gg 2(k_0 \tilde{a})^2$, where $\tilde{a}$ is the particle radius.

Although any element of the scattering matrix can be affected by the near field, the mutual screening takes most effect on the intensity (for the near field action on polarization, refer to Introduction). That is why our consideration of the near field effect the on scattered radiation characteristics will be only concerned with intensity. The characteristics of radiation scattered by a cluster are determined by the scattering matrix **F** describing how the Stokes vector-parameter $\mathbf{I}_0$ of the incident radiation is translated to the Stokes vector-parameter **I** of the scattered radiation [2, 15]

$$\mathbf{I} = \frac{1}{(k_0 r)^2} \mathbf{F} \mathbf{I}_0. \quad (9)$$

When the incident radiation is nonpolarized, related intensity *I* of the scattered radiation is defined by element F_{11} of scattering matrix (9) (see, e.g. [22])

$$I = F_{11} = \sum_{pn} |S_{pn}|^2. \quad (10)$$

In the CP representation, S_{pn} $(p, n = \pm 1)$ is the amplitude matrix of the radiation scattered by the cluster. Likewise scattered field (2), the cluster amplitude matrix S_{pn} can be summed from the amplitude matrices of all the particles. The *j*th particle amplitude matrix $t_{pn}^{(j)}(\mathbf{k}_0, \mathbf{k}_{sc})$ is available from (4) (see, e.g. [17, 18])

$$t_{pn}^{(j)}(\mathbf{k}_0, \mathbf{k}_{sc}) = \exp(-i\mathbf{k}_{sc}\mathbf{R}_j + in\psi_0 - ip\psi_{sc}) \times$$

$$\times \sum_{LM} \frac{2L+1}{2} A_{LM}^{(jpn)} D_{Mp}^{*L}(\hat{\mathbf{n}}_0, \hat{\mathbf{k}}_{sc}). \quad (11)$$

Matrix (11) is written in a basis of spiral unit vectors [19]. These unit vectors are produced by the spherical unit vectors $\mathbf{e}_{\theta_0}$, $\mathbf{e}_{\varphi_0}$ lying in the meridional plane passing the axis *z* and the vector $\mathbf{k}_0$, and by the spherical unit vectors $\mathbf{e}_{\theta_{sc}}$, $\mathbf{e}_{\varphi_{sc}}$ lying in the meridional plane passing the axis *z* and the vector $\mathbf{k}_{sc}$ (Fig. 1). In other words, the intensity vector components of the incident and the scattered waves given in different meridional planes are related by matrix (11). The passage to the scattering plane (carrying $\mathbf{k}_0$ and $\mathbf{k}_{sc}$ vectors), where matrix **F** is defined, is realized via the addition theorems for the Wigner functions [19].

3. MUTUAL SCREENING IN DENSE-PACKING SYSTEMS OF SCATTERERS

The screening idea is usually associated with a situation when the scatterer size is larger than the wavelength. Yet the screening can come when the scatterer

is much smaller than the wavelength. Characteristic features of the electromagnetic wave scattering from a couple of small (compared to the wavelength) closely-spaced scatterers polarized like a dipole in an external field will be considered in a qualitative sense. The scatterer spacing is assumed to be small with respect to the wavelength λ. For a couple of such scatterers, two possible charge configurations acquired in an external field $\mathbf{E}^{(0)}$ are shown in Fig. 2. The scatterers reside in the scattering plane coinciding with the figure plane, which is also the polarization plane of the incident radiation. The configuration in Fig. 2, a shows that the charges are not coupled by their near (electrostatic) fields. The intensity of the radiation scattered by the particles is not zero on the straight line *AB* connecting their centers. The charge configuration in Fig. 2, b is for electrostatically coupled scatterers: the intensity of the scattered radiation on straight line *AB* is zero. In other words, the near field involvement leads to the "screening" of one scatterer by the other along their common centerline.

Of course, the scatterer configuration in Fig. 2, b is idealized, with the electrostatic field contribution intentionally inflated. By formulas from Section 2, the angular dependence of the scattered radiation intensity was calculated for a couple of Rayleigh scatterers touching each other. The results plotted in Fig. 3 are for the particle wave parameter $X = k_0\tilde{a} = 0.01$, and the refractive index $\tilde{m} = 10.0 + i0$. That large refractive index was taken to show up differences between the two models. The scatterers reside in the *xz* plane, the symmetry axis of the couple of scatterers makes an angle of $45°$ with the *z* axis. A unit-intensity radiation is incident along the *z* axis. The scattering angle θ is measured clockwise from the *z* axis. The intensity of the scattered radiation is divided by $2X^2$. The dashed and the solid curves are from the models ignoring and considering the near field, respectively. The thick and the thin curves are given to distinguish between the cases of the incident radiation polarization in the scattering plane and in the plane normal to it, respectively.

As seen from the figure, the scattered radiation intensity from the near-field ignoring model behaves the same as for a single Rayleigh scatterer and fully obeys the scheme in Fig. 2, a. Namely, when the radiation is linearly polarized in the scattering plane, the scattered radiation intensity maxima occur in the scattering directions $\theta = 0°$ and $\theta = 180°$, the minimum is at

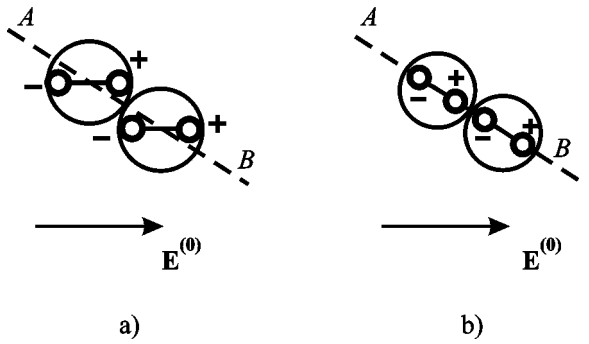

FIG. 2: Schematic showing the near-field "screening" of small-size dipole scatterers. Straight line AB connects the centers of the scatterers. When the induced charges do not interact, the intensity of the radiation scattered by the particles is not zero on line AB (a). When they do that and the near-field coupling takes place, the intensity of the radiation scattered by the particles is zero on AB line (b)

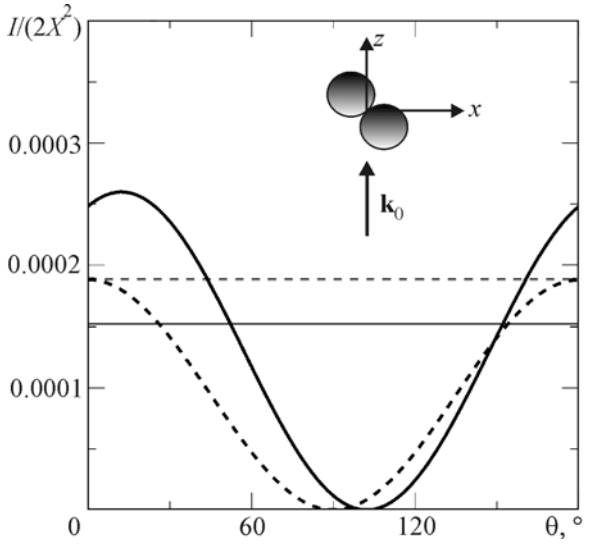

FIG. 3: Relative intensity *I* of the radiation scattered by a couple of closely-spaced Rayleigh scatterers versus the scattering angle θ. The wave parameter of the particles is $X = 0.01$ and the refractive index is $\tilde{m} = 10.0 + i0$. The dashed and the solid curves are for the models ignoring and considering the near field, respectively. The thick and the thin curves are for the incident radiation polarization in the plane of scattering and in the plane normal to it, respectively

$\theta = 90°$. For the radiation linearly polarized in the perpendicular plane, the scattering intensity does not depend on the scattering angle. In the $\theta = 0°$ and $\theta = 180°$ directions, the intensity does not depend on polarization of the incident radiation.

In the near-field considering model, the scattered radiation intensity in the $\theta = 0°$ and $\theta = 180°$ directions depends strongly on polarization of the incident radiation. In these directions, the scattered radiation intensity substantially exceeds the analogous amounts from the other model when the incident radiation is polarized in the scattering plane. The reason is that the electrostatic interaction between the scatterers (Fig. 2, b) considerably increases the dipole moments compared to the previous model. The intensity maximum is seen, however, at $\theta \approx 15°$, whereas the scheme from Fig. 2, b predicts it in the direction normal to *AB* line connecting the centers of the dipoles (in the considered example, this direction corresponds to $\theta = 45°$). This means that the dipole moments of the scatterers in Fig. 3 are aligned with the direction $\theta \approx 105°$, where the intensity is zero. The intensity behavior within $100° < \theta < 160°$ can be of interest. On this interval, the intensity from the near-field model is distinctly lower than that from the near-field ignoring model. This intensity decrease is explained by the scatterer "screening" interpreted in qualitative terms in Fig. 2.

Previously the near field part was played by the electrostatic field. Now turn to the screening arising during the electromagnetic interaction of scatterers. Consider the EMW scattering from a simplest cluster consisting of two similar spherical particles (bisphere). The bisphere particles touch each other, their radii being comparable with the wavelength. The scattering intensity of such a cluster versus the scattering angle is plotted in Figs. 4, a and b for two bisphere orientations with respect to the scattering plane. The intensity computations are due to the formulas from Section 2. The bisphere symmetry axis is normal to the direction of the incident nonpolarized radiation. The wave parameter of the bisphere particles is $X = k_0 \tilde{a} = 4.0$, the refractive index is $\tilde{m} = 1.32 + i0.05$. A choice of the refractive index with a relatively small real part and a fairly large imaginary part keeps intensity curves from abrupt bursts, which are typical for nonabsorbing scatterers with a large real part of the refractive index. For the refractive index employed, the scattered radiation intensity curves are relatively smooth, which simplifies the comparison between the two scattering models. The solid curves in Fig. 4 come from the calculations involving coefficients (7) (the allowance for the near field). The dashed curves correspond to the calculations with coefficients (8) (the near field ignored). The scattering plane coincides with the plane of the figure. The corresponding bisphere orientation with respect to the scattering plane is seen at the upper right of Figs. 4, a and b. For all the curves, the scattering radiation intensity (component F_{11} in (10)) was divided by $2X$.

A comparison of the curves in Fig. 4, a and b reveals that the near field involvement substantially (nearly an order of magnitude) reduces the scattering intensity in the direction of the bisphere symmetry axis ($\theta = 90°$). This fall in intensity is explained by the mutual screening of the particles in the near field. As mentioned in Section 2, coefficients (7) include all peculiarities of the field between the particles. These peculiarities are realized, in particular, in the mutual screening of particles. A disregard of the field components decaying faster than r_{js}^{-1} in coefficients (7) leads to spherical wave approximation (8). This means that the description of the field between the particles neglects the particle size with respect to the particle spacing. In this approximation, the mutual screening of particles is ruled out. That is why the scattering along the bisphere axis is much more intensive.

In Fig. 4, c, the radiation scattering intensity along the bisphere axis is plotted versus the spacing between the bisphere components. As is seen, the screening action can be traced until the spacing gets several diameters of the scatterers. The intensity minima are located by the interference of waves leaving the scatterers and arriving at the observation point with the phase difference $n_1\pi$, where n_1 is an odd integer. In the near-field model, the scattered radiation intensity versus the scatterer size demonstrates analogous minima along the bisphere axis when the bisphere components touch each other (Fig. 4, d, solid line). However the intensity curves from the near-field model in Figs. 4, c and d are actually dependences on the distance between the centers of the scatterers, the interference character in Fig. 4, d is not so bright. Besides, the amplitude of the interference oscillations decays as the scatterer size grows, which is caused by a larger destructive action of the scatterer size on the wave interference because the screening enhances.

For reference, Fig. 4, d presents the single-scatterer dependence (points). It is seen that for the given refractive index, the screening tends, as the scatterer size grows, to the geometrical optical limit, where the scattered radiation intensity is halved. A substantial (near-

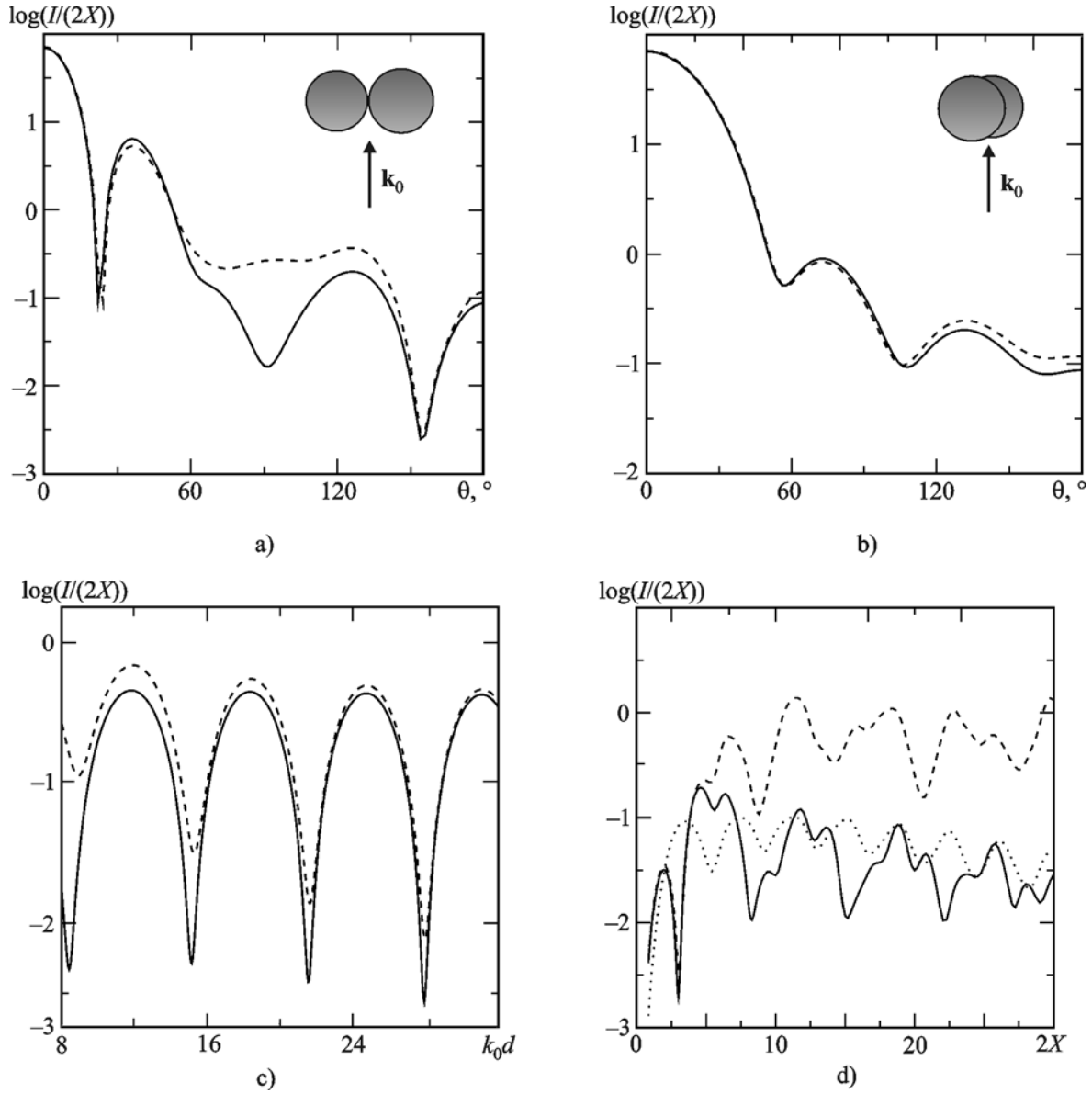

FIG. 4: The relative intensity of the bisphere scattered radiation versus the scattering angle: the bisphere components reside in the scattering plane (figure plane) (a) and in the plane normal to the scattering plane (b). The relative intensity of the scattered radiation in the bisphere axis direction versus the scatterer separation k_{od} (c) and the scatterer size (d). The intensity shown with points refers to a single scatterer. The solid and dashed lines correspond to the models with and without the near field, respectively. The wave parameter of the bisphere particles is $X = 4.0$, the refractive index is $\tilde{m} = 1.32 + i0.05$. The bisphere axis is normal to the wave vector $\mathbf{k}_0$ of the incident radiation

ly an order of magnitude) difference between the intensities from the two models is caused by a large contribution from the multiple scattering when the near field is considered. In particular, a significant contribution from the multiple scattering, which decreases as the bisphere component spacing increases, is clearly seen in Fig. 4, c at the intensity minima near $k_0 d \approx 9$ and $k_0 d \approx 15$.

It should be mentioned that the concept of "multiple scattering" is different for the two models discussed. To interpret its sense in the case of the near-field ignoring model, introduce the notation

$$f_{pn}^{(j)}(\hat{\mathbf{k}}_{sc},\hat{\mathbf{n}}_0)=\sum_{LM}\frac{2L+1}{2}A_{LM}^{(jpn)}D_{Mp}^{*L}(\hat{\mathbf{n}}_0,\hat{\mathbf{k}}_{sc}). \qquad (12)$$

Then formula (4) becomes

$$\mathbf{E}^{(j)}=\frac{\exp(ik_0r)}{-ik_0r}\exp(-i\mathbf{k}_{sc}\mathbf{R}_j)\times$$

$$\times\sum_p f_{pn}^{(j)}(\hat{\mathbf{k}}_{sc},\hat{\mathbf{n}}_0)\mathbf{e}_p(\hat{\mathbf{k}}_{sc}). \qquad (13)$$

Field (13) is a superposition of waves with right-handed ($p=1$) and left-handed ($p=-1$) circular polarizations and $f_{pn}^{(j)}(\hat{\mathbf{k}}_{sc},\hat{\mathbf{n}}_0)$ amplitudes. To get the equation for these amplitudes, substitute (8) in (6) and make use of the addition theorems for the Wigner functions [19]. Eventually we arrive at the following system of equations for coefficients (12)

$$f_{pn}^{(j)}(\hat{\mathbf{k}}_{sc},\hat{\mathbf{n}}_0)=g_{pn}^{(j)}(\hat{\mathbf{k}}_{sc},\hat{\mathbf{k}}_0)\exp(i\mathbf{k}_0\mathbf{R}_j)+$$

$$+\sum_q g_{pq}^{(j)}(\hat{\mathbf{k}}_{sc},\hat{\mathbf{r}}_{sj})\sum_{s\neq j}^{N}\frac{\exp(ik_0r_{js})}{-ik_0r_{js}}f_{qn}^{(s)}(\hat{\mathbf{r}}_{sj},\hat{\mathbf{n}}_0), \qquad (14)$$

where

$$g_{pn}^{(j)}(\hat{\mathbf{k}}_{sc},\hat{\mathbf{k}}_0)=\sum_L\frac{2L+1}{2}a_L^{(jpn)}D_{np}^{*L}(\hat{\mathbf{k}}_0,\hat{\mathbf{k}}_{sc}). \qquad (15)$$

Here $g_{pn}^{(j)}(\hat{\mathbf{k}}_{sc},\hat{\mathbf{k}}_0)$ is the amplitude of a circularly polarized wave with polarization *p*. The wave is scattered by the *j*th particle along the axis z_j of the coordinate system $\hat{\mathbf{k}}_{sc}$ (Fig. 1). In this case, incident plane wave (1) has circular polarization *n* and propagates along the axis z_0 of the coordinate system $\hat{\mathbf{k}}_0$.

The physical sense of equation system (14) is as follows. The amplitude $f_{pn}^{(j)}(\hat{\mathbf{k}}_{sc},\hat{\mathbf{n}}_0)$ of the wave scattered by the *j*th particle is a superposition of wave amplitudes, one of which is provided by the scattering of incident wave (1) (the first term in the right-hand side of (14)). The rest amplitudes are caused by the scattering of the waves arriving from the other scatterers of the cluster (the second term in the right-hand side of (14)). As the scatterer spacing is assumed to be far larger than the scatterer size, the wave arriving from the *s*th scatterer and acting on the *j*th scatterer is thought of as a quasi-plane uniform wave with an amplitude proportional to r_{js}^{-1}.

Let us represent an iteration procedure solution to equation system (14). This solution representation can be interpreted as a series expansion of amplitude (14) in scattering orders. In this case, the first term on the right-hand side of (14) corresponds to the single scattering from the *j*th particle. Its substitution into the second term corresponds to the double scattering from, first, the *s*th scatterer and then from the *j*th scatterer, and so on. In this way, expression (14) describes the process of multiple scattering of quasi-plane waves in the system of scatterers.

Unlike the previous model ignoring the near field, equation system (6) with coefficients (7) cannot be reduced to the form of (14). However it still allows the iteration procedure, which can be still interpreted as a series expansion of coefficients (5) in scattering orders. In these terms, the sense of the multiple scattering differs from its sense in the previous model. The near-field ignoring model deals with the scattering of quasi-plane waves acting on the scatterers. The near-field considering model interprets the "multiple scattering" as a process of the amplitude and phase redistribution between the coefficients $A_{LM}^{(jpn)}$ at different *j*, *L*, *M*, *n*, and *p*. In this case, such a relationship between the amplitudes and phases of these coefficients is established that leads to the scatterer screening.

Now let us trace the near-field mutual interaction of scatterers in clusters with chaotic orientation of spherical particles. Some computer codes from the Internet [23] were adopted for calculating the scattered radiation characteristics of the clusters of the kind with the near field included. These very codes were adapted for calculating the scattering characteristics with the near field ignored. Clusters of identical particles were generated by the methodology from [24]. The cases of clusters employed in the calculations and consisting of similar 50, 100 and 200 particles are seen in Fig. 5. The shape of the clusters is nearly spherical, the particle arrangement is random.

The wave parameter of cluster particles is $X=1.5$, the refractive indices are $\tilde{m}=1.55+i0.001$ and $\tilde{m}=1.55+i0.1$. The cluster packing density is

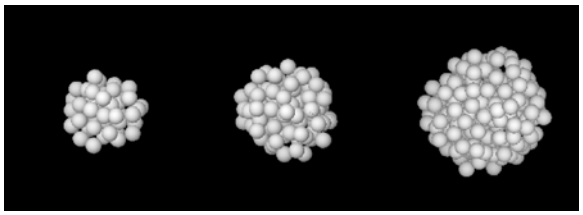

FIG. 5: Clusters consisting of 50, 100 and 200 identical spherical particles. The average wave parameter X_0 of these clusters is about 9.25, 11.9 and 14.67, respectively

$\xi = N\left(X/X_0\right)^3 \approx 0.2$, where N is the number of particles in the cluster. The cluster wave parameter is $X_0 = k_0 a_{\rm m}$ ($a_{\rm m}$ is the radius of the minimum sphere circumscribed around the cluster). The intensity of the radiation scattered by these chaotic-orientation clusters is plotted versus the scattering angle in Fig.6. The thick curves were obtained with allowance for the near field (with coefficients (7)). The thin curves are for the near field ignored (with coefficients (8)). The intensity was always divided by X_0^2.

As seen from Fig. 6, a disregard of the near field considerably increases the scattered radiation intensity at all scattering angles. A point of interest is the intensity behavior at $\theta > 60°$. With the near field included, the intensity in this angular range depends weakly on the number N of particles (especially for heavily absorbing scatterers). In so far as the intensity is normalized to the cross-sectional square unit (to be specific, it is divided by X_0^2), this dependence means that at least in this angular range the intensity is mostly determined by the upper layer of cluster particles. The rest particles of the cluster are screened by the upper layer of particles. When the near field is ignored, the particles do not screen one another. Thus, the multiple scattering process involves more particles, enhancing the multiple scattering contribution and the scattered radiation intensity compared to the model with the near field included. For the same reason, the intensity dependence on the number of particles in the cluster is heavier from the model ignoring the near field, and it is the more so for weakly absorbing scatterers.

In the scattering direction $\theta \approx 0$, the main contributor to the scattered radiation intensity is the interference of single-scattered waves. When the near field is taken into account, then, in view of the particle screening and wave phase shifts inside the cluster, the main contribution to this interference is from the particles nearby the

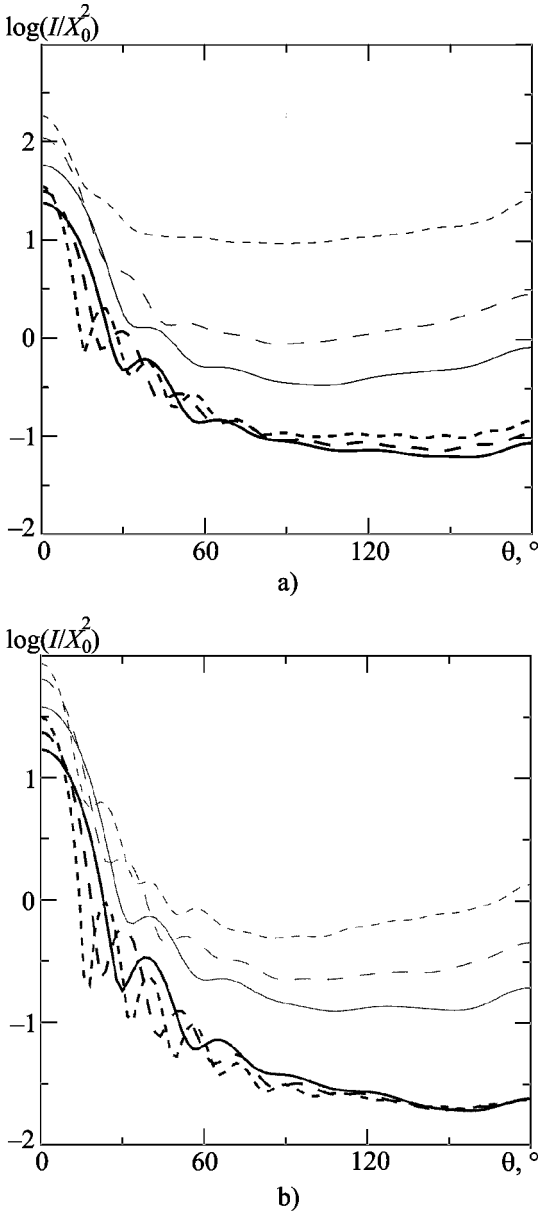

FIG. 6: The relative intensity of the radiation scattered by chaotic-orientation clusters of spherical particles with and without the near field considered (thick and thin lines, respectively) versus the scattering angle θ. —— $N = 50$, – – – $N = 100$, - - - $N = 200$. The wave parameter of the cluster particles is $X = 1.5$, the refractive index is $\tilde{m} = 1.55 + i0.001$ (a) and $\tilde{m} = 1.55 + i0.01$ (b)

cluster equator (limb) [11]. The number N of these particles is approximately proportional to the cluster average radius. As the interference contributes in proportion to the number $\tilde{N}(\tilde{N}-1)$, the scattered radiation intensity in the $\theta \approx 0$ direction varies directly with the cluster cross-sectional area. Therefore with the normalization as mentioned, the intensity in this scattering direction does not depend too much on the number of particles in a cluster. When the near field is ignored, each particle of a cluster contributes to the interference. The scattered radiation intensity is larger and depends more on the number of particles in a cluster.

It would be of interest to trace the behavior of the scattered radiation intensity in the area of the opposition scattering angles (near $\theta = 180°$). This angular interval is a valid one for interpreting observations of atmosphere-free celestial bodies offering, as a rule, the so-called brightness opposition effect in the visible region of spectrum (see, e.g. [23]). For reference, the brightness opposition effect consists in the nonlinear increase of the object brightness as the phase angle $\alpha = \pi - \theta$ decreases. Fig. 7 reports the scattered radiation intensity versus the phase angle for $N = 50$ and $N = 200$ clusters (solid and dashed lines, respectively). As before, thick and thin lines correspond to the calculations with the near field considered and ignored, respectively. According to the picture, the opposition effect is more pronounced in the model with the near field ignored. And this is the more so for heavily absorbing scatterers (Fig. 7, b). Thus, in the near-field ignoring model, the $N = 200$ cluster demonstrates an obvious opposition effect. In the near-field model, the opposition effect from the same cluster is insignificant (the dashed curves in Fig. 7, b). According to [8-12], this difference in the intensity behavior between the two models is caused by the near field nonuniformity (see Introduction). It is notable that the brightness opposition effect is slight for dark *F*-type asteroids, while for light asteroids it is seen clearly [25]. This can be explained by a high packing density of scatterers of a small-size and a large imaginary part of the refractive index.

Attention is drawn to the oscillating character of the intensity curves of the $N = 200$ cluster in the near-field model (Fig. 7). Also, a similar but more pronounced oscillating character of the intensity is demonstrated by chaotic-orientation clusters of the same particles with a regular packing of the particles at tetrahedron vertices [11]. This suggests that the oscillations on the curves in Fig. 7 can be caused by the cluster upper layer getting structurally bounded at this packing density. The periodicity of oscillations confirms it. In the near-field ignoring model, the contribution from the multiple scattering is large enough to "wash" these oscillations "out".

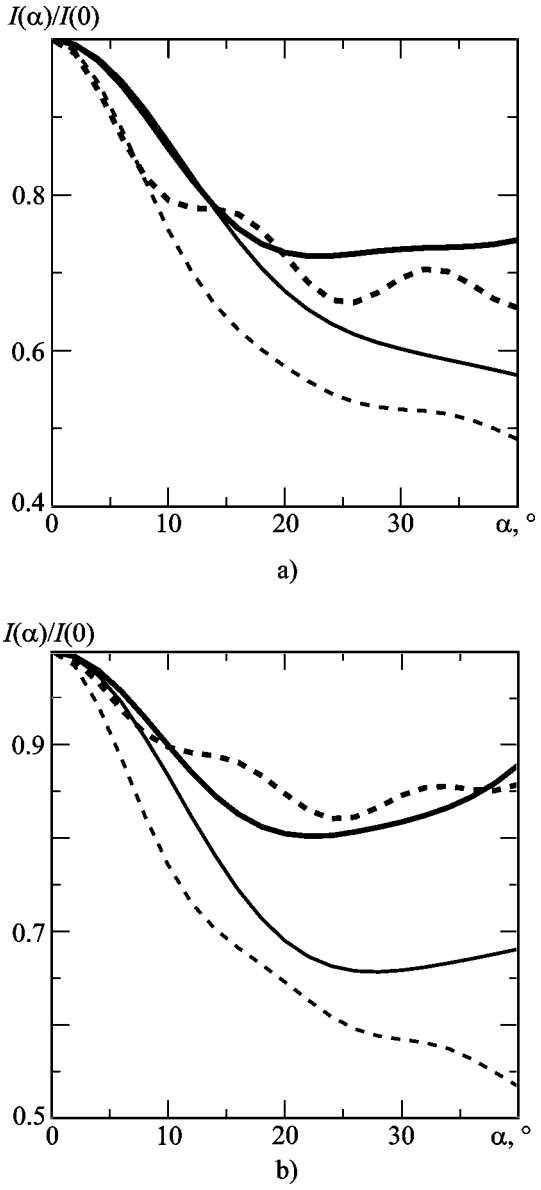

FIG. 7: Relative intensity of the radiation scattered by chaotic-orientation clusters of spherical particles with and without the near field considered (thick and thin lines, respectively) near the opposition scattering angles. The refractive index is $\tilde{m} = 1.55 + i0.001$ (a) and $\tilde{m} = 1.55 + i0.01$ (b). The solid curves are for $N = 50$, the dashed curves are for $N = 200$

4. CONCLUSIONS

In this paper, the near-field scattering features of collections (clusters) of spherical scatterers are considered. It has been shown that the near-field mutual screening of scatterers substantially reduces the cluster scattering intensity compared to the scattering model ignoring the near field. This model stands behind the modern theory of multiple scattering by discrete media. The numerical results on the intensity of the radiation scattered by systems of scatterers indicate that consideration must be given to the near field when the theory of multiple scattering by dense packing media is constructed and when various measurements are interpreted.

ACKNOWLEDGEMENTS

The author expresses his gratitude to A. S. Bryukhovetski, A. A. Minakov, and S. L. Prosvirnin for their constructive comments made during the discussion of the present paper manuscript.

REFERENCES

1. Mishchenko, M. I., Vector radiative transfer equation for arbitrarily shaped and arbitrarily oriented particles: a microphysical derivation from statistical electromagnetics, *Appl. Opt*., 41:7114-7134, 2002.
2. Mishchenko, M. I., Travis, L. D., and Lacis, A. A. Multiple Scattering of Light by Particles. Radiative Transfer and Coherent Backscattering. Cambridge: Cambridge University Press; 2006.
3. Ivanov, A. P., Loyko, V. A., and Dik, V. P. Propagation of Light in Dense-Packing Discrete Media. Minsk: Nauka i Tekhnika; 1988 (in Russian).
4. Thang, L. and Kong, J. A., Scattering of electromagnetic waves from a dense medium consisting of correlated Mie scatterers with size distributions and applications to dry snow, *J. Electromagn. Waves Appl*., 6:265-286, 1992.
5. Tsang, L., Chen, C. -T., Chang, A. T. C., Guo, J., and Ding, K. -H., Dense media radiative transfer theory on quasi-crystalline approximation with applications to passive microwave remote sensing of snow, *Radio Sci*., 35:731-749, 2000.
6. Zhang, H. and Voss, K. J., Comparisons of bidirectional reflectance distribution function measurements on prepared particulate surfaces and radiative transfer models, *Appl. Opt*., 44:597-610, 2005.
7. Ishimaru, A. Wave Propagation and Scattering in Random Media. Vol. 1. New York: Academic; 1978.
8. Tishkovets, V. P., Backward scattering of light by dense-packing media, *Opt. i Spektr.*, 85:233-238, 1998 (in Russian).
9. Tishkovets, V. P., and Litvinov, P. V., Opposition effects in scattering of light by regolith-type media, *Astron. Vestn*., 33(2):186-192, 1999 (in Russian).
10. Tishkovets, V. P., Litvinov, P. V., Petrova, E. V., Jockers, K., and Mishchenko, M. I. Backscattering effects for discrete random media: Theoretical results. In: Videen, G. , Yatskiv, Y., Mishchenko, M., editors. Photopolarimetry in Remote Sensing. Dordrecht, Netherlands: Kluwer Academic Publishers; 2004. p. 221-242.
11. Tishkovets, V. P., Petrova, E. V., and Jockers, K., Optical properties of aggregate particles comparable in size to the wavelength, *J. Quant. Spectrosc. Radiat. Transfer*., 86(3):241-265, 2004.
12. Petrova, E. V., Tishkovets, V. P., and Jockers, K., Modeling of opposition effects with ensembles of clusters: Interplay of various scattering mechanisms, *Icarus*., 188:233-245, 2007.
13. Mishchenko, M. I., Hovenier, J. W., and Mackowski, D. W., Single scattering by a small volume element, J*OSA A*, 21:71-87, 2004.
14. Mishchenko, M. I., Liu, L., Mackowski, D. W., Cairns, B., and Videen, G., Multiple scattering by random particulate media: exact 3D results, *Optics Express*, 15:2822-2836, 2007.
15. Mishchenko, M. I., Travis, L. D., and Lacis, A. A. Scattering, Absorption, and Emission of Light by Small Particles. Cambridge: Cambridge University Press; 2002.
16. Borghese, F., Denti, P., and Saija, R. Scattering from model nonspherical particles. Theory and applications to environmental physics. Berlin: Springer; 2002.
17. Tishkovets, V. P. and Mishchenko, M. I., Coherent backscattering of light by a layer of discrete random medium, *J. Quant. Spectrosc. Radiat. Transfer*, 86:161-180, 2004.
18. Tishkovets, V. P., Incoherent and coherent backscattering of light by a layer of densely packed random medium, *J. Quant. Spectrosc. Radiat. Transfer*, 108:454-463, 2007.
19. Varshalovich, D. A., Moskalev, A. N., and Khersonskiy, V. K. Quantum Theory of Angular Momentum. Moscow: Nauka; 1975 (in Russian).
20. Gradshteyn, I. S. and Ryzhik, I. M., Table of Integrals, Series, and Products. Academic: New York; 1994.
21. Greffet, J. -J. and Carminati, R., Image formation in near-field optics, *Progr. Surf. Sci*., 56:133-237, 1998.
22. Tishkovets, V. P. and Jockers, K., Multiple scattering of light by densely packed random media of spherical particles: Dense media vector radiative transfer equation, *J. Quant. Spectrosc. Radiat. Transfer*, 101:54-72, 2006.
23. Mackowski, D. W., Fuller, K., and Mishchenko, M. I. Codes for calculation of scattering by clusters of spheres. Available from: ftp://ftp.eng.auburn.edu/pub/dmckwski/scatcodes/index.html
24. Mackowski, D. W., Electrostatics analysis of sphere clusters in the Rayleigh limit: application to soot particles, *Appl. Opt*., 34:3535-3545, 1995.
25. Belskaya, I. N. Optical properties of asteroid, centaur and Koyper belt surfaces. Thesis for doctor degree in physics and mathematics. Author's abstract. Kyiv: 2007 (in Russian).